工學博士學位論文

Fabrication of Graphene and Molybdenum Disulfide Electrodes and Their Biosensor Applications

그래핀과 이황화몰리브덴 전극의 제조 및 바이오센서로의 응용

2017年 8月

서울大學校 大學院

化學生物工學部

安 智 賢

Fabrication of Graphene and Molybdenum Disulfide Electrodes and Their Biosensor Applications

by

Ji Hyun An

Submitted to the Graduate School of Seoul National University in Partial Fulfillment of the Requirements for the Degree of Doctor of Philosophy

August, 2017

Thesis Adviser: Jyongsik Jang

Abstract

Biosensors have received substantial attentions in analytical chemistry owing to their potential for a wide range of applications. Compared to various sensing methods, electrochemical sensing method is a very attractive and powerful tool for high-performance biosensors. Electrochemical biosensors recognize a measurable electrical signal through a transducer, leading to high sensitivity, low power consumption, simple instrumentation, and short analysis time. Among electrochemical biosensors, field-effect transistor (FET)-based sensors are promising candidates because of their ability to rapidly and sensitively detect analytes *via* efficient interfacial transfer of charge carriers. Transducers play a crucial role in improving the performance of FET sensors. From a material viewpoint, the characteristics of transducer materials significantly affect the sensing performance. Therefore, it is important to develop and utilize enhanced transducer materials for FET-type biosensors.

This dissertation describes CVD graphene and MoS_2 as transducers for biosensor applications. Graphene, two-dimensinal (2D) structures with hexagonal lattice, comprises single- or few- layer of sp^2-hybridized carbon atoms. Graphene has grabbed considerable focus owing to its

outstanding thermal, mechanical, and electrical properties. Transition metal dichalcogenides (TMDs) are graphene-like 2D layered materials. Molybdenum disulfide (MoS_2), which is a layered TMD, features high carrier mobility and low noise level. From these attractive properties, three different nanostructures based on graphene and MoS_2 were used as transducers for biosensors. First, graphene was prepared *via* chemical vapor deposition (CVD) process. CVD graphene was applied to HBsAg and taste sensors. Second, the flower-like MoS_2 nanospheres were fabricated using a simple hydrothermal method. After vapor deposition polymerization (VDP), carboxylated polypyrrole-coated nanospheres showed improved performance in As(III) sensor. Lastly, MoS_2 nanosheets were grown on graphene surface by hydrothermal process. The nanocomposite was applied to a highly sensitive nonenzymatic sensor for H_2O_2 detection. These transducer materials can provide enhanced sensing performance with high sensitivity, good selectivity, and rapid response for various sensor applications.

Keywords: Graphene, Molybdenum disulfide, Field-effect-transistor, Biosensor

Student Number: 2014-31079

List of Abbreviations

2D: two dimension

AA: ascorbic acid

APS: 3-aminopropyltrimethoxysilane

Apt-CFMNS: aptamer-conjugated CFMNS

Apt-FMNS: aptamer-conjugated FMNS

Ar: argon

As(III): arsenite

As(V): arsenate

As: arsenic

Au: gold

BSA: bovine serum albumin

ca.: circa

CFMNS: CPPy-coated flower-like MoS_2 nanosphere

CG: CVD graphene

CH_4: methane

cm: centi-meter

CNT: carbon nanotube

-COOH: carboxyl group

CP: conducting polymer

CPPy: carboxylated polypyrrole

Cr: chrome

Cu: copper

CVD: chemical vapor deposition

CYC: cyclamate

D: drain

DAN: 1,5-diaminonaphthalene

DGE: duplexed graphene electrode

D-Glu: Dglucuronic acid

DMT-MM: 4-(4,6-dimethoxy-1,3,5-triazin-2-yl)-4-ethylmorpholinium chloride

DNA: deoxyribonucleic acid

DPBS: Dulbecco's phosphate buffered saline

eV: electron volt

$FeCl_3$: iron (III) chloride

FE-SEM: field emission-scanning electron microscopy

FET: field-effect-transistor

fM: femto-mole

FMNS: flower-like MoS_2 nanosphere

FT-IR: fourier transform-infrared

G: gate

GA: glutaraldehyde

GM: graphene micropattern

GMP: guanosine monophosphate

GPCR: G protein-coupled receptor

H_2: hydrogen

H_2O_2: hydrogen peroxide

HAS: hepatitis B aptasensor

HBsAg: hepatitis B surface antigen

HBV: hepatitis B virus

hr: hour

HR-TEM: high resolution-transmission electron microscopy

I: instantaneous recorded current

I_0: initial current

IDA: interdigitated array

IgG: immunoglobulin G

IMP: inosine monophosphate

I_{sd}: source to drain current

I-V: current-voltage

LOD: limit of detection

M: mole

MDL: minimum detectable level

MGE: multiplexed graphene electrode

min: minute

mM: milli-mole

MNS: MoS_2 nanosheet

MNSCG: MoS_2 nanosheets on CVD graphene

MoS_2: molybdenum disulfide

MSG: monosodium glutamate

mV: milli-volt

N_2: nitrogen

-NH_2: amino group

nm: nano-meter

nM: nano-mole

NS: nanosphere

-OH: hydroxyl group

PBS: phosphate-buffered saline

PEN: polyethylene naphthalate

pH: potential of hydrogen

pM: pico-mole

PMMA: poly(methyl methacrylate)

PPy: polypyrrole

PSE: 1-pyrenebutanoic acid *N*-hydroxysuccinimidyl ester

p-type: positive-type

RIE: reactive ion etching

RNA: ribonucleic acid

ROS: reactive oxygen species

S/N: signal to noise

s: second

S: source or sensitivity

SAED: selected area electron diffraction

sccm: standard cubic centimeters per minute

swCNT: single walled carbon nanotube

TEB: thermo-electrostatic bonding

TEM: transmission electron microscopy

TMD: transition metal dichalcogenide

Tr: transmittance

UA: uric acid

UV: ultraviolet

V: voltage

VDP: vapor deposition polymerization

V_g: gate voltage

V_{sd}: source to drain voltage

W/L: width to length

W: watt

XPS: x-ray photoemission spectroscopy

XRD: x-ray diffraction

List of Figures

Figure 1. Schematic of biosensor operation (left) and regeneration (right).

Figure 2. A schematic of a biosensor with electrochemical transducer.

Figure 3. Schematic illustration of the liquid-ion gated FET-type biosensor.

Figure 4. There are several methods of mass-production of graphene, which allow a wide choice in terms of size, quality and price for any particular application.

Figure 5. Wet−transfer method of the graphene on the flexible substrate.

Figure 6. (a) The atomic structure of layered MoS_2. Different sheets of MoS_2 are composed of three atomic layers S−Mo−S, where Mo and S are covalently bonded. (b) A top view of the honeycomb lattice.

Figure 7. Electronic energy diagrams and structures for (a) neutral PPy, (b) polaron, (c) bipolaron, and (d) fully doped PPy.

Figure 8. Synthetic procedure of flexible hepatitis B aptasensor on PEN film.

Figure 9. Chemical reactions among 1,5-diaminonaphthalene (DAN),

glutaraldehyde (GA) and hepatitis B surface antigen binding aptamer.

Figure 10. Raman spectrum of single layer graphene on a SiO_2 wafer substrate.

Figure 11. (a) UV–visible spectrum and photograph (inset) of single layer graphene transferred on PEN film (transmittance at 550 nm). (b) Flexible graphene platform with the gold electrodes.

Figure 12. FE-SEM images of (a) pristine graphene, (b) HAS_L, and (c) HAS-H electrodes, respectively (HAS indicates hepatitis B aptasensor).

Figure 13. Spectrophotometric absorbance of conjugated aptamers on HAS_H and HAS_L surfaces before and after washing process.

Figure 14. Current–voltage (I–V) curves of the hepatitis B aptasensor before and after the introductions of DAN, GA, and aptamers.

Figure 15. (a) Schematic illustration of a liquid-ion gated FET system ("G", "S", and "D" mean gating voltage and source/drain electrodes, respectively). (b) I_{sd}–V_{sd} output relationships of the graphene aptasensor at different V_g from 0 to –0.9 V in a step of –0.1 V (V_{sd}: 0 to –0.27 V in a step of –10 mV).

Figure 16. Real-time responses of the FET-type aptasensor with normalized current change ($\Delta I/I_0 = (I - I_0)/I_0$, where I is the real-time current and I_0 is the initial current).

Figure 17. Schematic illustration of HBsAg detection mechanism based on the FET-type sensor.

Figure 18. (a) Structures of diverse biomolecules as non-target analytes. (b) Selective response of the aptasensor toward target HBsAg (10 fM) and non-target analytes (1 nM).

Figure 19. Real-time measurements of the aptasensors toward (a) artificial saliva and (b) real saliva samples.

Figure 20. Sensitive changes toward various HBsAg concentrations (10 fM to 1 nM) (PBS (red line); real saliva (blue line)).

Figure 21. Schematic illustrations for the fabrication procedure of duplex sensor containing umami and sweet taste receptor nanovesicles.

Figure 22. Illustrative diagram of the sequential steps for the preparation of nanovesicles expressing heterodimeric human taste receptors. Umami taste receptor (T1R1/T1R3) and sweet taste receptor (T1R2/T1R3) were stably expressed.

Figure 23. Western blot analysis for T1R1, T1R2, and T1R3 on the taste

nanovesicles.

Figure 24. Photographic image of a fabricated multiplexed electrode on a silicon oxide wafer. Two pairs of the contact electrodes were simultaneously used to detect multiple responses.

Figure 25. (a) Raman spectrum of CVD graphene on a silicon oxide substrate. (b) HR-TEM observation of CVD-grown single layer graphene.

Figure 26. FT-IR spectra of graphene electrodes before (black line) and after (red line) the introduction of PSE.

Figure 27. (a) Low- and (b) high-resolution FE-SEM images of graphene channels after the introduction of nanovesicles.

Figure 28. (a) Current−voltage ($I-V$) curves of the DBT sensor before and after the immobilization of nanovesicles. (b) Output characteristics of a FET-type DBT (V_g, 0 to −2.5 V in a step of −0.5 V, and V_{sd}, 0 to −0.7 V in a step of −50 mV).

Figure 29. Schematic diagram depicting the FET geometry and showing the sensing mechanism of a DBT.

Figure 30. Discrimination of umami tastants with umami taste nanovesicle-immobilized bioelectronic tongues. Real-time response of a single channel in a DBT with various

concentrations of MSG (100 nM to 1 mM). DGE stands for duplex graphene electrode.

Figure 31. (a) Chemical structures for sensing tests related to umami taste. (b) Selective response of a DBT toward target tastant (MSG, 100 nM).

Figure 32. Dose-dependent responses of DBTs to artificial seasonings containing target umami tastant.

Figure 33. Sensing performance of sweet taste receptor nanovesicle-based bioelectronics tongues. (a) Real-time electrical measurement of a DBT to various sucrose concentrations (1 μM to 10 mM). (b) Calibration curves of DBTs toward tasteless, natural, and artificial sweet tastants.

Figure 34. (a) Chemical structures of diverse sweet tastants. (b) Selective property of a DBT toward target tastant (sucrose, 1 μM) and nontarget tastants (cellobiose and D-glucuronic acid, 1 mM).

Figure 35. Simultaneous detection of umami and sweet tastants using DBTs. (a) Schematic diagram of DBT geometry. (b) Real-time responses of two channels in the DBT sensor toward umami and sweet tastants.

Figure 36. Real-time responses from (a) tomato juice solution and (b) green tea solution as real drink samples (red and blue lines indicate umami and sweet channels, respectively).

Figure 37. Schematic diagram of the fabrication steps for flower-like MoS_2 nanospheres coated with carboxylated polypyrrole.

Figure 38. XRD patterns of FMNSs (a) before annealing, (b) after annealing at 400 °C, and (c) after annealing at 600 °C.

Figure 39. TEM images of FMNS with various hydrazine monohydrate quantity; (a) 0.75 mL, (b) 1.875 mL, and (c) 3.75 mL, respectively.

Figure 40. Nitrogen adsorption−desorption isotherms of FMNS_0.75 (black line), FMNS_1.875 (red line), and FMNS_3.75 (blue line), respectively.

Figure 41. (a) FE-SEM micrograph of FMNSs. (b) TEM image of FMNS.

Figure 42. HR-TEM image and SAED diffraction pattern (inset) of FMNS.

Figure 43. XRD patterns of (a) flower-like MoS_2 nanospheres and (b) bulk-MoS_2.

Figure 44. High-resolution XPS spectra of (a) the Mo 3d region and (b)

the S 2p region of FMNSs.

Figure 45. HR-TEM image of carboxylated polypyrrole-coated FMNS.

Figure 46. FT-IR spectra of FMNSs (black line) and CFMNSs (red line).

Figure 47. (a) XPS spectra of FMNSs (black line) and CFMNSs (red line). (b) Deconvoluated XPS N 1 s spectrum of CFMNSs.

Figure 48. Schematic illustrations for the immobilization procedure of aptamer-conjugated CFMNSs (Apt-CFMNSs) on the electrode. SEM image (inset) of Apt-CFMNSs.

Figure 49. The absorbance of immobilized aptamer on FMNS and CFMNS surfaces before and after washing.

Figure 46. FT-IR spectra of FMNSs (black line) and CFMNSs (red line).

Figure 47. (a) XPS spectra of FMNSs (black line) and CFMNSs (red line). (b) Deconvoluated XPS N 1 s spectrum of CFMNSs.

Figure 48. Schematic illustrations for the immobilization procedure of aptamer-conjugated CFMNSs (Apt-CFMNSs) on the electrode. SEM image (inset) of Apt-CFMNSs.

Figure 49. The absorbance of immobilized aptamer on FMNS and CFMNS surfaces before and after washing.

Figure 50. (a) Current–voltage (*I*–*V*) curve of FMNSs-based electrode. (b) Current–voltage (*I*–*V*) relations of MoS_2-based sensor

before and after the introduction of aptamer.

Figure 51. (a) Illustrative diagram of liquid-ion gated FET sensor using Apt-CFMNSs as transducers. (b) Output characteristics of Apt-CFMNSs FET-type sensor under different gate voltage (V_g, 0.2 to –0.8 V in a step of –0.1 V, and V_{sd}, 0 to –0.14 V in a step of –10 mV).

Figure 52. Discrimination of target As(III) with different sensors using CFMNS (black line), Apt-FMNS (gray line), and Apt-CFMNS (blue line). (a) Real-time responses and (b) calibration curves toward various As(III) concentrations (1 pM to 10 nM).

Figure 53. (a-c) Selective responses of Apt-CFMNSs FET sensor toward target analyte (As(III), 1pM) and nontarget metal ions (Fe^{2+}, Zn^{2+}, Mg^{2+}, Cu^{2+}, Mn^{2+}, Li^{+}, Cd^{2+}, Co^{2+}, and Ni^{2+}, 1 μM).

Figure 54. (a) Selective response of Apt-CFMNSs FET sensor toward 1 pM, and 10 pM concentrations of As(III) in mixture containing 1 μM of the nontarget metal ions. (b) Real-time response from river water as real water sample.

Figure 55. Schematic illustrations for the preparation steps of MNSCG.

Figure 56. FE-SEM images of MNSCG (a) untreated with DAN and (b)

treated with DAN.

Figure 57. FE-SEM images of (a) MNSCG_L and (b) MNSCG_H.

Figure 58. FE-SEM images of MNSCGs with (a) the optimum and (b) the excess amount of precursors. SEM images of MNSCGs reacted for (c) 6 hr and (d) 18 hr, respectively.

Figure 59. FT-IR spectra of CVD graphene unmodified (black line) and modified (red line) with DAN.

Figure 60. Fully scanned XPS spectra of Pristine CG (black line) and MNSCG (red line).

Figure 61. (a), (b) Raman spectra of Pristine CG (black line), MNSCG_L (gray line), and MNSCG_H (blue line).

Figure 62. (a) Current–voltage (*I*–*V*) curves of Pristine CG, MNSCG_L, and MNSCG_H. (b) Output properties of MNSCG_H sensor under various gate voltage (V_g, 0 to –0.6 V in a step of –0.1 V, and V_{sd}, 0 to –0.5 V in a step of –50 mV).

Figure 63. Detection of H_2O_2 with diverse sensors using Pristine CG (black line), FMNS (red line), MNSCG_L (gray line), and MNSCG_H (blue line). (a) Real-time measurements and (b) calibration curves toward various H_2O_2 concentrations (1 nM to 10 μM).

Figure 64. Schematic illustration depicting H_2O_2 sensing mechanism of MNSCG sensor based on non-enzymatic reaction.

Figure 65. (a) Selective response of MNSCG sensor toward target H_2O_2 (1 nM) and non-target biomolecules (uric acid (UA) and ascorbic aicd (AA), 1 μM). (b) Reusability of non-enzymatic MNSCG sensor upon the first (black) and tenth (red) addition of 1 μM H_2O_2.

Figure 66. FE-SEM images of MNSCG after (a) the first and (b) the tenth addition of 1 μM H_2O_2.

List of Tables

Table 1. Zeta potential measurements for FMNS samples.

Table 2. Sensing performance compared with previous researches using electrochemical method.

Table 3. Inductively Coupled Plasma-Atomic Emission Spectrometer (ICPS) analysis for Han River.

Table 4. H_2O_2 sensing performance of this work compared with previous studies.

Table of Contents

Abstract ..... **i**

List of Abbreviations ..... **iii**

List of Figures ..... **ix**

List of Tables ..... **xix**

Table of Contents ..... **xx**

1. Introduction **1**

1.1 Background **1**

1.1.1 Biosensors 1

1.1.1.1 Recognition elements 4

1.1.1.2 Electrochemical sensing method 5

1.1.2 Transducer materials 9

1.1.2.1 CVD graphene 9

1.1.2.2 Transition metal dichalcogenide 13

1.1.2.3 Conducting polymers 16

1.1.3 Biosensor applications 19

1.1.3.1 Hepatitis B virus sensor 19

1.1.3.2 Taste sensor 20
1.1.3.3 Arsenic sensor 21
1.1.3.4 H_2O_2 sensor 23

1.2 Objectives and Outlines 25
1.2.1 Objectives 25
1.2.2 Outlines 25

2. Experimental Details 28

2.1 Fabrication of flexible graphene aptasensor for hepatitis B virus detection 28
2.1.1 Fabrication of CVD graphene 28
2.1.2 Fabrication of hepatitis B sensor based on binding aptamer-conjugated graphene electrodes 29
2.1.3 Preparation of saliva sample 30
2.1.4 Characterization of hepatitis B sensor based on binding aptamer-conjugated graphene electrodes 30
2.1.5 Instruments for the hepatitis B sensor 31

2.2 Fabrication of duplex bioelectronic tongue based on multiplexed graphene electrodes for sensing umami and sweet tastes 32
2.2.1 Fabrication of CVD graphene on SiO_2 wafer substrate 32

2.2.2 Fabrication of duplex graphene electrodes 33
2.2.3 Immobilization of nanovesicles on the DGE surface..... 34
2.2.4 Preparation of target tastants..... 34
2.2.5 Characterization of duplex bioelectronic tongue based on multiplexed graphene electrodes..... 35
2.2.6 Sensing measurements for the umami and sweet taste sensor 36

2.3 Fabrication of highly sensitive FET-type aptasensor using flower-like MoS_2 nanospheres for real-time detection of arsenic(III)..... 37
2.3.1 Materials..... 37
2.3.2 Fabrication of flower-like MoS_2 nanospheres 37
2.3.3 Fabrication of carboxylated polypyrrole-coated FMNSs... 38
2.3.4 Fabrication of FET-type aptasensor for As(III) detection . 39
2.3.5 Instrumentation for the FET-type aptasensor..... 39
2.3.6 Sensing measurements for the As(III) aptasensor..... 40

2.4 Fabrication of H_2O_2 sensor based on MoS_2 nanosheets grown on CVD graphene..... 41
2.4.1 Materials..... 41
2.4.2 Preparation of CVD graphene..... 41
2.4.3 Fabrication of MoS_2 nanosheets grown on the graphene substrate 42

2.4.4 Characterization of MoS_2 nanosheets grown on the graphene substrate 43
2.4.5 Instruments for the H_2O_2 sensor..... 44

3. Results and Disccusions 45

3.1 Fabrication of flexible graphene aptasensor for hepatitis B virus detection 45
3.1.1 Fabrication of graphene based-aptasensor for hepatitis B virus detection 45
3.1.2 Characterization of flexible CVD graphene electrodes 49
3.1.3 Characterization of aptamer-immobilized graphene electrodes..... 53
3.1.4 Electrical properties of FET-type hepatitis B aptasensor... 56
3.1.5 Real-time responses of FET aptasensor toward HBsAg.... 60
3.1.6 Real-time responses of FET aptasensor toward real samples 66

3.2 Fabrication of duplex bioelectronic tongue based on multiplexed graphene electrodes for sensing umami and sweet tastes 70
3.2.1 Fabrication of duplex bioelectronic tongue 70
3.2.2 Characterization of duplex bioelectronic tongue 74
3.2.3 Electrical properties of duplex bioelectronic tongue 81

3.2.4 Real-time responses of the DBT for umami tastant 84
3.2.5 Real-time responses of the DBT for umami tastant in artificial seasonings 89
3.2.6 Real-time responses of the DBT for sweet tastant 91
3.2.7 Dual responses of the DBT for umami and sweet tastants 95

3.3 Fabrication of highly sensitive FET-type aptasensor using flower-like MoS_2 nanospheres for real-time detection of arsenic(III) 99
3.3.1 Fabrication of carboxylated polypyrrole-coated FMNSs... 99
3.3.2 Characterization of FMNSs..... 106
3.3.3 Characterization of CFMNSs..... 112
3.3.4 Immobilization of aptamers on CFMNS surfaces..... 117
3.3.5 Electrical characteristics of CFMNSs 121
3.3.6 Real-time responses of CFMNS aptasensor toward arsenite 125
3.3.7 Real-time response of MoS_2 based-aptasensor toward a real sample..... 131

3.4 Fabrication of H_2O_2 sensor based on MoS_2 nanosheets grown on CVD graphene..... 135
3.4.1 Fabrication of MoS_2 nanosheets grown on graphene substrate..... 135
3.4.2 Characterization of MNSCG..... 139

3.4.3 Electrical properties of MNSCG 146
3.4.4 Real-time responses of FET-type H_2O_2 biosensor based on MNSCG electrode 149
3.4.5 Selective response and reusability of MNSCG sensor 154

4. Conclusion 158

Reference 164

국문초록 177

1. Introduction

1.1 Background

1.1.1 Biosensors

Biosensors are analytical devices combined with biological sensing elecments, and they are used for the monitoring of target analytes with physicochemical detectors [1-3]. Biosensors detect a chemical, physical, or biological change that occurs *via* specific interaction between a recognition element and target analyte, and then convert the change into a measurable signal (**Figure 1**) [3,4]. Biosensors have received great deal of attention from researchers in analytical chemistry due to their potential for a wide range of appications. Biosensors are now being used in medical diagnosis, drug delivery, food monitoring, drink-water safety, environmental checking, protein engineering, DNA detection, toxicity assessment, and other bio-applications [5-10].

Biosensor's performance is evaluated based on its various sensing properties such as sensitivity, selectivity, minimum detectable level, response time, reusability, detection range, thermal and physical stability,

and storability. Recently, considerable efforts have been made to enhance biosensor's sensing abilities because there is still room for improvement.

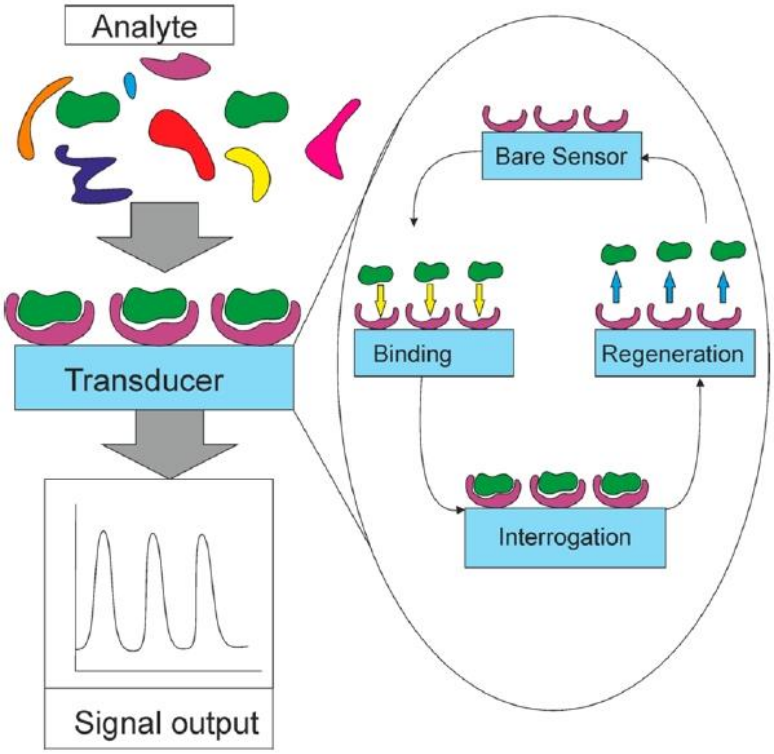

Figure 1. Schematic of biosensor operation (left) and regeneration (right). [3]

1.1.1.1 Recognition elements

Biosensors can accurately detect target analytes by using recognition elements. The receptors enable selective response to particular analytes through specific interactions, leading to minimized interferences from other non-target components. To improve sensing performance, various receptors such as enzymes, antibodies, cells, protiens, nucleic acids, aptamers, conducting polymers, and metals have been studied [11-17]. Aptamers have attracted much attention due to their ability to interact distinctly with target analytes with high affinity in a similar way to antibodies. Aptamers consist of artificial single-stranded RNA or DNA oligonucleotides that have outstanding selectivity, easy modification with functional groups, and commercial availability [18]. Moreover, aptamers represent advantages over antibodies, including better solubility, thermal stability, and low production costs [19]. To utilize these attractive characteristics, various aptamer-functionalized biosensors have been developed for diverse analytes [20-23]. G protein-coupled receptors (GPCRs) are a family of membrane-bound proteins that mediate a number of physiological processes such as sensory signaling, cell signal transduction, and hormonal signaling. GPCRs transmit signals from extracellular binding of various ligands to

intracellular signaling molecules [24,25]. Notably, human GPCRs derived from human receptors are attractive recognition elements due to their ability to mimic human system with human-like performance [26-28].

1.1.1.2 Electrochemical sensing method

Electrochemical sensing method is a very promising and powerful tool for high-performance biosensors. Electrochemical biosensors recognize a measurable electrical signal through a transducer. **Figure 2** illustrates a biosensor system with electrochemical transducer. Electrical change occurs when a biological sensing element reacts with target analyte, and the change can be related to the concentration of the analyte [29]. From the viewpoint of sensing methods, electrochemical biosensors have beneficial advantages such as extraordinary sensitivity, low power consumption, simple instrumentation, inexpensive cost and short analysis time [30,31].

Among electrochemical biosensors, field-effect transistor (FET)-based sensors are attractive candidates due to their ability to rapidly and sensitively detect analytes *via* efficient interfacial transfer of charge carriers [32-34]. A FET-type biosensor is generally made up of a

recognition element and a semiconducting FET that acts as a transducer. The FET, which consists of source (*S*), drain (*D*), and gate (*G*) electrodes, is a transistor that utilize an electric field to control the electrical property of the biosensor. The variation of gate voltage can change the amount of current that can flow between the source and drain electrodes. The electrostatic surface potential of the transducer is altered when analytes bind to receptors. This change in the surface potential alters charge distribution at the transducer surface, which acts like gate voltage modulation. In addition, FET-type sensors achieve excellent current amplification and improved signal-to-noise (S/N) ratio [35,36]. Various materials can be applied to transducers in liquid-ion gated FET geometry operated in the solution state through the gate dielectric [37-41]. **Figure 3** presents schematic illustration of the liquid-ion gated FET geometry. Liquid-ion gated FET biosensors have demonstrated rapid responses with low-voltage operation and improved signal transduction, leading to high sensing performance as well as real-time detection [42-45].

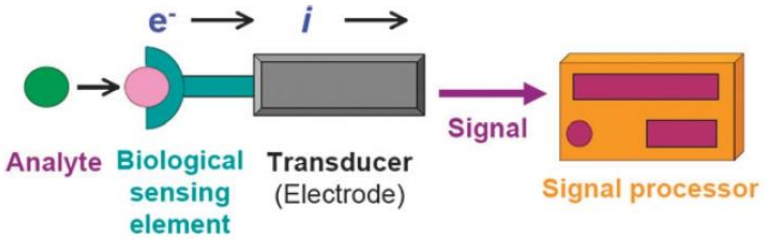

Figure 2. A schematic of a biosensor with electrochemical transducer. [29]

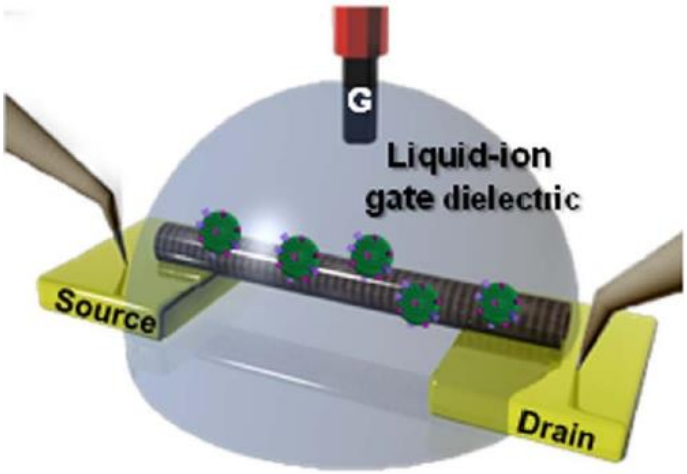

Figure 3. Schematic illustration of the liquid-ion gated FET-type biosensor. [39]

1.1.2 Transducer materials

Electrochemical transducer reacts to binding interactions and converts electrical response to a signal output that can be amplified, stored, and displayed [29]. Transducers play a pivotal role in improving sensing performance. From a material viewpoint, the characteristics of transducer materials significantly affect the performance of biosensors [46]. Accordingly, it is important to develop and utilize innovative transducer materials for biosensor applications.

1.1.2.1 CVD graphene

Graphene is two-dimensinal (2D) structures with hexagonal honeycomb lattice and comprises single- or few- layer of sp^2-hybridized carbon atoms. Crystalline graphene can become a semi-metal or zero-gap semiconductor, enabling graphene applications for electronic devices. In particular, graphene reveals a powerful ambipolar electric field effect. This implies that charge carriers can be tuned between electrons and holes in concentrations as high as 10^{13} cm^{-2} and room-temperature mobilities of 10,000 cm^2 V^{-1} s^{-1} can be achieved by applying gate voltage [47]. The Fermi level of graphene decreases below the Dirac point under negative gate bias, leading to many holes into the valence

band. Graphene has grabbed substantial focus due to its extraordinary thermal, mechanical, and electrical properties [48]. Because of these properties, it has recently become the subject of considerable research interest for a wide range of applications, including supercapacitors, electronic devices, solar cells, transparent conducting electrodes, and biosensors [49-56]. There are various methods (e.g., chemical vapor deposition (CVD), liquid-phase exfoliation, epitaxial growth, and mechanical exfoliation) being used to prepare graphene. Among different preparation approaches, CVD method has received enormous attention because of its high quality and low price (**Figure 4**) [57]. Large-area CVD graphene with low contact resistance can be synthesized by deposition and pyrolysis of hydrocarbon precursors (e.g. methane). CVD graphene has been investigated as a transducer in analytical methodologies, showing high sensitivity, selectivity, and rapid response/recovery times owing to extraordinary carrier mobility and high conductivity [58.59]. In addition, CVD graphene transferred onto flexible substrates can provide transparent and flexible platform for biosensor applications. **Figure 5** depicts wet-transfer of CVD graphene onto a flexible substrate [59]. From these attractive advantages,

graphene-based substrate is a promising structure for high-performance biosensors.

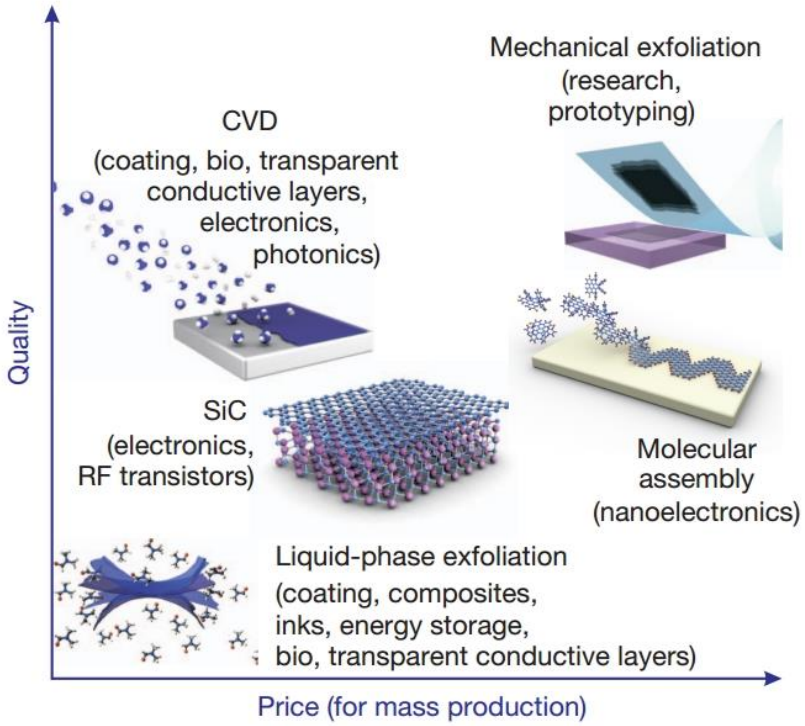

Figure 4. There are several methods of mass-production of graphene, which allow a wide choice in terms of size, quality and price for any particular application [57].

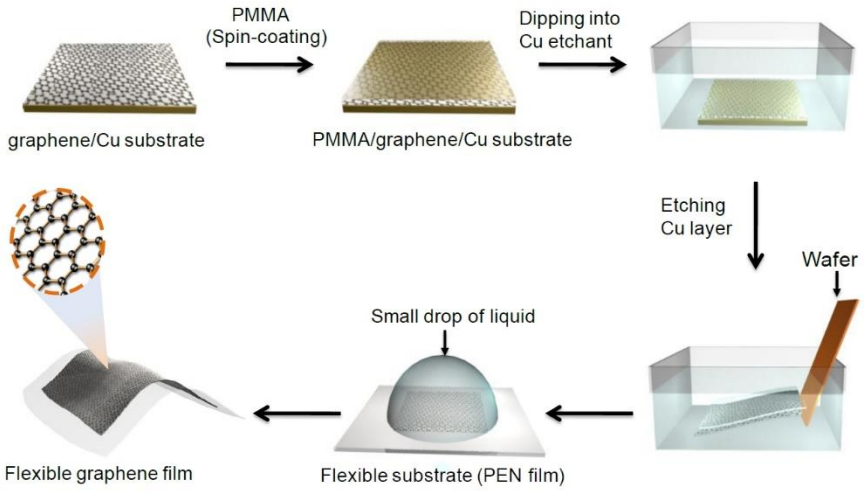

Figure 5. Wet−transfer method of the graphene on the flexible substrate [59].

1.1.2.2 Transition metal dichalcogenide

Transition metal dichalcogenides (TMDs) are graphene-like 2D layered materials, and consist of vertically stacked layers bonded by van der Waals forces. Each layer is composed of a transition metal atom sandwiched between two hexagonal lattices of chalcogen atoms. The atoms in a single layer are held together by strong covalent bonds [60]. TMDs have drawn increasing interest in diverse applications owing to their unique electrical, magnetic, mechanical, and optical properties [61-63]. A large surface area of TMD is obtained when bulk structure is thinned down into few layers, resulting in high density of edges which are potential active sites for electrochemical interactions [64]. TMDs are semiconducting materials with an intrinsic bandgap and show excellent electrostatics [65]. The bandgap in most semiconducting TMDCs, whether in bulk or monolayer, are comparable to the 1.1-eV bandgap in silicon, making them suitable for use in digital transistor [61]. In addition, TMDs exhibits low on/off swiching ratios. These properties enable TMDs to be utilized for highly scalable FETs.

Recently, there has been much interest in using TMDs for sensor applications due to their electron- and proton-accepting behavior. Molybdenum disulfide (MoS_2), which is a layered TMD, features a

hexagonal lattice with the Mo and S_2 atoms [66]. **Figure 6** illustrates the atomic structure of layered MoS_2. Notably, MoS_2 has a large surface-to-volume ratio, good carrier mobility, and a low noise level [67,68]. Gas sensors using MoS_2 transducers have been studied extensively due to their impressive performance with low power consumption [69-72]. However, relatively little research has been conducted using MoS_2 transducers for biosensors, although some MoS_2-based biosensors for protein or DNA have been reported [73,74]. Therfore, the appication of MoS_2 transducers for biosensors is still challenging and of particular interest.

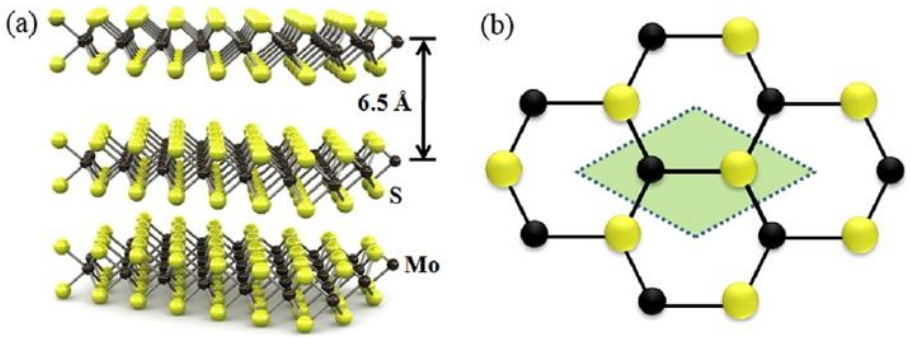

Figure 6. (a) The atomic structure of layered MoS_2. Different sheets of MoS_2 are composed of three atomic layers S−Mo−S, where Mo and S are covalently bonded. (b) A top view of the honeycomb lattice [66].

1.1.2.3 Conducting polymers

During the last decades, conducting polymers (CPs) have instigated a lot of interest due to their superior electrical property, stability, and biocompatibility [75]. These characteristics of CPs originated from polyconjugated backbone which is comprised of alternating single (σ) and double (π) bonds [76]. Among organic materials, the electrical property of CPs is similar to that of inorganic semiconductors or metals. These excellent features make it attractive to use CPs for sensor transducers [77,78]. CPs are typically polymerized by chemical or electrochemical oxidation of monomers. Vapor deposition polymerization (VDP) method is one of promising strategies to synthesis CPs on a substrate. First, monomers are deposited onto surface by vaporization during VDP process, and then polymerization is achieved by thermal, chemical, photochemical, and other processes. VDP method can offer smooth and uniform CP layer onto the desired surface through the consecutive polymerization of vaporized monomer under a vacuum condition [79,80].

Compared with other CPs, polypyrrole (PPy) has favourable characteristics such as high electrical conductivity, redox property, and long-term stability [81]. PPy, which consists of five-membered

heterocyclic rings, shows different concnetrations of charge carrier depending on oxidation levels. **Figure 7** represents the electronic band model of PPy with three different structures [82]. Upon oxidation, polarons are created from valance band (neutral state). Subsequently, bipolarons generate according to the futher oxidation. Bipolarons can move through the rearrangement of single and double bonds in the conjugated structure, enabling charge transfer along the PPy backbone. PPy has high conductivity originated from the unique π-conjugated electronic system. The polymer backbones of PPy provide a superb pathway for charge flow during electrochemical processes [83]. Moreover, the functional groups of PPy derivatives play a pivotal role in engineering surface modifications. Therefore, some transducers are combined with PPy to improve sensing ability, and they demonstrates advanced performance [84-86].

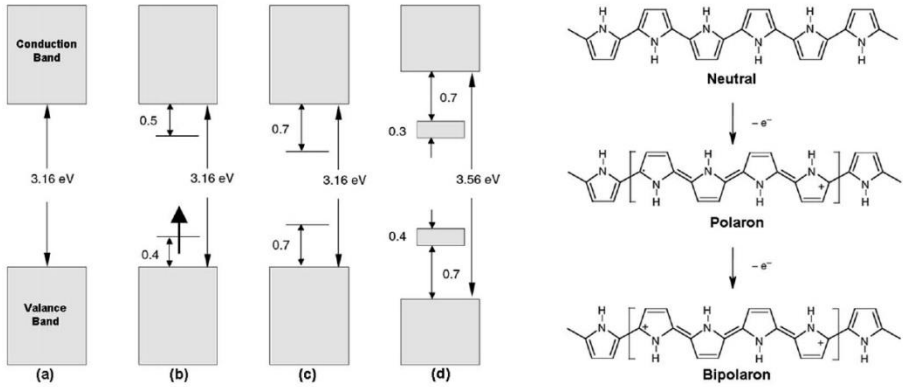

Figure 7. Electronic energy diagrams and structures for (a) neutral PPy, (b) polaron, (c) bipolaron, and (d) fully doped PPy [82].

1.1.3. Biosensor applications

1.1.3.1 Hepatitis B virus sensor

Persistent infection by hepatitis B virus (HBV) has been implicated in a number of fatal diseases such as chronic hepatitis, primary liver cancer, cirrhosis, and hepatocellular carcinoma [87]. The HBV infection influences almost one third of the world population. In addition, an estimated 250 million people are troubled with chronic disease, and more than 780 thousand people die every year from complications relevant to hepatitis B [88,89]. To improve safety, various analytical devices have been developed to detect HBV DNA or hepatitis B surface antigens (HBsAg) related to HBV, including colorimetric analysis, surface-enhanced Raman scattering, luminescence assay, and fluorescence sensors [90-95]. In particular, luminescence and fluorescence sensors have been widely used owing to the simplicity and high sensitivity. However, theses sensors have limitations including time-consuming process, sophisticated instruments, and multiple-step procudures. To date, among other sensors, electrochemical biosensors have received a great deal of attention because of their highly fast response, simple design, small dimensions, and low power consumption [96]. Lee *et al*. fabricated an electrochemical sensor based on hepatitis B antibody, and the sensor

demonstrated the successful detection of HBsAg [97]. However, is is still challenging to design stable sensors because the antibody shows poor thermal stability. Aptamers can be good alternatives to antibodies due to their high thermal stability, better solubility, easy synthesis and commercial availability [98]. Xi *et al*. synthesized DNA aptamers that specifically bind to HBsAg. They fabricated chemiluminescent aptasensor using the DNA aptamers. The aptasensor was highly specific in the detection of HBsAg.

1.1.3.2 Taste sensor

Artificial taste sensors, referred to as electronic tongues have triggered a lot of interest due to their ability to monitor food and beverage safety. The electronic tongues have utilized various materials, including polymers, chelators, aromatic compounds, and lipid membranes [99-103]. In addition, diverse sensing methods, such as fluoremetry, impedance analysis, pH sensing, and photoluminescence method, have been used to monitor tastants [104-107]. However, theses methods have significant disadvatages such as slow response time and time-consuming process. Although significant efforts have been made to artificial taste sensors, most previous electric tongues can not mimic the natural

characteristics of a human taste system. Humans tongue can discriminate five basic tastes: sweet, bitter, salty, sour, and umami through different functional receptors. These receptors are GPCRs or ion channels found on taste neurons. To mimic human system, some researches have been reported using human taste recetors, belonging to the family of GPCRs [108-109]. These researches have serious drawbacks of slow response and low sensitivity. Song *et al*. fabricated a nanomaterial-based sensor combined with human taste receptors [28]. The taste sensor recognized sweet tast which is one of five basic tastes and showed high sensitivity and selectivity. However, the sensor are unable to simultaneously discriminate more than two basic tastes.

1.1.3.3 Arsenic sensor

Arsenic (As) contamination in drinking water is becoming a serious problem in many countries due to its threat to human health [110]. Elevated arsenic levels can lead to skin damage, keratosis, heart disease, and circulatory system problems [111,112]. Moreover, many fatal cancers (e.g., skin, lung, bladder, kidney, and liver) are caused by drinking water containing arsenic [113]. Therefore, the World Health Organization (WHO) recommends that the limit of arsenic in drinking

water is below 10 ppb (133 nM, 10 μg/L) [114]. Arsenite (As(III)) and arsenate (As(V)) are the two most common forms of arsenic found in water. Arsenic(III) is the most toxic form and is 60-times more harmful than As(V) [115]. Considerable efforts have been made to develop innovative receptors for detecting As(III). Some receptors such as gold nanoparticles, Escherichia coli cells, and laccase have been developed to recognize As(III) [116-119]. However, difficult modifications and reactions are required to use these receptors, resulting in their limited application. Additionally, these materials feature a relatively low sensitivity and poor selectivity for detecting As(III). Therefore, there is a great need to develop highly stable, sensitive and selective receptors for As(III) sensors. Aptamers have attracted much attention due to their ability to interact distinctly with targets. Aptamers consist of artificial single-stranded RNA or DNA oligonucleotides. The arsenic-binding aptamer (named Ars-3) synthesized by Kim *et al*. has a high affinity to As(III) [120]. Some strategies have been proposed to selectively detect As(III) using Ars-3 [121-124]. However, real-time detection for As(III) remains a challenge; strategies to date suffer from slow responses and are time-consuming.

1.1.3.4 H_2O_2 sensor

Reactive oxygen species (ROS) are considered to be important intracellular signaling molecules because they regulate protein synthesis, DNA damage, cell apoptosis, etc [125]. The excessive accumulation of ROS can cause cell disruption, disease, and aging. Hydrogen peroxide (H_2O_2), a prominent representative of ROS, has strong oxidizing property, which allows it to be widely used pharmaceutical, clinic, environmental, mining, textile, food manufacturing, and chemical industries [126]. In living organisms, H_2O_2 is regarded as an unwanted byproduct in various biochemical reactions involving different oxidases. In addition, H_2O_2 penetrates into other cellular compartment due to its long life time, leading to diverse harmful modifications [127]. As an oxidative stress marker, H_2O_2 gives rise to diverse disease such as cancer, diabetes, Parkinson's, and Alzheimer's disorders. Therefore, H_2O_2 can be extremely harmful to human health and safety. Several sensing methods, including luminescent, colormetirc, and fluorescent measurements have been established to detect H_2O_2 [128-132]. However, theses methods have considerable drawbacks associated with response time. To solve the problem, electrochemical sensors have been proposed by using different kinds of sensing materials such as enzyme, metal, metal oxide, CNT,

HRP, and graphene [133-137]. Recently, MoS_2 has been used as effective sensing material for H_2O_2 monitoring [138-140]. The MoS_2-based non-enzymatic sensors are sensitive and selective enough to detect H_2O_2.

1.2 Objectives and Outlines

1.2.1 Objectives

In the proceding section, the significance of graphene and molybdenum disulfide nanomaterials was presented from the viewpoint of academic achievement and practical sensor applications. The aim of this dissertation is to introduce the fabrication of graphene and MoS_2-based biosensors and to describe their electrical properties. Moreover, their application areas are also demonstrated, including hepatitis B virus, taste, arsenic, and H_2O_2 sensors.

1.2.2 Outline

This dissertation involves the following subtopics:

I. High-performnace flexible graphene aptasensor for hepatitis B virus detection
   1. Fabrication of CVD graphene electrodes on flexible PEN substrate.
   2. Construction of hepatitis B sensor based on binding aptamer-conjugated graphene electrodes
   3. Application for FET-type hepatitis B surface antigen sensor

II. Duplex bioelectronic tongue for sensing umami and sweet tastes based on multiplexed graphene electrodes

1. Preparation of duplex graphene electrodes *via* photolithography process
2. Fabrication of bioelectronic tongue based on taste receptor-conjugated duplex graphene electrodes
3. Real-time responses of taste sensor

III. Highly sensitive FET-type aptasensor using flower-like MoS_2 nanospheres for real-time detection of arsenic(III)

1. Preparation of MoS_2 nanospheres *via* hydrothermal synthesis
2. Control of morphology under different synthetic conditions
3. Application for arsenic(III) sensor

IV. Hydrogen peroxide sensor based on MoS_2 nanosheets grown on CVD graphene

1. Preparation of MoS2 nanosheets on CVD graphene *via* hydrothermal synthesis
2. Real-time responses of biosensor based on MoS_2 and graphene

for H_2O_2 detection

3. Application for arsenic(III) sensor

2. Experimental Details

2.1 Fabrication of flexible graphene aptasensor for hepatitis B virus detection

2.1.1 Fabrication of CVD graphene

The single layer graphene was fabricated by chemical vapor deposition (CVD) method and it was grown on Cu substrate (25 μm-thick) using CH_4, H_2 gases as carbon source in the cylindrical furnace. The CVD process was as follows: (1) Place the Cu foil in the furnace, evacuate, and introduce 8 sccm flow of H_2 at 90 mTorr for 30 min. (2) Heat to 1000 °C from room temperature, maintaining the elevated temperature for 30 min. (3) Introduce CH_4 at 20 sccm flow and 560 mTorr total pressure for 30 min. (4) Cool the furnace at 40 °C min^{-1} to room temperature. For the wet-transfer method, PMMA solution was coated on the frontside of graphene/Cu substrate by spin-coating process. Subsequently, the backside of the substrate is treated with O_2 plasma in order to etch the Cu substrate. The underlying Cu substrate was then removed using copper etchant, $H_2O/H_2O_2/HCl$ (5:1:1) solution, and $H_2O/H_2O_2/NH_4OH$ (5:1:1) solution, and then washed by distilled water.

Finally, the PMMA-coated graphene was transferred from the water to the flexible polyethylene naphthalate (PEN) film. To remove the PMMA layer, the sample was dealt with acetone vapor for 10 min, and then was immersed in acetone at 60 °C for 3 hr.

2.1.2 Fabrication of hepatitis B sensor based on binding aptamer-conjugated graphene electrodes

To build the FET-type aptasensor into liquid-ion gated device, gold electrodes (W/L = 20; L = 200 μm channel length) were deposited on the graphene film. 10-nm-thick chrome and 90-nm-thick gold were deposited sequentially on the graphene film by thermal evaporation. Subsequently, the graphene film with deposited gold electrodes was dipped in 0.005 M or 0.05 M DAN with methanol for 1 hr. The structure was exposed to 20 μL of 2% GA dissolved in PBS for 2 h, and then the modified graphene film was washed using phosphate buffered solution (PBS). Finally, the treated graphene substrate was exposed to 100 nM aptamer solution for 6h (40μL) and then rinsed with PBS. The aptamer sequence was 5'-GGG AAT TCG AGC TCG GTA CCC ACA GCG AAC AGC GGC GGA CAT AAT AGT GCT TAC TAC GAC CTG CAG GCA TGC AAG CTT GG-amine-3' [98].

2.1.3 Preparation of saliva sample

Artificial saliva solution was prepared as biological sample. The solution has the following composition: 0.1 L each of 25 mM K_2HPO_4, 24 mM Na_2HPO_4, 150 mM $KHCO_3$, 1.5 mM $MgCl_2$, 100 mM NaCl, 5 mM $CaCl_2$, and 0.006 L of 25 mM citric acid. The pH of the solution was regulated at 7.4 by the introduction of HCl [141]. Then, Hepatitis B surface antigen, as a target analyte, was solubilized in the saliva solution at various concentrations.

2.1.4 Characterization of hepatitis B sensor based on binding aptamer-conjugated graphene electrodes

The surface image of the graphene electrode was acquired using a Field Emission-Scanning Electron Microscope (FE-SEM, JEOL-6700F). The High Resolution-Transmission Electron Microscopy (HR-TEM) image was observed from a JEOL JEM-3010 instrument installed at the National Center for Inter-university Research Facilities at Seoul National University. The spectrophotometer (Thermo SCIENTIFIC, model NanoDrop 2000/2000c) was used for measuring the concentration of immobilized aptamer on the modified graphene surface. UV-Vis

absorbance spectrum was observed by using a Lambda-35 spectrometer (Perkin-Elmer, Waltham, MA, USA). Raman spectrum was recorde with a Horiba Jobin-Yvon LabRam Aramis spectrometer. The 514.5 nm line of an Ar-ion laser was used as the excitation source.

2.1.5 Instruments for the hepatitis B sensor

All electrical measurements were operated with a Keithley 2612A SourceMeter and probe station (MS TECH, Model 4000). To utilize solution-based measurements, a solution chamber (200 μL volume) was designed and used. Electrical current change was normalized as $\Delta I/I_0 = (I - I_0)/I_0$, where I_0 is the initial current and I is the detected current for real-time responses.

2.2 Fabrication of duplex bioelectronic tongue based on multiplexed graphene electrodes for sensing umami and sweet tastes

2.2.1 Fabrication of CVD graphene on SiO_2 wafer substrate

The single layer graphene was synthesiszed by chemical vapor deposition (CVD) process and it was grown on Cu foil. The foil was introduced in the furnace chamber, and the furnace was evacuated. Then, 8 sccm flow of H_2 at 90 mTorr was introduced for 30 min. The furnace was heated from the ambient temperature up to 1000 °C and maintained at 1000 °C for 30 min. Subsequently, 20 sccm flow of CH_4 gas as the carbon source was introduced at a pressure of 560 mTorr for 30 min. The furnace was then cooled at 40 °C min^{-1} to ambient temperature. For the transfer process, PMMA as a supporting layer was coated on the surface of the graphene/Cu substrate and then cured. To etch the Cu substrate, the backside of the substrate is dealt with O_2 plasma (100W, 40 s). The underlying Cu substrate was then removed using copper etchant, hydrochloride solution, and ammonia solution. Thereafter, the PMMA-coated graphene was transferred to the SiO_2 wafer substrate. To remove the PMMA layer, the sample was treated with acetone vapor for 10 min, and then was dipped in acetone at 60 °C for 2 hr. Finally the PMMA-

coated graphene substrate was annealed to remove PMMA residue at 500 °C for 3 h under gas mixtures of hydrogen (200 sccm) and argon (500 sccm).

2.2.2 Fabrication of duplex graphene electrodes

Duplex graphene electrodes (DGEs) were prepared using a typical photolithography process as follows. To remove the surface moisture, the as-prepared graphene substrate was heated at 120 °C for 5 min. The graphene substrate was coated with a GXR601 photoresist by the spin-coating at 4000 rpm for 30 s. After coating, the photoresist contained a certain amount of solvent. The soft bake process was conducted at 100 °C for 90 s to dry the solvent, leading to stable condition by reducing the excess solvent. Then, square patterns were created by exposure to UV light using photolithography (Karl-Süss, MA-6). The exposure time was optimized for 4 s. To reduce the standing wafe effect, the hard bake process was performed 120 °C for 60 s. Subsequently, an AZ300 remover was used for the development process (30 s). Unpatterned region of the graphene substrate was etched by the reactive ion etching (RIE) process (Oxford Instruments), and then acetone solvent was used to remove the patterned photoresist. This graphene patterns were utilized

for the channel region of DGEs. Afterward, second photolithography process was conducted to fabricate the patterns of contact electrode. Finally, the contact electrodes were deposited by the thermal evaporation of Cr/Au (10 nM/40 nM) with a 1 Å/s deposition rate and lift-off method.

2.2.3 Immobilization of nanovesicles on the DGE surface

The prepared DGEs were exposed to 1 mM 1-pyrenebutanoic acid *N*-hydroxysuccinimidyl ester (PSE) solution in methanol for 30 min at room temperature, and then the DGEs were rinsed with pure methanol and modified through π-stacking between the pyrene groups of the PSE and the surface of the graphene. To immobilize taste receptor nanovesicles on the surface of the DGEs, the modified DGEs were dipped in nanovesicle solution for 3 h. The taste nanovesicles were provided by my co-worker whose name is Ahn, sae ryun [142]. The succinimidyl groups of the PSE interacted with the proteins of the nanovesicles, forming peptide bonds. As a result, taste nanovesicles were successfully immobilized on the surface of the DGEs.

2.2.4 Preparation of target tastants

Umami and sweet tastants were obtained from Sigma-Aldrich.

Tastants were diluted in Dulbecco's phosphate buffered saline (DPBS, Gibco, USA) at different concentrations. The artificial seasoning 1 had the following composition: salt, sugars, flavor raw material, yeast extract, wheat protein seasoning, and yeast extract fermented seasoning (such as amino acids). The artificial seasoning 2 contained 97.3% MSG, 1.35% IMP, and 1.35% GMP. These artificial seasonings were purchased commercially and dissolved in pure water. Tomato juice was also purchased and the composition was as follows: tomato juice, purified water, liquid exaggeration, citric acid, synthetic flavors, cellulose gum, rock pigments, and vitamin C and sucrose was added to it at 100 μM. To prepare green tea sample, a green tea bag was immersed in 100 mL of water and heated at 90 °C for 5 min, and sucrose was added (1 mM).

2.2.5 Characterization of duplex bioelectronic tongue based on multiplexed graphene electrodes

The taste nanovesicle images were obtained using a Field Emission-Scanning Electron Microscope (FE-SEM, JEOL-6700F). Graphene layer was imaged with a high-resolution transmission electron microscopy (HR−TEM) from a JEOL JEM−3010. Raman experiment was performed using a Horiba Jobin-Yvon LabRam Aramis spectrometer. The 514.5 nm

line of an Ar-ion laser was utilized as the excitation source.

2.2.6 Sensing measurements for the umami and sweet taste sensor

A Keithley 2612A semiconductor analyzer, a probe station (MS TECH, model 4000), and a multichannel system (ONTEST Co.) were used to measure the electrical performance of the DBTs. DPBS containing 2 mM $CaCl_2$ at pH 7.4 was utilized as the electrolyte. Then, the DPBS was placed in a glass chamber (200 μL volume). Electrical current signal was detected and normalized as $\Delta I/I_0 = (I - I_0)/I_0$, where I is the detected real-time current and I_0 is the initial current.

2.3 Fabrication of highly sensitive FET-type aptasensor using flower-like MoS_2 nanospheres for real-time detection of arsenic(III)

2.3.1 Materials

$(NH_4)_2MoS_4$, $N_2H_4 \cdot H_2O$, As_2O_3, and NaOH were obtained from the Aldrich Chemical Company. As(III) solution was prepared by dissolving As_2O_3 in NaOH solution. Pyrrole (98%) monomer, pyrrole-3-carboxylic acid, and $FeCl_3$ were also purchased from the Aldrich Chemical Company. The Ars-3 aptamer was purchased from Bioneer Co. (Daejeon, Korea). Its sequence was 5'-amine-GGT AAT ACG ACT CAC TAT AGG GAG ATA CCA GCT TAT TCA TTT TAC AGA ACA ACC AAC GTC GCT CCG GGT ACT TCT TCA TCG AGA TAG TAA GTG CAA TCT-3' [120].

2.3.2 Fabrication of flower-like MoS_2 nanospheres

Flower-like nanospheres were synthesized by a hydrothermal method as reported previously with modification [143]. First, $(NH_4)_2MoS_4$ powder (0.165 g) was dissolved in deionized water (72 mL) with vigorous stirring and bath sonication to prepare a homogeneous solution. Then, the aforementioned solution was mixed with various

quantities (0.75–3.75 mL) of $N_2H_4 \cdot H_2O$ by sonication for 30 min. After that, the as-prepared solution was transferred into a 150-mL Teflon-lined stainless steel autoclave and treated at 200 °C for 12 h. The autoclave reactor was allowed to naturally cool down to room temperature. The black product was obtained by centrifugation, washed several times with deionized water and ethanol, and then dried for 12 h at 60 °C. Finally, the black powder was placed in a vacuum furnace and heated in flowing argon gas at 600 °C and a flow rate of 300 sccm for 1 h. After the annealing process, flower-like MoS_2 nanospheres (FMNSs) were obtained.

2.3.3 Fabrication of carboxylated polypyrrole-coated FMNSs

Carboxylated polypyrrole-coated FMNSs (CFMNSs) were fabricated by the vapor deposition polymerization (VDP) method. The above-prepared FMNSs were immersed into 0.1 M ethanolic ferric chloride ($FeCl_3$) solution for 10 min. The immersed FMNSs were dried in an oven under vacuum and moved into a reactor. Subsequently, the liquid monomer (0.18 mmol pyrrole-3-carboxylic acid) was injected into the reactor when the internal pressure was reduced to 0.1 Torr. Chemical oxidation polymerization was achieved after placing the reactor in the

electric oven at 100 °C for 15 min. This provided a coating of CPPy on the FMNS surface.

2.3.4 Fabrication of FET-type aptasensor for As(III) detection

To build the FET-type aptasensor configuration, interdigitated array (IDA) substrate was dipped in 3 wt% aqueous 3-aminopropyltrimethoxysilane (APS) solution for 12 h. The amino-modified IDA was treated with a mixed solution of 5 wt% aqueous CFMNSs solution (30 μL) and 1 wt% aqueous 4-(4,6-dimethoxy-1,3,5-triazin-2-yl)-4-methylmorpholinium chloride (DMT-MM) solution (20 μL) over 12 h. The CFMNS-immobilized substrate was washed with distilled water. To introduce the arsenic-binding aptamer on the surface of the CFMNSs, the modified substrate was exposed to a mixture of 1 μM aptamer solution (40 μL) and 1 wt% aqueous DMT-MM solution (10 μL) for 6 h. Finally, the aptasensor was rinsed with distilled water, and then dried at room temperature.

2.3.5 Instrumentation for the FET-type aptasensor

Field-emission scanning electron microscope (FE-SEM) (JEOL, JSM-6700F), transmission electron microscope (TEM) (JEOL, JEM-

200CX) and high-resolution transmission electron microscope (HR-TEM) (JEOL, JEM-3010) were used to visualize the material morphologies. X-ray diffraction (XRD) and X-ray photoelectron spectroscopy (XPS) spectra were acquired using an M18XHF SRA (MAC Science Co.) and an AXIS-His (KRATOS). FTIR data were obtained using a Spectra 400 (Perkin Elmer). Spectrophotometer (Thermo SCIENTIFIC, model NanoDrop 2000/2000c) was used to determine the concentration of immobilized aptamer. Zeta-potential measurements were obtained using electrophoretic light scattering spectrophotometer (Otsuka, ELS-8000).

2.3.6 Sensing measurements for the As(III) aptasensor

All electrical performance were measured with Keithley 2612A semiconductor analyzer and probestation (MS TECH, Model 4000). To build solution-based measurements, a glass chamber (200 μL volume) was designed and utilized. Electrical current change was normalized and defined as $\Delta I/I_0 = (I - I_0)/I_0$, where I_0 is the original current and I is the detected real-time current.

2.4 Fabrication of H_2O_2 sensor based on MoS_2 nanosheets grown on CVD graphene

2.4.1 Materials

Na_2MoO_4 and thiourea ($SC(NH_2)_2$) were obtained from the Aldrich Chemical Company. Hydrogen peroxide (H_2O_2) solution, uric acid, and L-ascorbic acid were also purchased from the Aldrich Chemical Company.

2.4.2 Preparation of CVD graphene

CVD graphene was fabricated by chemical vapor deposition (CVD) method and it was grown on Cu substrate. The foil was introduced in the furnace chamber, and the furnace was evacuated. Then, H_2 gas was introduced at 90 mTorr for 30 min. The flow rate of H_2 was maintained at 8 sccm. To anneal the Cu surface, the furnace chamber was heated up to 1000 °C and maintained at the elevated temperature for 30 min. Thereafter, CH_4 gas (20 sccm flow rate) as the carbon source was flowed at 560 mTorr pressure for 30 min. The reaction furnace was cooled at 25 °C min^{-1} rate from 1000 °C to room temperature. To perform the transfer procedure, PMMA layer was coated on the surface of the

graphene/Cu substrate and then cured at room temperature for 30 min. The O_2 plasma (100W, 40 s) was applied to the backside of the graphene substrate. Subsequently, the underlying Cu foil was etched by copper etchant, dilute hydrochloride, and ammonia solution. The PMMA-treated graphene was transferred to the SiO_2 wafer substrate. To clean the surface of wafer, the SiO_2 substrate was pretreated with piranha solution, IPA, methanol, and acetone. This graphene substrate was exposed with acetone vapor for 10 min, and then was immersed in acetone solvent at 60 °C for 2 hr. Then, the annealing process was conducted to remove PMMA residue at 500 °C for 3 h under hydrogen/argon mixture gas (200 sccm/500 sccm flow rate).

2.4.3 Fabrication of MoS_2 nanosheets grown on the graphene substrate

MoS_2 nanosheets were grown on a CVD graphene substrate by a hydrothermal method. First, the as-prepared graphene substrate was dipped in 0.001 M or 0.05 M DAN with methanol for 1 hr, and then the substrate was washed with methanol and distillated water. Then, Na_2MoO_4 powder (0.155 g) and thiourea (0.143g) as MoS_2 precursors were dissolved in deionized water (15 mL) with vigorous stirring for 50 min, and then the solution was sonicated in bath type sonicator for 10

min to obtain a homogeneous solution. Subsequently, the ae-prepared graphene sample and the aforementioned solution were transferred into a 50-mL Teflon-lined stainless steel autoclave, sealed tightly and heated at 130 °C for 12 h. After the hydrothermal reaction, the autoclave reactor was naturally cooled down to ambient temperature. The MoS_2-treated graphene sample was taken out and washed with deionized water, and then dried in an oven at 60 °C for 6 h. After that, the sample substrate was introduced in a vacuum furnace and heated up to 600 °C and maintained at the elevated temperature for 45 min under Ar gas (300 sccm). Finally, MoS_2 nanosheets grown on the graphene were prepared after the annealing process.

2.4.4 Characterization of MoS_2 nanosheets grown on the graphene substrate

To acquire the sample images, Field-Emission Scanning Electron Microscope (FE-SEM) (JEOL, JSM-6700F) and High-Resolution Transmission Electron Microscope (HR-TEM) (JEOL, JEM-3010) were utilized. X-Ray Diffraction (XRD) and X-ray Photoelectron Spectroscopy (XPS) spectra were obtained with an M18XHF SRA (MAC Science Co.) and an AXIS-His (KRATOS). Raman

measurements were investigated using LabRAM HV Evolution (HORIBA Co.). The 532 nm laser was used as the excitation source.

2.4.5 Instruments for the H_2O_2 sensor

Keithley 2612A SourceMeter and probe station (MS TECH, Model 4000) were used to measure all electrical properties. A solution chamber (200 μL volume) was designed and utilized for the solution-based measurements. Electrical current change was acquired and normalized as follows:

$\Delta I/I_0 = (I - I_0)/I_0$, where I_0 is the initial current and I is the monitored current for real-time responses.

3. Results and Discussions

3.1. Fabrication of flexible graphene aptasensor for hepatitis B virus detection

3.1.1 Fabrication of graphene based-aptasensor for hepatitis B virus detection

The single layer graphene was grown on a Cu foil *via* chemical vapor deposition (CVD) method with methane (CH_4) and Hydrogen (H_2) gas precursors. To remove the Cu foil, the etching process was performed, and the graphene was transferred onto a flexible polyethylene naphthalate (PEN) film. Subsequently, source (*S*) and drain (*D*) electrodes were deposited on the graphene-transferred PEN film through thermal evaporation. The gold electrodes were placed side by side and piled up uniform distance. **Figure 8** illustrates a schematic protocol for the fabrication of graphene-based aptasensor on a flexible PEN substrate. The graphene surface was chemically functionalized using 1,5-diaminonaphthalene (DAN), enabling the surface to be modified with amino groups. The DAN was placed on the surface of the graphene *via* π– π interaction between plane of the graphene and phenyl groups of the

DAN [144]. Thereafter, graphene-based aptasensors were successfully fabricated by the addition of binding aptamer after the introduction of glutaraldehyde (GA). The GA was used as effective cross-linking agent for immobilizing the aptamer on the graphene surface. The aptamer sequence was 5'-GGG AAT TCG AGC TCG GTA CCC ACA GCG AAC AGC GGC GGA CAT AAT AGT GCT TAC TAC GAC CTG CAG GCA TGC AAG CTT GG-amine-3'. This aptamer specifically interacted with hepatitis B virus surface antigen (HBsAg). From the viewpoint of chemical reactions, one aldehyde group of the GA was intreracted with the amine group of the DAN by the Schiff-base reaction [145]. Similarly, the other aldehyde group of GA was connected to the amine group at 3’ terminus of the aptamer, leading to the construction of stable-sensing elements even in the liquid state (**Figure 9**). Therefore, the Hepatitis B aptasensor (HAS) was successfully fabricated by surface modifications.

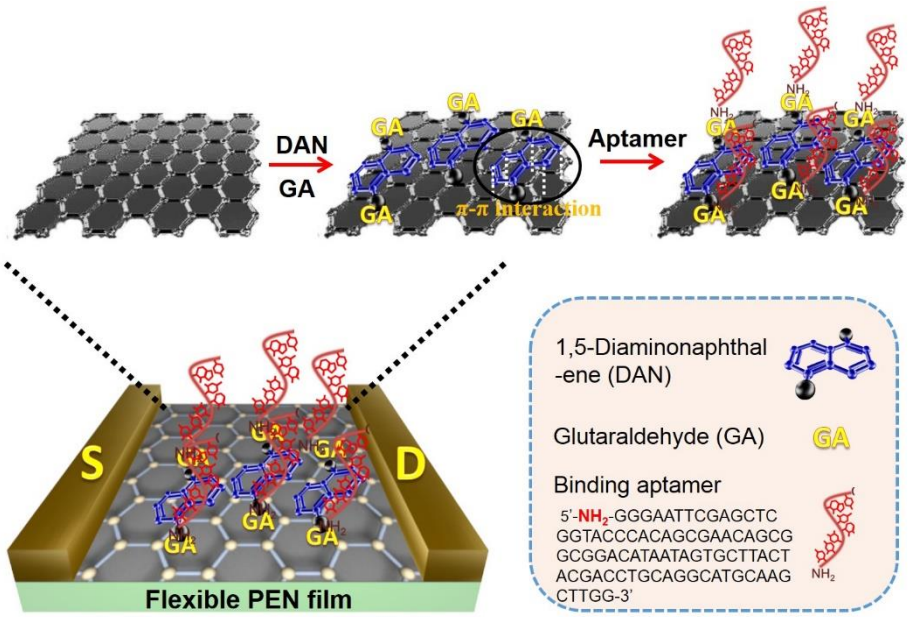

Figure 8. Synthetic procedure of flexible hepatitis B aptasensor on PEN film.

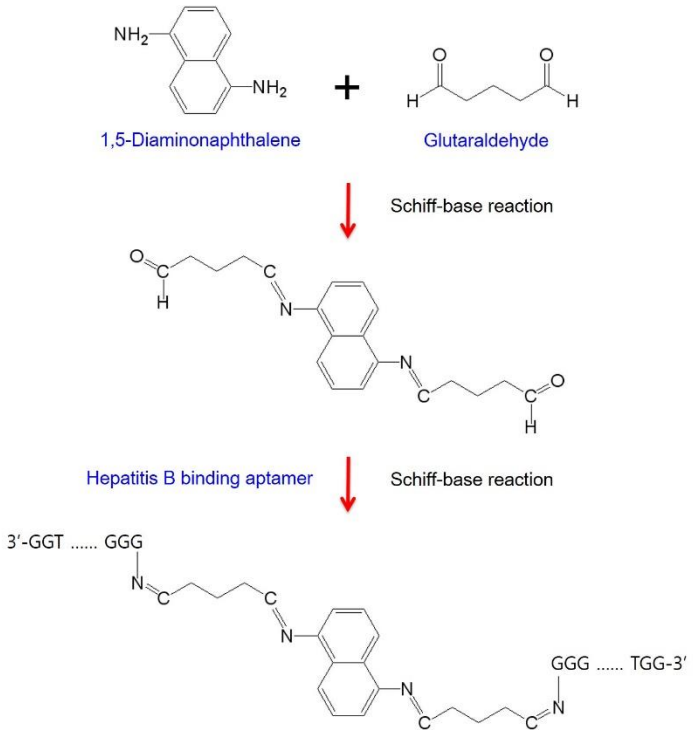

Figure 9. Chemical reactions among 1,5-diaminonaphthalene (DAN), glutaraldehyde (GA) and hepatitis B surface antigen binding aptamer.

3.1.2 Characterization of flexible CVD graphene electrodes

A single layer graphene, rather than double or few layer graphene, has been used for diverse electronic devices such as electrode and electrical transducer of biosensors because of its exceptional electrical and physical properties [146]. The number of graphene layers was characterized using Raman measurement. **Figure 10** displays the Raman spectrum over the range from 1250 to 2950 cm^{-1}. The G peak (*ca*. 1580 cm^{-1}) and 2D peak (*ca*. 2680 cm^{-1}) were the most distinctive characteristics of the Raman spectrum. In single layer graphene, the 2D peak is sharper and more intensive than the G peak [147,148], which is consistent with the spectrum as shown in **Figure 10**. This result demonstrated that single layer graphene was successfully fabricated *via* the CVD method. **Figure 11a** presents UV-visible spectra of the graphene film on a flexible PEN substrate. The optical transmittance (Tr) was measured at 550 nm and was found to be 97.7 %, which indicated that the thickness of the CVD graphene is similar to that of a single layer graphene [149]. As shown the photograph, the graphene film was highly transparent (**inset of Figure 11a**). The gold electrodes were deposited on the graphene film through thermal evaporation process. The graphene structure was maintained after the thermal process, implying that the

graphene had a good thermal stability. **Figure 11b** shows the flexible property of the prepared graphene electrode.

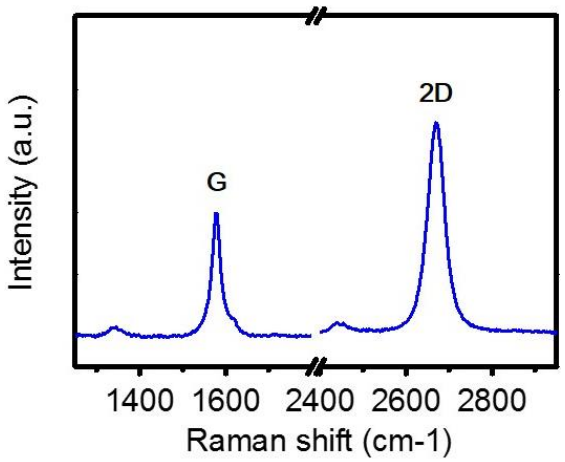

Figure 10. Raman spectrum of single layer graphene on a SiO_2 wafer substrate.

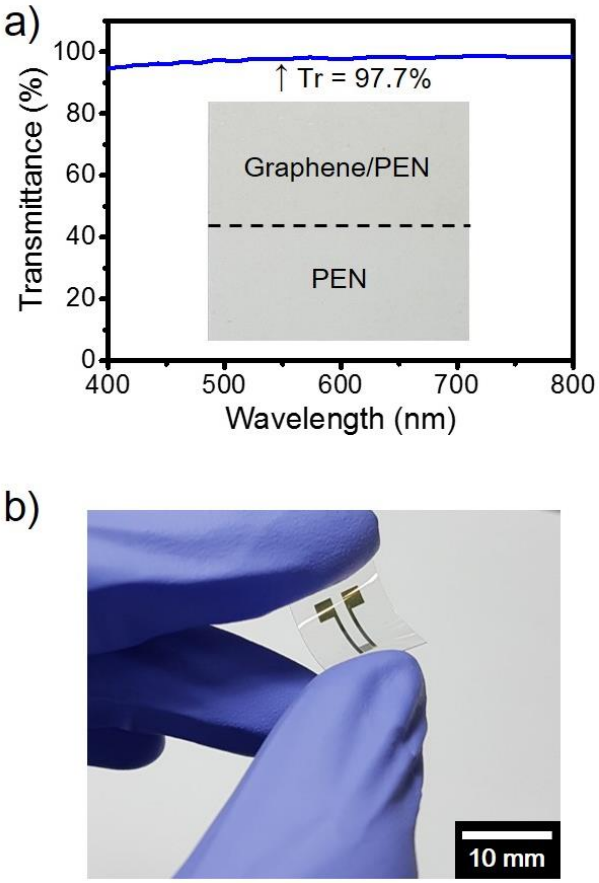

Figure 11. (a) UV–visible spectrum and photograph (inset) of single layer graphene transferred on PEN film (transmittance at 550 nm). (b) Flexible graphene platform with the gold electrodes.

3.1.3 Characterization of aptamer-immobilized graphene electrodes

To visualize immobilization of the aptamer on the graphene electrode modified with DAN and GA, a field-emission scanning electron microscopy (FE-SEM) measurement was conducted. **Figure 12a-c** represent FE-SEM images of the graphene surface before and after the immobilization of the binding aptamer. **Figure 12a** indicates that the pristine electrode surface is clear. **Figure 12b and c** display HAS_L and HAS_H samples pretreated with 0.001 M DAN and 0.05 M DAN, respectively. Both samples represent uneven surfaces because of the aptamer introduction. In particular, HAS_H has a rougher surface (**Figure 12b**) than HAS_L (**Figure 12c**). Presumably, a higher-concentration of DAN enabled more aptamers to be loaded on the graphene surface. To quantify the immobilized aptamers on the HAS_H and HAS_L samples, spectrophotometric measurements were carried out (**Figure 13**). The spectrophotometer used the Beer-Lambert equation to correlate the calculated absorbance with concentration. The results showed that *ca*. 91% of the aptamers remained on the HAS_H after washing process, while only *ca*. 43% of the aptamers were conjugated on the washed HAS_L. This quantitative consequence corresponded to the preceding SEM result.

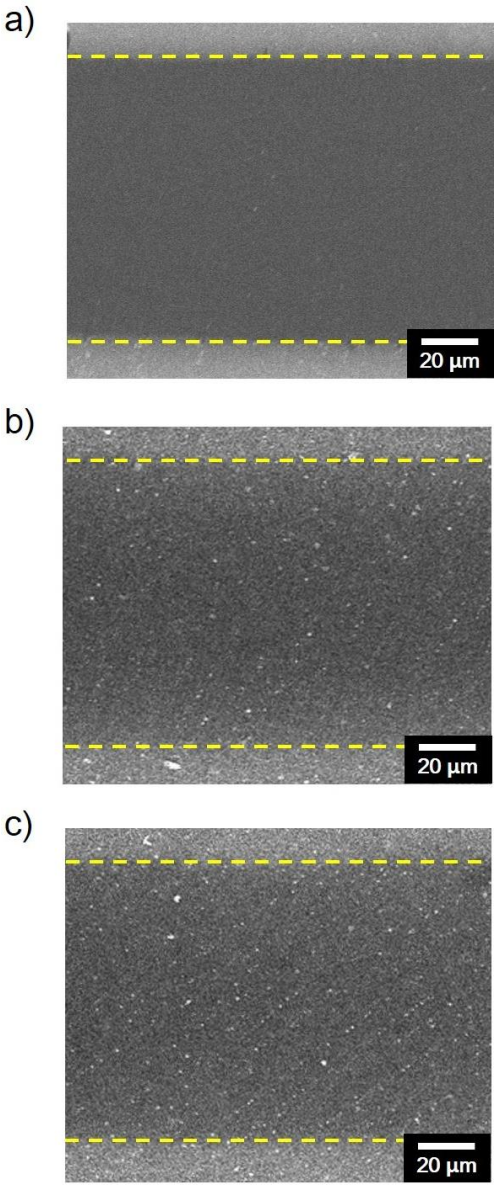

Figure 12. FE-SEM images of (a) pristine graphene, (b) HAS_L, and (c) HAS-H electrodes, respectively (HAS indicates hepatitis B aptasensor).

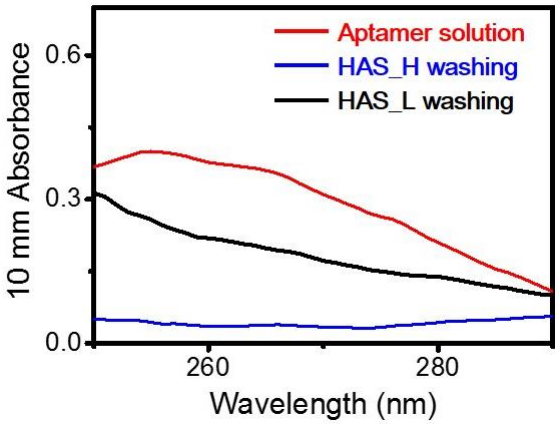

Figure 13. Spectrophotometric absorbance of conjugated aptamers on HAS_H and HAS_L surfaces before and after washing process.

3.1.4 Electrical properties of FET-type hepatitis B aptasensor

To assess the electrical characteristics of the flexible aptasensor, a current–voltage (*I*–*V*) measurement was accomplished. **Figure 14** shows the dependence of current *versus* voltage before and after the immobilization of the aptamer. Although d*I*/d*V* value slightly decreased following DAN, GA, and aptamer introductions, the *I*–*V* curves remained linear property. The result demonstrated that stable ohmic contact was preserved after introducing the aptamer. It can be concluded that the aptamer conjugation on the graphene surface provided reliable electrical contacts. In addition, the introduction of the aptamer was indirectly proven through changes in the *I*–*V* relationship. A liquid-ion gated FET configuration was constructed to utilize the aptasensor as an FET-type sensor. The FET geometry was surrounded with a phosphate-buffered solution (PBS; pH 7.4), which helped maintain effective gate regulation [150]. **Figure 15a** represents the experimental setup used to characterize the device performance of the aptasensor geometry under ambient conditions. **Figure 15b** presents the output characteristics of the aptasensor under different gate voltages (V_g) in a step of –1 V. The source-to-drain current (I_{sd}) negatively increased with negatively increasing gate V_g; this was due to the p-type (hole-transporting)

behavior. Moreover, the linear characteristics (ohmic contact) of the current curves were maintained under all gate V_g, indicating that electrostatic gating effect, rather contact resistance, can be the predominant effect leading to the electrical changes in the FET device. Considering these results, the aptamer/HBsAg interaction can induce a sensing signal in the liquid state.

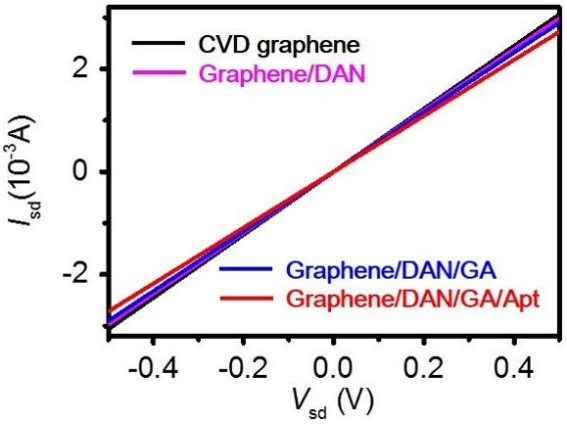

Figure 14. Current–voltage (*I*–*V*) curves of the hepatitis B aptasensor before and after the introductions of DAN, GA, and aptamers.

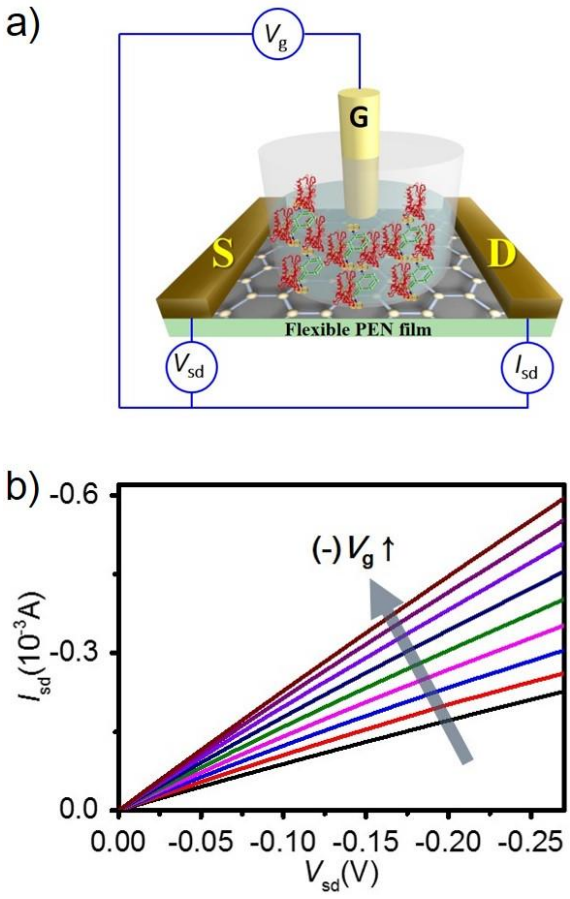

Figure 15. (a) Schematic illustration of a liquid-ion gated FET system ("G", "S", and "D" mean gating voltage and source/drain electrodes, respectively). (b) I_{sd}–V_{sd} output relationships of the graphene aptasensor at different V_g from 0 to –0.9 V in a step of –0.1 V (V_{sd}: 0 to –0.27 V in a step of –10 mV).

3.1.5 Real-time responses of FET aptasensor toward HBsAg

Graphene is widely known to be an ambipolar material having a Dirac point, which makes the use of graphene transducer be possible with either p-type or n-type regions [151]. Sensors based on graphene also exhibited ambipolar characteristics, but showed a more stable and sensitive response in the p-type region due to the adsorption of oxygen from air or water. Therefore, the real-time responses to the presence of HBsAg were measured at p-type region. The HBsAg as the target analyte interacts with the binding aptamer, and then changes electrostatic condition at the interface, which induces a change in the electrical signals. Observing the considerable changes allows real-time responses as well as the label-free detection in the FET device [152]. The sensing abilities were evaluated by measuring I_{sd} upon the introduction of various HBsAg concentrations. **Figure 16** reveals the real-time response of the aptasensor, as well as that of a pristine graphene for comparison. HAS_H samples, as the hepatitis aptasensor, were used for real-time responses in this study. The minimum detectable level (MDL) of HBsAg was *ca*. 10 fM, and the saturation level was *ca*. 1 nM. Moreover, the graphene-based aptasensor had rapid response times of less than 1 s, and the response was clearly meaningful (signal-to-noise: 6.62). The instantaneous signal

changes were monitored with wide ranging HBsAg concentrations (10 fM to 1 nM). The signal currents gradually increased when the aptasensor was exposed to higher concentrations of HBsAg, although the pristine graphene as a control experiment presented ignorable changes in I_{sd}. **Figure 17** reveals the plausible sensing mechanism. The increased I_{sd} mainly occurs through the interaction between HBsAg and the single stranded DNAs (ss DNAs) of aptamers. When the interaction takes place, the ssDNA conformation is transformed to a folded and compact structure [98]. Such folded conformation involves more exposed negative charge because of the negatively charged phosphate backbone of ssDNAs [153]. In addition, target HBsAg is negatively charged in pH 7.4 PBS solution [154]. From these results, holes as positive charge carriers are accumulated on the graphene transducer operated in a p-type region, resulting in the increased I_{sd}. This is comparable to a p-type doping effect affecting indirectly on the liquid-ion gate dielectric. The selective response toward HBsAg was also explored using the following other biomolecules: ascorbic acid (AA), uric acid (UA), bovine serum albumin (BSA), and immunoglobulin G (IgG). **Figure 18a** displays the structures of the other biomolecules. As shown in **Figure 18b**, no measurable change occurred in I_{sd} (signal-to-noise: <0.73) when the

aptasensor was treated with nontarget biomolecules (1 nM). However, significantly large changes in I_{sd} was observed upon the addition of target HBsAg (10 fM), which is clearly meaningful (signal-to-noise: 5.78). The ability to discriminate HBsAg with a high selectivity was accomplished using the binding aptamer with a sequence that is specific for HBsAg.

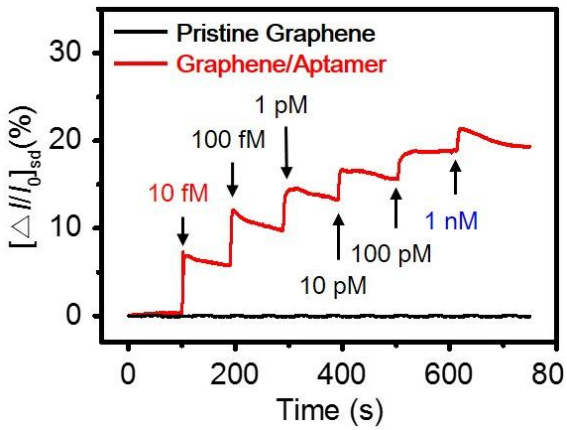

Figure 16. Real-time responses of the FET-type aptasensor with normalized current change ($\Delta I/I_0 = (I - I_0)/I_0$, where I is the real-time current and I_0 is the initial current).

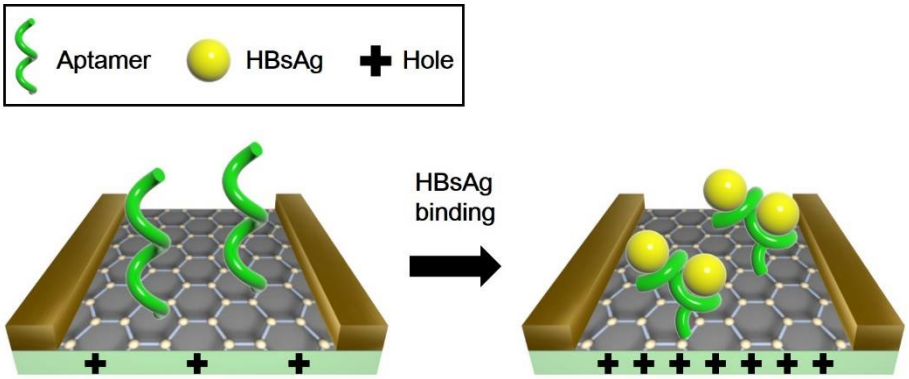

Figure 17. Schematic illustration of HBsAg detection mechanism based on the FET-type sensor.

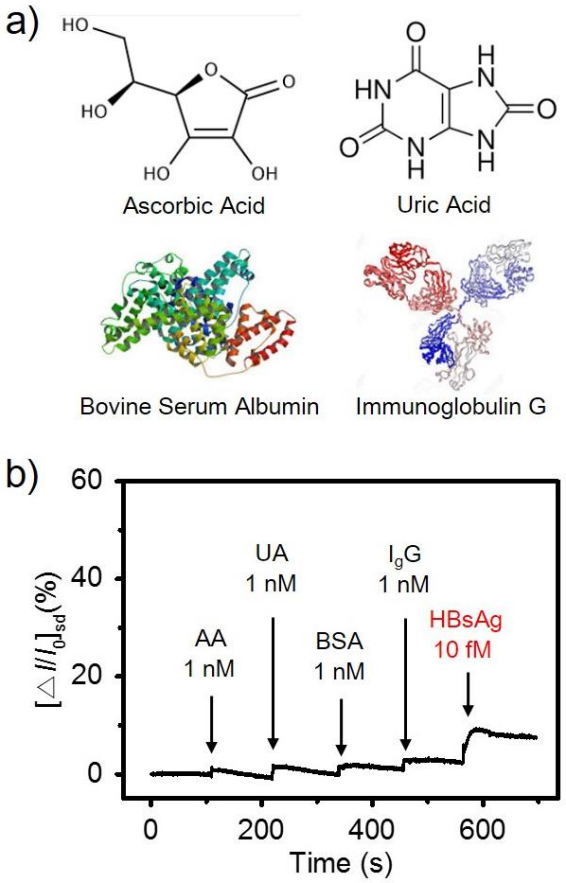

Figure 18. (a) Structures of diverse biomolecules as non-target analytes. (b) Selective response of the aptasensor toward target HBsAg (10 fM) and non-target analytes (1 nM).

3.1.6 Real-time responses of FET aptasensor toward real samples

Real-samples have been used to confirm the practical applicability of biosensors in many researches. Until recently, most hepatitis B sensors have been using plasma or serum derived from whole blood as real-samples [94,95,155,156]. However, the blood samples are collected by venipuncture and require well-trained personnel. In addition, the venipuncture is considerably painful for some people such as infants, children, hemophiliacs, or patients suffering from needle phobia. Therefore, a non-invasive method for HBsAg determination is needed to eliminate discomfort and pain. Saliva is a promising candidate as an alternative to venipuncture. Some researches demonstrated the potential use of saliva for HBsAg detection [157,158]. Compared with the blood samples, the collection of saliva samples is non-invasive, comfortable, and less expensive. From these attractive advantages, saliva can be a valuable real sample for HBsAg monitoring. **Figure 19a** delineates the real-time response of the aptasensor toward artificial saliva samples. No measurable changes occurred following the injection of pristine sample, whereas meaningful current changes were monitored upon the introduction of HBsAg (10 fM) spiked sample. To further evaluate sensing ability, real saliva samples were collected. Real saliva samples

were obtained from healthy volunteers after washing their mouths. The supernatants of the prepared samples were collected by centrifugation and used for response tests. As shown in **Figure 19b**, although no notable changes were observed upon the addition of pristine real sample, signal currents increased when the HBsAg spiked real samples were introduced. The current changes were observed a range of the HBsAg concentrations (10 fM to 10 pM). Judging from these results, the FET-type aptasensor is capable of detecting HBsAg in real saliva samples and can be utilized in practical applications. **Figure 20** presents the sensitive change (S) as a function of the HBsAg concentration. The HBsAg was dissolved in PBS or real saliva sample. The PBS-based sample was more sensitive than the saliva-based sample. Presumably, the various biomolecules in the real saliva could interfere with the binding event between the aptamer and HBsAg.

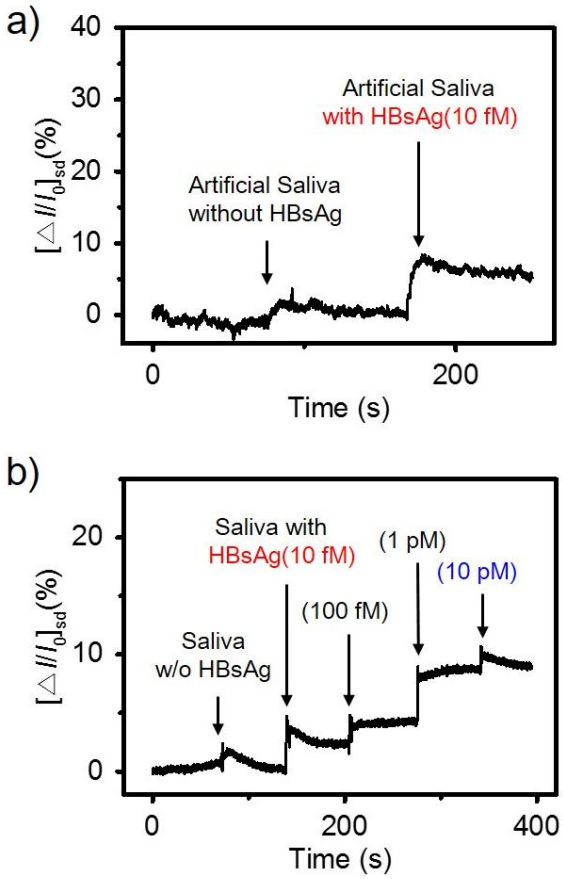

Figure 19. Real-time measurements of the aptasensors toward (a) artificial saliva and (b) real saliva samples.

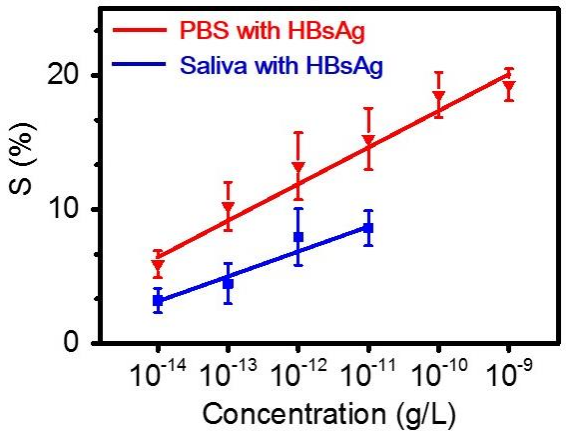

Figure 20. Sensitive changes toward various HBsAg concentrations (10 fM to 1 nM) (PBS (red line); real saliva (blue line)).

3.2 Fabrication of duplex bioelectronic tongue based on multiplexed graphene electrodes for sensing umami and sweet tastes

3.2.1 Fabrication of duplex bioelectronic tongue

Transducers play a crucial role in improving the performance of biosensors. Graphene is one of the high-performance materials for sensor transducers. It has a large surface area, high conductivity, and superb carrier mobility [159,160], providing outstanding sensing properties for biosensors [161,162]. To take the advantage of this special aspect, a FET-type taste sensor was fabricated with chemical vapor deposition (CVD)-grown graphene. **Figure 21** presents the schematic illustration for the duplex bioelectronic tongue (DBT) based on taste receptor nanovesicles. First, single layer graphene was fabricated by the CVD process. Subsequently, the graphene was positioned on a four-inch silicon oxide wafer using the wet-transfer method. Photolithography and reactive-ion etching (RIE) processes were used to prepare graphene micropatterns (GMs). Afterward, a second photolithography process was conducted to provide the photoresist patterns for contact electrodes that were utilized for the source (*S*) and drain (*D*) electrodes. The contact electrodes were deposited on the GM channels by the thermal evaporation of metals (Cr/Au) and liftoff method. Finally, dual-channel graphene based FETs

for DBTs were constructed after the passivation process. To introduce the nanovesicles on the GM channels, the surface of the GMs was exposed to pyrenebutyric acid *N*- hydroxysuccinimide ester (PSE) as the linker molecules. The PSE was placed on the GM channels *via* π–π stacking. The pyrenyl groups of the PSE were bound to the plane of the graphene [163]. Then, the PSE-functionalized GMs were treated with the nanovesicles containing umami or sweet taste receptors. The taste nanovesicles were provided by my co-worker whose name is Ahn, sae ryun [142]. **Figure 22** depicts the overall procedure for the preparation of nanovesicles containing heterodimeric human taste receptors. The succinimidyl groups of the PSE interacted with the proteins of the vesicles, resulting in chemically stable peptide bonding. Therefore, an immobilized nanovesicle sensor system was successfully fabricated on a silicon oxide substrate. Two GM channels of a DBT were used for the simultaneous detection of umami and sweet tastants. One channel was connected to umami vesicles, and the other channel was treated with sweet vesicles. As a result, the DBT sensor could simultaneously detect dual responses for umami and sweet tastants.

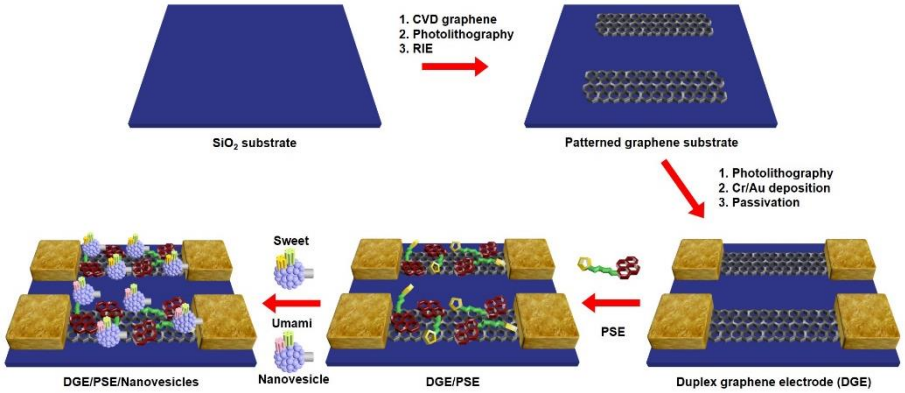

Figure 21. Schematic illustrations for the fabrication procedure of duplex sensor containing umami and sweet taste receptor nanovesicles.

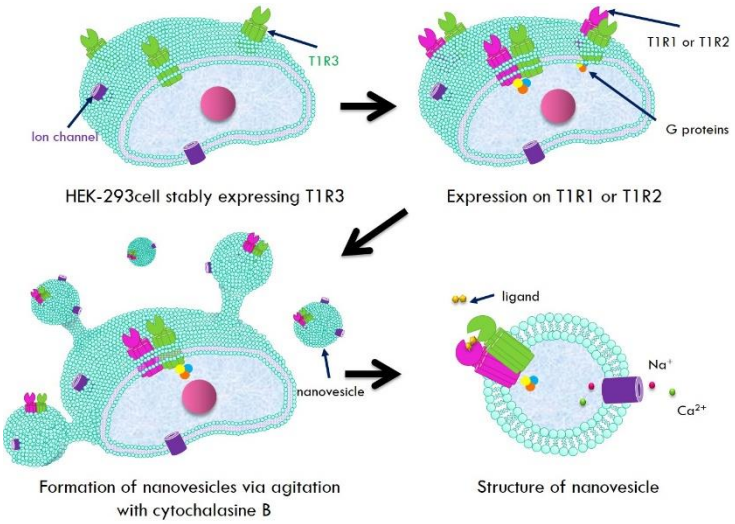

Figure 22. Illustrative diagram of the sequential steps for the preparation of nanovesicles expressing heterodimeric human taste receptors. Umami taste receptor (T1R1/T1R3) and sweet taste receptor (T1R2/T1R3) were stably expressed.

3.2.2 Characterization of duplex bioelectronic tongue

The expression of taste receptors on the as-prepared nanovesicles was evaluated using Western blot analysis (**Figure 23**). A fabricated multiplexed graphene electrode (MGE) circuit is represented in the photograph (**Figure 24a**). The MGE consists of eight pairs of source (S) and drain (D) electrodes, and two pairs of the contact electrodes were utilized for the DBT configuration. The CVD-grown graphene was used as the electrical channel between the contact electrodes. The number of layers and thickness of the graphene was measured by Raman spectra and high-resolution transmission electron microscopy (HR-TEM). Raman analysis was conducted to measure the distinctive peaks of the graphene. In a single layer graphene, the 2D peak has stronger and sharper intensity than the G peak, which distinguishes it from double and few layer graphene. As shown in **Figure 25a**, the G peak (～1590 cm^{-1}) and 2D peak (～2690 cm^{-1}) were consistent with single layer graphene. In order to further clarify the number of layers, the edge of the graphene was analyzed using HR-TEM, which is a powerful tool to visualize the graphene layer. The HR-TEM image displays the presence of single layer graphene (**Figure 25b**). **Figure 26** represents Fourier-transform infrared (FT-IR) spectra recorded before and after the introduction of PSE as

linker molecules. In case of PSE treated graphene, the three bands appeared at 1818, 1783, and 1738 cm^{-1}, corresponding to the C=O stretching vibration of the ester, the in-plane and out-of-plane of the succinimidyl group, respectively. In addition, the two peaks at 1207 cm^{-1} (C–N–C) and 1064 cm^{-1} (N–C–O) arise from the succinimidyl group [164]. The FT-IR result demonstrated that the PSE was successfully introduced to the graphene surface. Nanovesicles immobilized on a graphene channel were observed by field-emission scanning electron microscopy (FE-SEM), as shown in **Figure 27a and b**. The lyophilization process was performed to preserve the shape of the nanovesicles for the FE-SEM analysis. The SEM images clearly show that the nanovesicles were successfully attached to the surface of the graphene. As shown in the SEM image, the nanovesicles showed spherical shape with diameters in the range 100−200 nm.

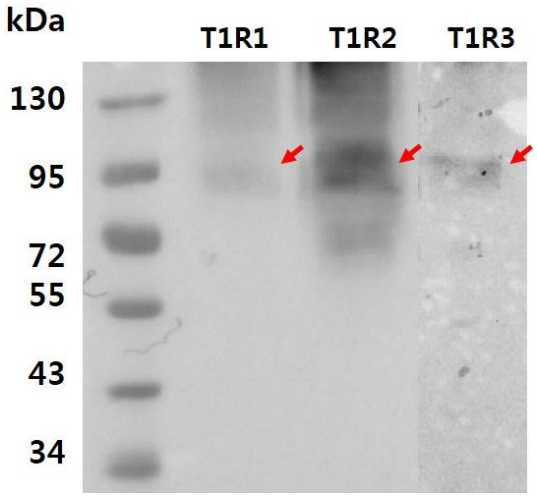

Figure 23. Western blot analysis for T1R1, T1R2, and T1R3 on the taste nanovesicles.

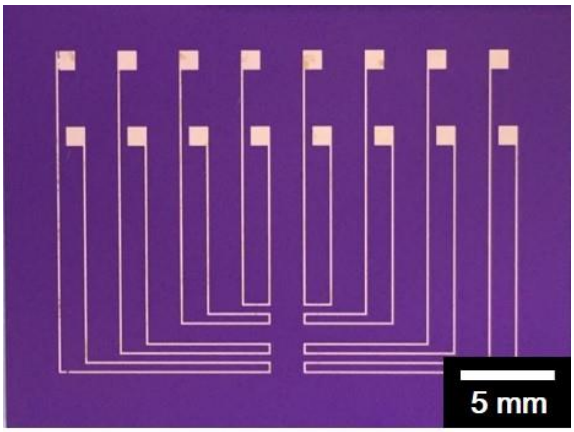

Figure 24. Photographic image of a fabricated multiplexed electrode on a silicon oxide wafer. Two pairs of the contact electrodes were simultaneously used to detect multiple responses.

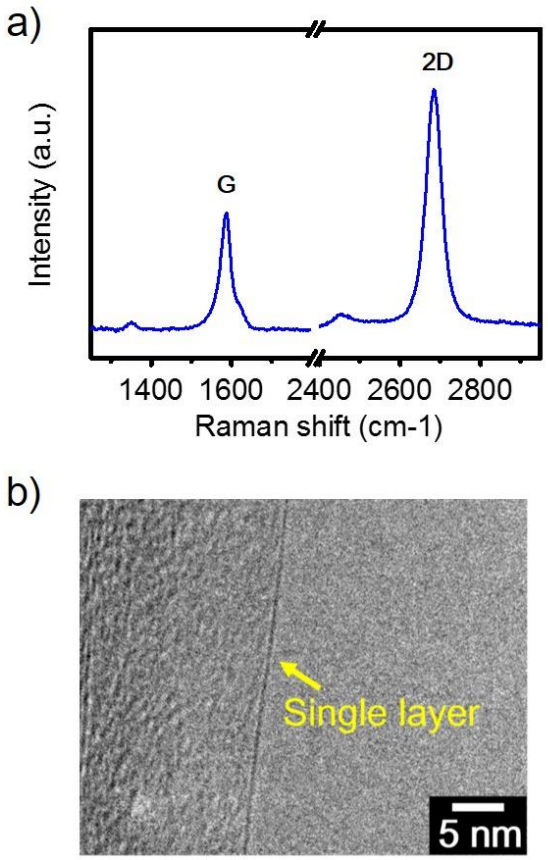

Figure 25. (a) Raman spectrum of CVD graphene on a silicon oxide substrate. (b) HR-TEM observation of CVD-grown single layer graphene.

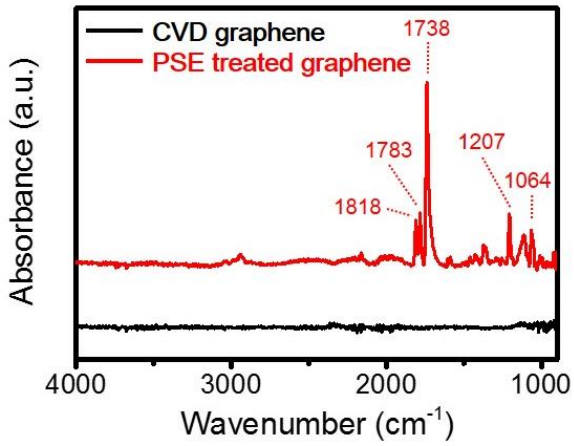

Figure 26. FT-IR spectra of graphene electrodes before (black line) and after (red line) the introduction of PSE.

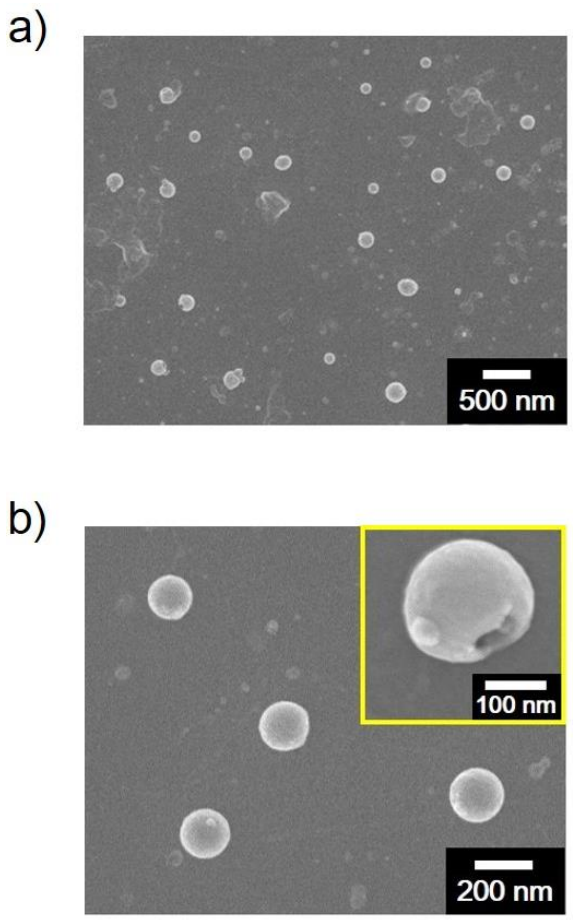

Figure 27. (a) Low- and (b) high-resolution FE-SEM images of graphene channels after the introduction of nanovesicles.

3.2.3 Electrical properties of duplex bioelectronic tongue

To exploit the electrical characteristics of the DBT configuration, current−voltage ($I-V$) measurement was carried out (**Figure 28a**). The graph in Figure 4c exhibits the variations in the $I-V$ values before and after nanovesicle immobilization on the surface of the GM channel. The $I-V$ relation maintained linear properties, even though the dI/dV value moderately decreased after nanovesicle attachment. It was apparent that stable ohmic contact remained during the immobilization process. These results demonstrate that the DBT transducers can preserve a reliable electrical contact, indicating that an interaction between target tastant and nanovesicles can be detected by observing the changes in the current. Exploring the possibility to utilize nanovesicle-immobilized GM channels as transducers in the FET system, a liquid-ion gated FET geometry was fabricated. The FET system was used to investigate the electrical characteristics under different gate voltages (V_g). Dulbecco's phosphate buffered saline (DPBS; pH 7.4) was used as the electrolyte. A gate electrode was placed in the DPBS electrolyte, providing that the transducer has a reliable contact with the solution. **Figure 28b** reveals the output curves of the DBT under various V_g ranging from 0 to −3 V. The source-to-drain current (I_{sd}) negatively increased according to

negatively increasing V_g, meaning p-type semiconductor behavior (hole-transporting). Moreover, the ohmic contact remained at the different V_g, suggesting that the sensing signal changes were mainly affected by the electrostatic gating effect of the GM channel, rather than the contact resistance. Considering these results, the DBT can transduce the sensing signal created when charge-carrier density is changed by the interaction between the nanovesicles and specific-target molecules. Thus, the liquid-ion gated FET system facilitates a label-free detection of taste molecules.

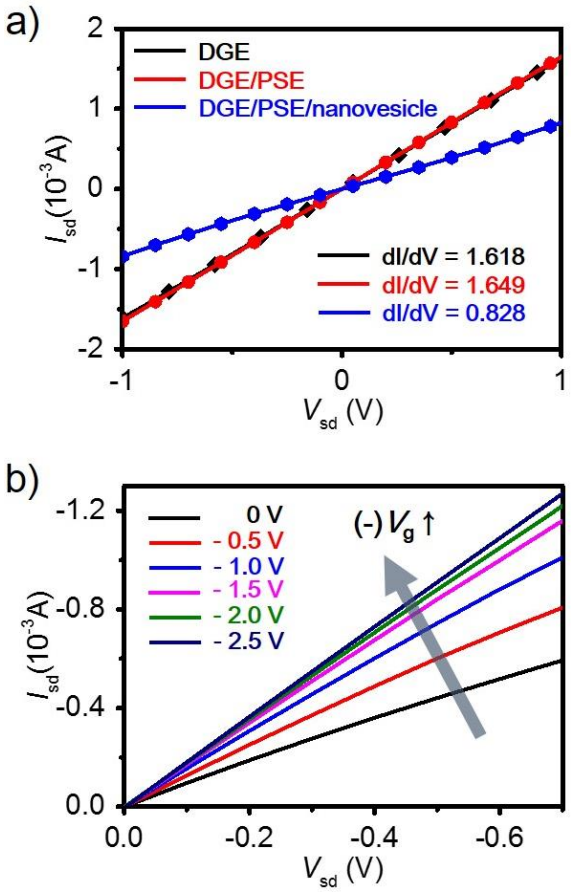

Figure 28. (a) Current−voltage ($I-V$) curves of the DBT sensor before and after the immobilization of nanovesicles. (b) Output characteristics of a FET-type DBT (V_g, 0 to −2.5 V in a step of −0.5 V, and V_{sd}, 0 to −0.7 V in a step of −50 mV).

3.2.4 Real-time responses of the DBT for umami tastant

In my previous investigation, graphene-based FET sensors demonstrated stable and responsive performance in the p-type region because of the adsorption of oxygen, whereas the graphene-based sensors had ambipolar properties. Therefore, real-time responses in this study were measured in the p-type region. **Figure 29** illustrates the sensing mechanism of the graphene-FET type DBT platform. First, the specific binding between the taste receptor and target tastant-induced signal transduction inside the nanovesicles *via* G-proteins and ion channels introduced Ca^{2+} ions into the nanovesicles. Subsequently, the accumulated ions applied a positive gate effect on the surface of the p-type sensors. Finally, the positive potential effect reduced the number of holes in the graphene and thus decreased the I_{sd}. As shown in **Figure 30**, the real-time responses of the DBT device were observed by monitoring the I_{sd}, after adding various monosodium glutamate (MSG) concentrations. The I_{sd} value immediately decreased upon exposure to MSG as umami tastant, coinciding with the sensing mechanism of the DBT device. The minimum detectable level (MDL) was ～100 nM (signal-to-noise ratio 3.10), and the saturation level was ～1 mM. The detection limit (100 nM) of the DBT was 1000-times more sensitive than

those of other taste sensors using polymer membranes and lipid membranes [165,166]. The current changes were detected over a wide range of MSG concentrations (10^{-7} to 10^{-3} M), and the current signals gradually decreased in response to higher concentrations of MSG. However, the pristine duplex graphene electrode (DGE) in the absence of the nanovesicle did not show any critical changes in the I_{sd} after the introduction of MSG, indicating that the specific interaction between the nanovesicles and umami tastant triggered prompt current changes. Moreover, the DBT exhibited a highly rapid response (on a time scale of less than 1 s). **Figure 31a** displays the chemical structures of MSG, L-glutamine (non-umami taste), and umami enhancers. The chemicals were used to prove the specificity of the DBT device, as shown in **Figure 31b**. Although the nontarget chemicals had much higher concentrations (3 orders of magnitude) than target MSG, no significant changes occurred following the injection of the nontarget chemicals. However, the addition of 100 nM concentration of MSG remarkably affected the current changes in I_{sd}, indicating that the DBT features the ability to perceive the target tastant with superior selectivity.

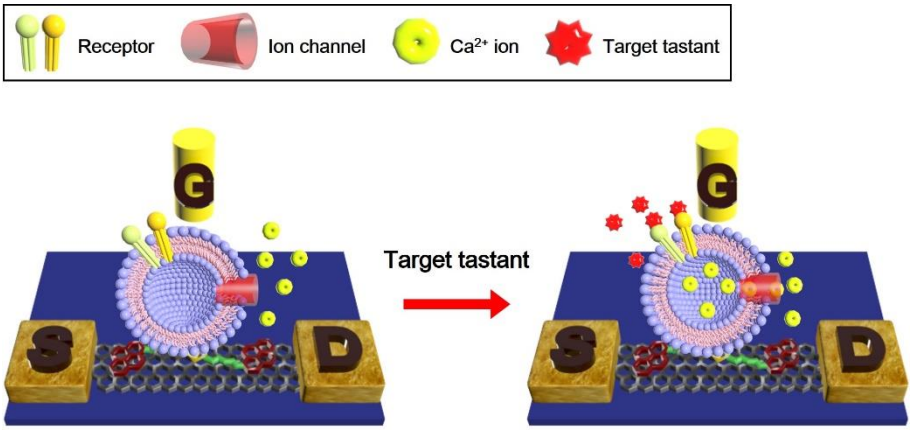

Figure 29. Schematic diagram depicting the FET geometry and showing the sensing mechanism of a DBT.

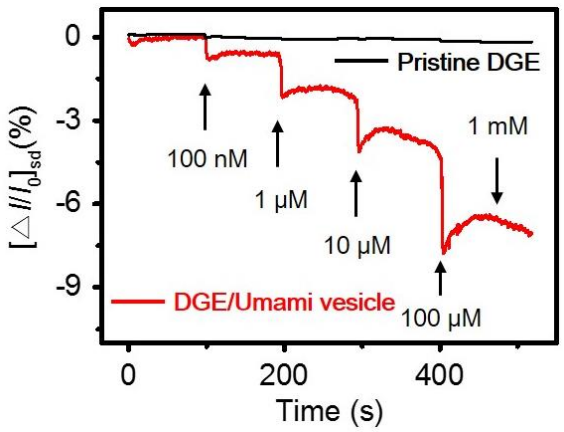

Figure 30. Discrimination of umami tastants with umami taste nanovesicle-immobilized bioelectronic tongues. Real-time response of a single channel in a DBT with various concentrations of MSG (100 nM to 1 mM). DGE stands for duplex graphene electrode.

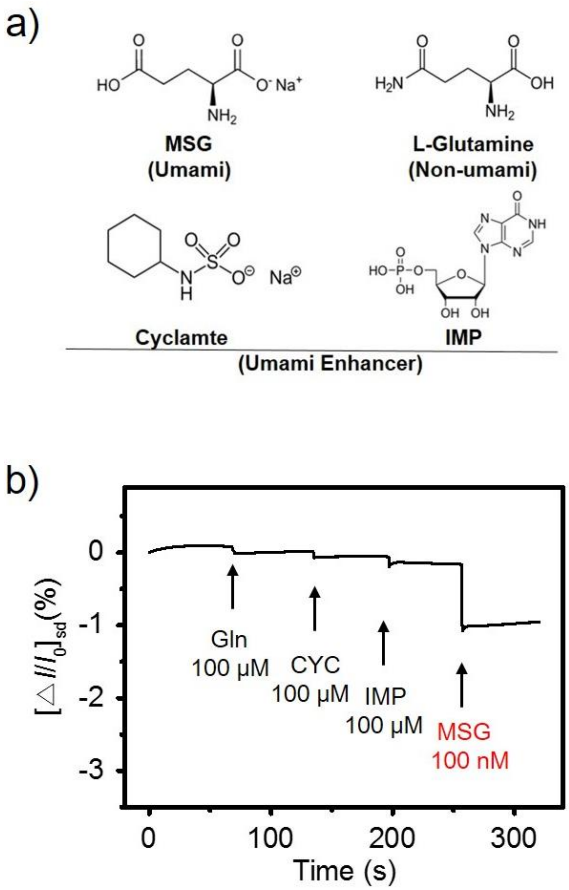

Figure 31. (a) Chemical structures for sensing tests related to umami taste. (b) Selective response of a DBT toward target tastant (MSG, 100 nM).

3.2.5 Real-time responses of the DBT for umami tastant in artificial seasonings

L-Glutamic acid is one of wellknown umami tastants and occurs naturally in diverse foods containing kelp, mushrooms, fish, dairy, and meat. However, it is hard to feel the umami taste in those foods due to the low solubility of the glutamic acid [167-169]. MSG is highly soluble glutamic acid. Therefore, artificial seasonings consisting of MSG are commonly used in food for the umami taste [170]. **Figure 32** shows the normalized sensitivity ($\Delta I/\Delta I_{max}$) of the DBT platform to commercially available artificial seasonings. The artificial seasoning 1 was comprised of salt, sugars (sucrose, lactose), flavor raw material (dried bonito powder, bonito extract), yeast extract, wheat protein-fermented seasoning, and yeast extract-fermented seasoning. The artificial seasoning 2 consisted of 97.3% MSG, 1.35% IMP, and 1.35% guanosine monophosphate (GMP). The normalized sensitivity steadily increased over a range of the seasoning concentrations (10^{-8}–10^{-4} g/L). The concentration of artificial seasonings normally dissolved in food is in the range 1−10 g/L. Compared with the concentration range, it can be concluded that the sensitivity of DBT is sufficient to be utilized in the food analysis.

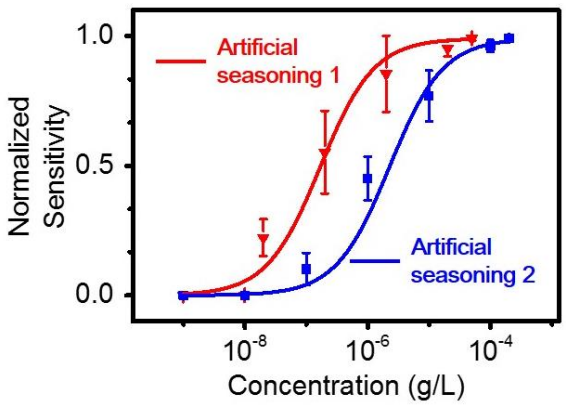

Figure 32. Dose-dependent responses of DBTs to artificial seasonings containing target umami tastant.

3.2.6 Real-time responses of the DBT for sweet tastant

Figure 33a displays the real-time responses of the sweet taste sensor. The I_{sd} of the sensor decreased because of the interaction between the sweet taste receptor nanovesicles and sucrose and was entirely consistent with the sensing mechanism of the previous umami sensor. The current changes were observed within 1 s and detected over an extensive range of sucrose concentrations (1 μM to 10 mM), whereas a sensor without nanovesicle as a control experiment exhibited only slight variation. The DBT of the sucrose sensor was ~1 μM (signal-to-noise ratio 5.41), and the saturating concentration was ~10 mM. The limit of detection (LOD) in the DBT was 1 μM and was 100-times more sensitive than that of previously reported sensor based on a swCNT-FET [28]. The outstanding properties of CVD graphene contributed to this enhanced performance. The 2D graphene channel had a larger area than 1D CNT channels, enabling more nanovesicles to be loaded in the channel of the graphene-FET sensor. Moreover, the graphene featured high conductivity and fast carrier mobility, leading to improved signal transduction. The calibration curves of the DBT was demonstrated using various concentrations of the sweet tastants, as shown in **Figure 33b**. Increased sensitivity appeared when the DBT was treated with higher concentrations of natural (sucrose

and fructose) and artificial (saccharin and aspartame) sweet tastants. However, no significant sensitivity changes were observed in the case of tasteless sweet tastants (Dglucuronic acid and cellobiose). Importantly, the DBT had a more sensitive reaction with the artificial tastants than the natural tastants, which is consistent with general human sensory responses [171]. This result suggested that the artificial tastants elicited stronger stimulation than the natural tastants, and the DBT could mimic the human taste system related to sweeteners. **Figure 34a** presents the chemical structures of natural sugars (sucrose and fructose), tasteless sugars, and artificial sweeteners for the sensing experiments. The selective response of the DBT to sucrose is shown in **Figure 34b**. The I_{sd} values changed significantly when sucrose (1 μM) as the target sugar was introduced in the DBT configuration, whereas the addition of D-glucuronic acid and cellobiose (1 mM) as tasteless sugars did not affect signal. Based on these results, the sweet sensors could differentiate a target sugar with excellent selectivity from the tasteless sugars.

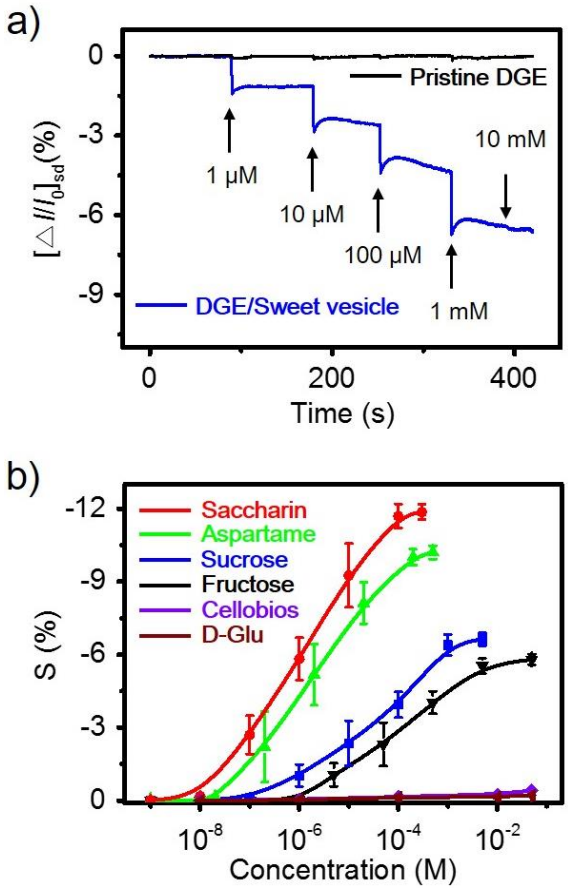

Figure 33. Sensing performance of sweet taste receptor nanovesicle-based bioelectronics tongues. (a) Real-time electrical measurement of a DBT to various sucrose concentrations (1 μM to 10 mM). (b) Calibration curves of DBTs toward tasteless, natural, and artificial sweet tastants.

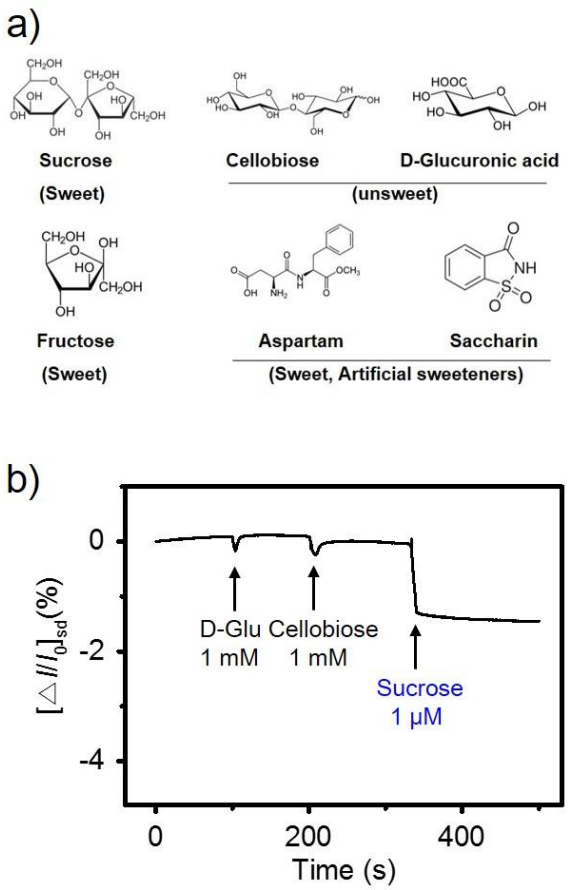

Figure 34. (a) Chemical structures of diverse sweet tastants. (b) Selective property of a DBT toward target tastant (sucrose, 1 μM) and nontarget tastants (cellobiose and D-glucuronic acid, 1 mM).

3.2.7 Dual responses of the DBT for umami and sweet tastants

The DBT platform delineated highly sensitive and selective responses for each umami and sweet tastant. Based on the outstanding performance, the duplex sensor was used to simultaneously detect umami and sweet tastants. **Figure 35a** shows a schematic diagram of a liquid-ion gated duplex sensor. One channel was utilized as umami channel treated with umami taste receptor nanovesicles, and the other channel operated with sweet taste receptor nanovesicles. **Figure 35b** shows the dual responses in the DBT sensor upon the stimulation of tastants. The umami channel was stimulated only by the injection of MSG, whereas the sweet channel was selectively activated by the addition of sucrose. According to the selective interaction of each channel, the DBT system successfully discriminated specific tastants. The DBT demonstrates human-like dual responses to umami and sweet tastants and has potential for applications such as bioelectronic tongues, which can mimic human sensation. To validate the possibility of the DBT sensor for practical applications, responses for drink samples were observed using the duplex device. Commercial tomato juice and green tea were used for the drink samples. **Figure 36a** displays the result of dual responses for the tomato sample. Tomato is widely known to contain

much L-glutamate [172]. The current changes were observed in both the umami and sweet channels when the tomato juice solution was introduced. Subsequently, the electrical signal was further changed in the sweet channel when the tomato juice additionally containing sucrose was added to the sensor. However, no measureable change was detected in the umami channel. The response speed of the duplex sensor was slow in the case of the tomato sample. Presumably, the interaction between the nanovesicles and tastants could be interrupted by various types of non-target molecules in the real drink sample. To further evaluate the sensing performance of a food sample, a green tea sample was used on the duplex system, as shown in **Figure 36b**. The selective responses from two channels occurred upon the exposure to the green tea sample. Green tea is known to have umami taste because it contains high level of amino acids including L-glutamate [173,174]. The addition of the green tea solution resulted in the current changes at only the umami channel. In contrast, the introduction of the solution containing sucrose altered the current signals of only the sweet channel. These results indicate that the DBT sensor has the ability to discriminate target tastants in real food samples and can be utilized in practical applications.

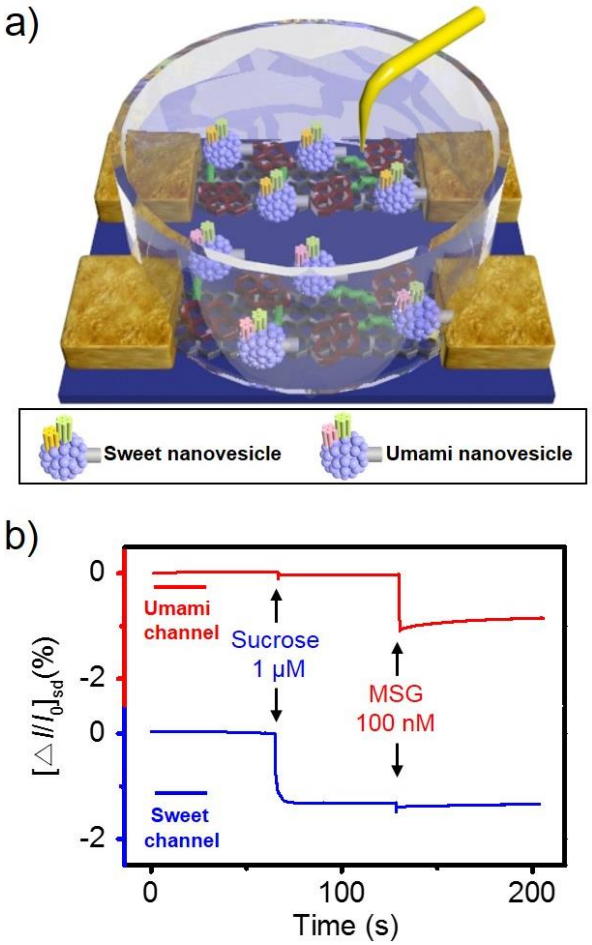

Figure 35. Simultaneous detection of umami and sweet tastants using DBTs. (a) Schematic diagram of DBT geometry. (b) Real-time responses of two channels in the DBT sensor toward umami and sweet tastants.

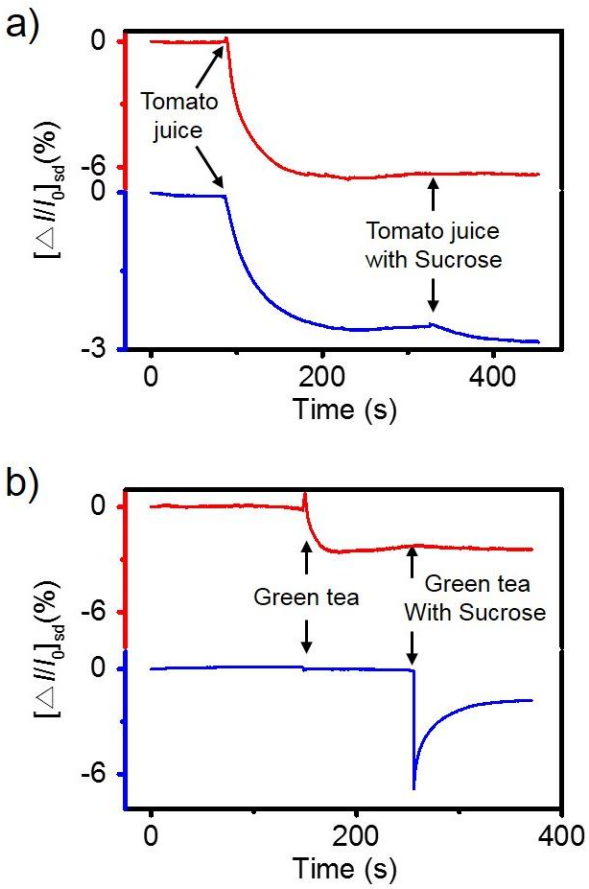

Figure 36. Real-time responses from (a) tomato juice solution and (b) green tea solution as real drink samples (red and blue lines indicate umami and sweet channels, respectively).

3.3 Fabrication of highly sensitive FET-type aptasensor using flower-like MoS_2 nanospheres for real-time detection of arsenic(III)

3.3.1 Fabrication of carboxylated polypyrrole-coated FMNSs

The conducting polymer-coated MoS_2 nanospheres were fabricated using hydrothermal, annealing and vapor deposition polymerization (VDP) processes. **Figure 37** represents the schematic illustration for overall procedure. First, self-assembled nanospheres (NSs) were prepared by a simple hydrothermal method. Ammonium tetrathiomolybdate and hydrazine monohydrate were used as precursors for the hydrothermal method. XRD measurement showed the absence of the (002) diffraction peak, which indicated that the NSs had poor crystallinity along the c-axis (**Figure 38a**). Annealing at 600°C for 1 h formed highly ordered 3D flower-like MoS_2 nanospheres (FMNSs) along the (002) direction (**Figure 38c**). The flower-like nanostructure provided a high surface area with numerous potential reaction sites. In addition, the (100) and (110) peaks were stronger and sharper after the annealing process, meaning enhanced crystallinity. Interestingly, the morphology of FMNSs was controlled by the quantity of the hydrazine monohydrate, which varied from 0.75 to 3.75 mL. **Figure 39a-c** present transmission electron microscopy (TEM) images of the FMNSs with

increasing hydrazine solution. The optimum morphology of the FMNSs was obtained when 1.875 mL of hydrazine was used for the hydrothermal process (**Figure 39b**). **Figure 40** shows the N_2 adsorption/desorption isotherms conducted using the Brunauer–Emmett–Teller (BET) analysis for the morphology-controlled FMNSs. The surface area of FMNS_1.875 was the highest value, which corresponded to the aforementioned TEM result. Therefore, the FMNSs_1.875 sample was used in all remaining study. Subsequently, the as-prepared FMNSs were exposed to $FeCl_3$ solution to introduce ferric cations (Fe^{3+}) as an initiator for the VDP process. The Fe^{3+} ions were immobilized on the surface of the FMNSs through charge–charge interactions between Fe^{3+} ions and the negatively charged NSs. The surface charge of the FMNSs was confirmed by electrophoretic light scattering spectrophotometry (**Table 1**). To induce polymerization *via* chemical oxidation, carboxylated pyrrole monomers were vaporized in a vacuum oven. Polymerization of the monomers proceeded on the FMNS surface, with the adsorbed Fe^{3+} ions as an oxidant, to form the CFMNSs.

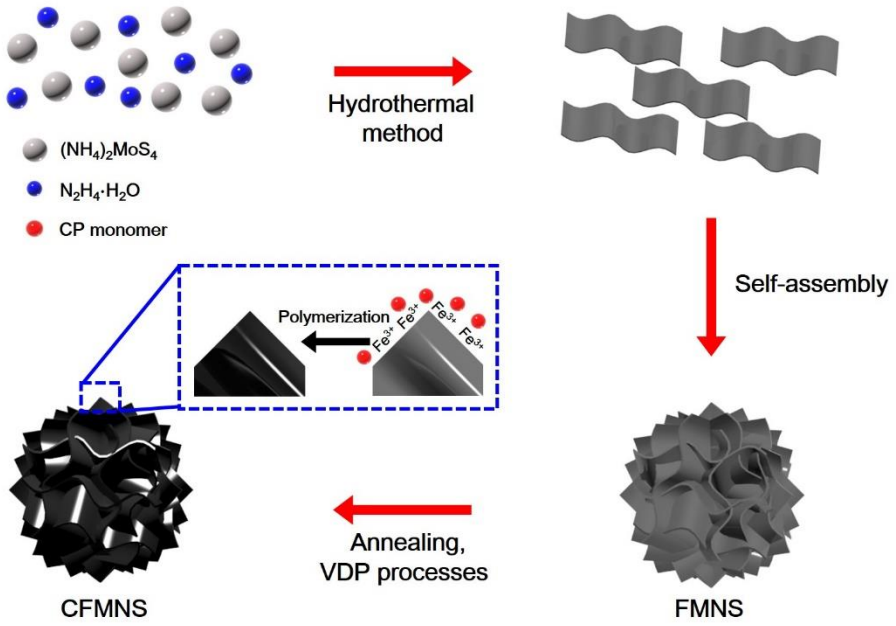

Figure 37. Schematic diagram of the fabrication steps for flower-like MoS_2 nanospheres coated with carboxylated polypyrrole.

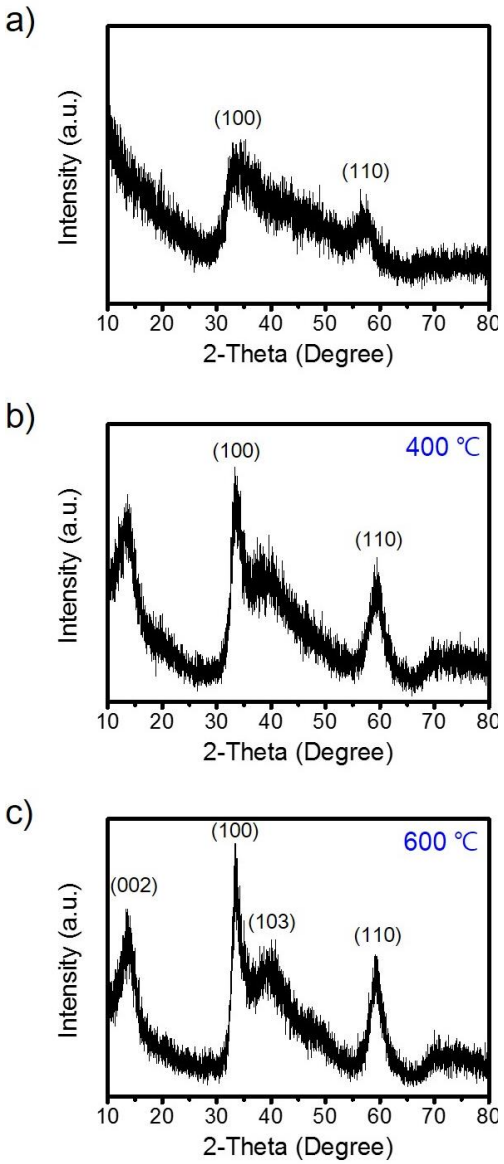

Figure 38. XPS patterns of FMNSs (a) before annealing, (b) after annealing at 400 °C, and (c) after annealing at 600 °C.

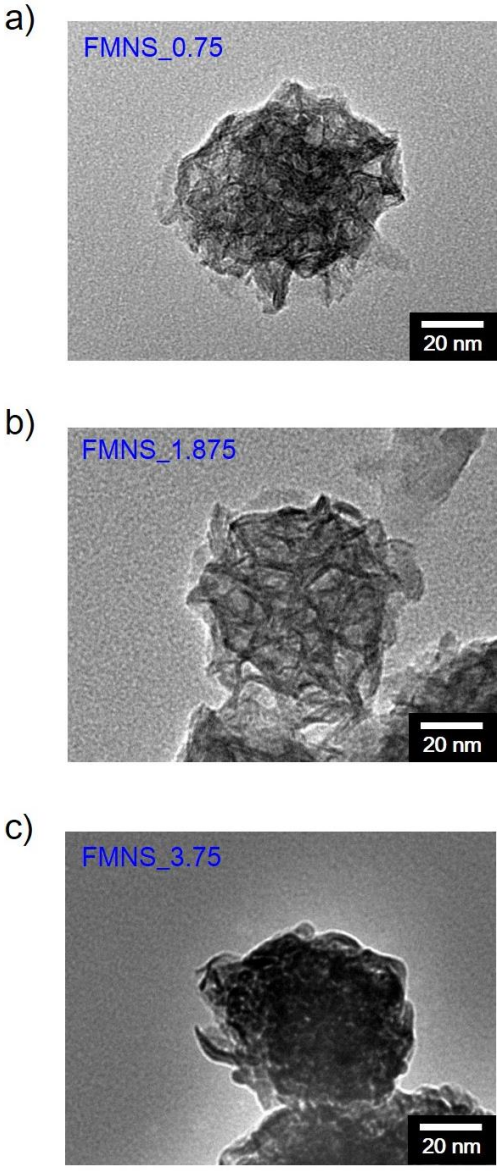

Figure 39. TEM images of FMNSs with various hydrazine monohydrate quantity; (a) 0.75 mL, (b) 1.875 mL, and (c) 3.75 mL, respectively.

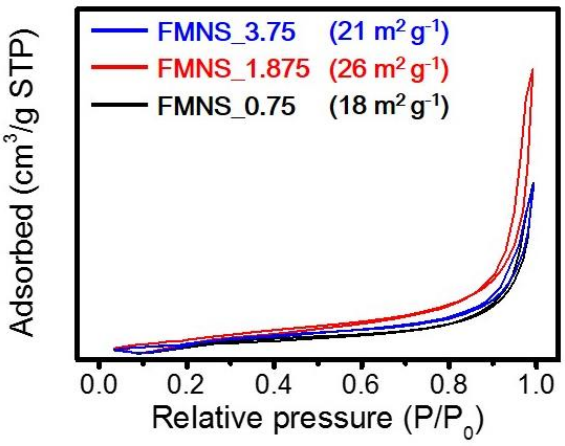

Figure 40. Nitrogen adsorption−desorption isotherms of FMNS_0.75 (black line), FMNS_1.875 (red line), and FMNS_3.75 (blue line), respectively.

Table 1. Zeta potential measurements for FMNS samples.

FMNSs	Zeta Potential (mV)[a)]
Sample 1	–73.46
Sample 2	–79.54
Sample 3	–84.60

a) Values were obtained by electrophoretic light scattering spectrophotometer.

3.3.2 Characterization of FMNSs

The as-prepared FMNSs were examined by field-emission scanning electron microscopy (FE-SEM) (**Figure 41a**). The FMNSs present spherical shape with diameters ranging from *ca*. 70 to 120 nm. Transmission electron microscopy (TEM) clearly reveals the 3D flower-like nanostructure of the FMNSs (**Figure 41b**). **Figure 42** displays high-resolution TEM (HR-TEM) image of the FMNS, which presents the d-spacing between adjacent MoS_2 single layers. This spacing is *ca*. 0.64 nm, which correspond to the (002) interlayer spacing of MoS_2 [175]. Selected area electron diffraction (SAED) was used to further analyze the structure of the FMNSs. The SAED pattern (**inset of Figure 42**) represents the (100), (103), (110) and (002) planes, indicating that the FMNSs have a hexagonal structure [176]. The crystallinity and structure of the FMNSs were determined by XRD analysis. As shown in **Figure 43a**, the diffraction peaks corresponding to the (002), (100), (103) and (110) planes were in good agreement with those of the hexagonal MoS_2 reference (JCPDS card No. 37-1492) [176]. This demonstrated that the obtained FMNSs were highly pure and had the hexagonal structure. Interestingly, the (002) plane peak of the FMNSs was much less intense than that of bulk MoS_2 (**Figure 43b**). This reduced intensity suggested

that the stacking interaction between the MoS_2 single layers had been prevented, resulting in the formation of few-layer MoS_2 [177]. In order to study the chemical composition of Mo and S in the as-prepared FMNSs, X-ray photoelectron spectroscopy (XPS) analysis was investigated (**Figure 44a and b**). The Mo 3d feature displayed two peaks at 229.6 and 232.8 eV, which are associated with Mo $3d_{5/2}$ and Mo $3d_{3/2}$, respectively (**Figure 44a**). In addition, two characteristic S peaks located at 162.5 and 163.6 eV were assigned to S $2p_{3/2}$ and S $2p_{1/2}$, respectively (**Figure 44b**) [175].

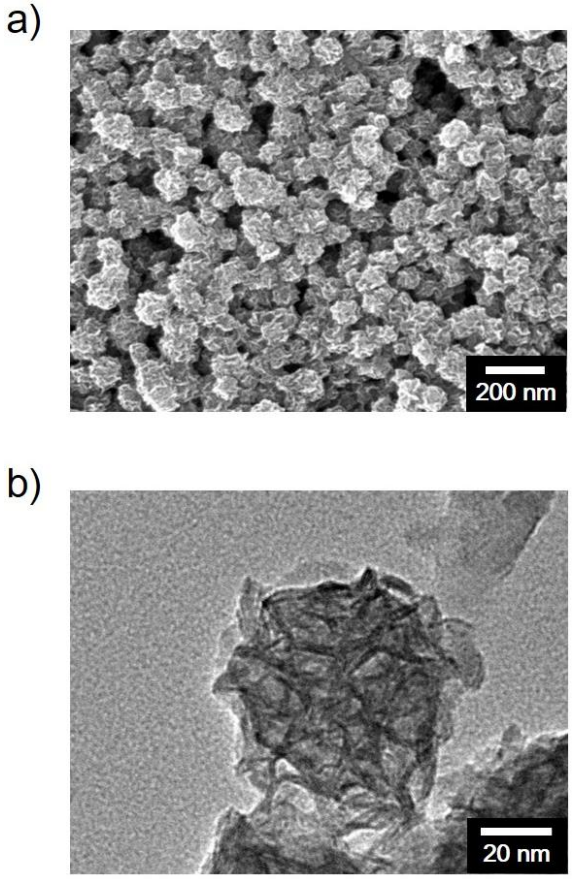

Figure 41. (a) FE-SEM micrograph of FMNSs. (b) TEM image of FMNS.

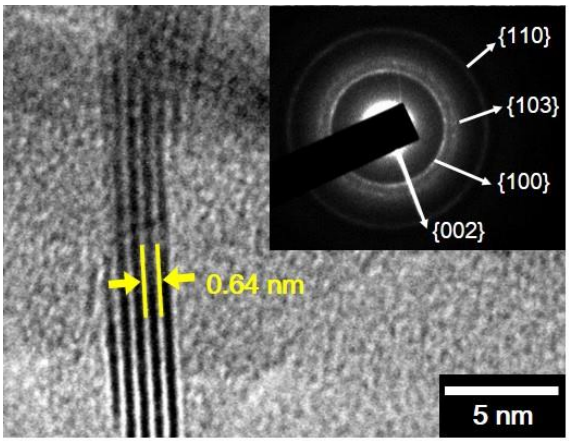

Figure 42. HR-TEM image and SAED diffraction pattern (inset) of FMNS.

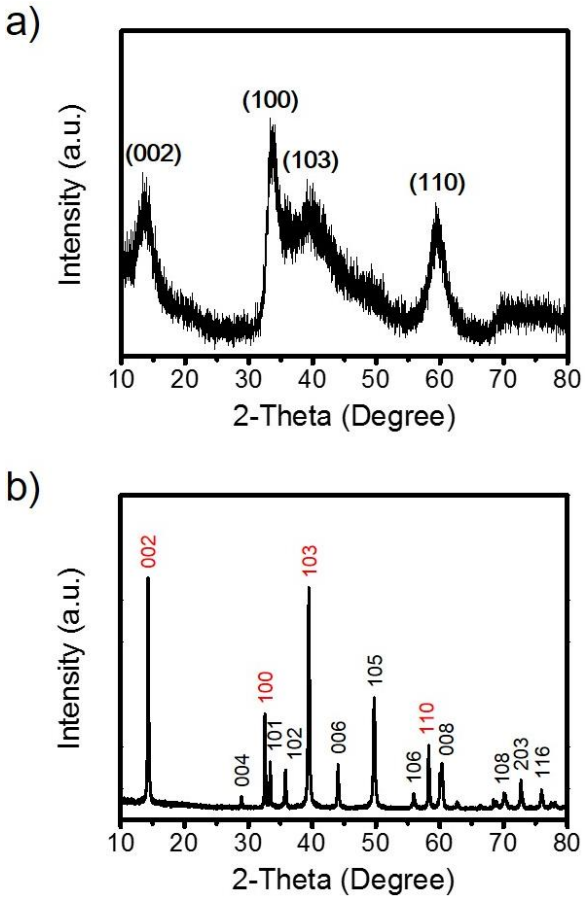

Figure 43. XRD patterns of (a) flower-like MoS_2 nanospheres and (b) bulk-MoS_2.

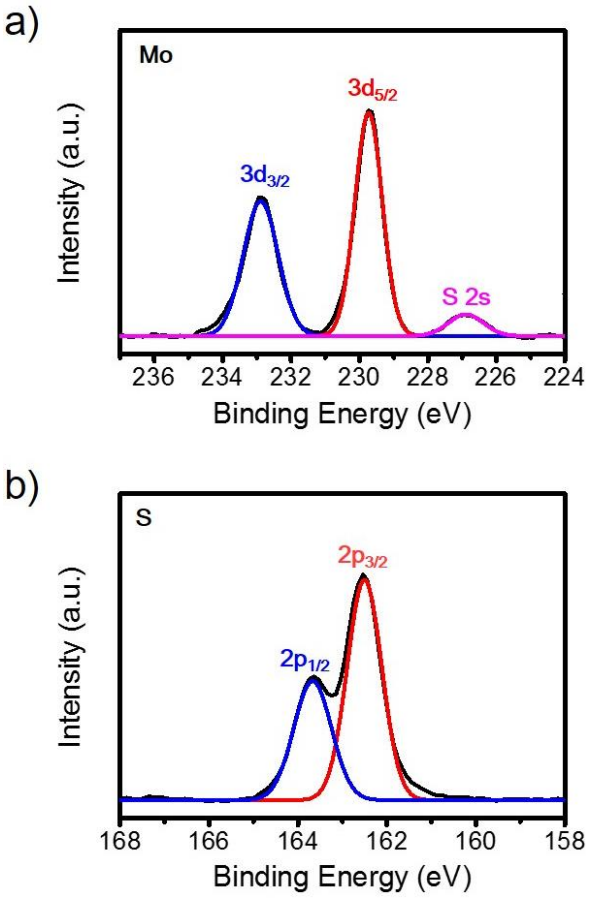

Figure 44. High-resolution XPS spectra of (a) the Mo 3d region and (b) the S 2p region of FMNSs.

3.3.3 Characterization of CFMNSs

CPs can be effective signal transducers due to their high conductivity. The π-conjugated electronic system of CPs can lead to excellent conductivity [178]. The polymer backbone provides an outstanding pathway for the flow of electric charge during electrochemical reactions. Moreover, the functional groups of CPs play important roles in achieving surface modification [179]. To utilize these attractive characteristics, CPPy, a high-performance CP, was introduced onto the as-prepared FMNSs. A CPPy layer was successfully coated on the surface of the FMNS *via* the VDP process. **Figure 45** shows an HR-TEM image of CPPy-coated FMNSs (CFMNSs), revealing a *ca*. 2-nm-thick coating layer on the surface. Additionally, there was no aggregation of CPPy despite the chemical oxidant polymerization, suggesting that the ferric cations were uniformly distributed on FMNS surfaces. **Figure 46** exhibits Fourier-transform infrared (FT-IR) spectra recorded before and after the introduction of the CPPy coating layer. The pristine FMNSs did not show distinctive peaks related to the pyrrole ring structure and carbonyl functional group due to the absence of the CPPy. In contrast to the spectrum of the FMNSs, absorption bands appeared at 1,551 and 1,471 cm^{-1} in the FT-IR spectrum of the CFMNSs, corresponding to the

C–C stretching and C–N stretching vibrations of the pyrrole ring, respectively. Furthermore, peaks at 1,294 and 1,187 cm^{-1} were assigned to the =C–H in-plane vibration. The absorption band at 907 cm^{-1} corresponded to the =C–H out-of-plane vibration. Moreover, the appearance of a peak at 1,702 cm^{-1} (corresponding to the C=O stretching vibration of the carboxylic acid) indicated the presence of the carbonyl functional group [85,180]. To further clarify the presence of the CPPy layer, the chemical composition of the FMNSs and CFMNSs was confirmed by XPS analysis. **Figure 47a** represents the survey scan spectrum, which indicated the presence of Mo, S, C and O in both samples. Although the N 1s peak was present in the CFMNSs spectrum, there was no corresponding peak in the FMNSs spectrum. The appearance of the N 1s peak was attributed to the nitrogen atoms of the CPPy, and implied that the CPPy coating on the FMNS surfaces was successfully applied. **Figure 47b** displays the deconvoluted XPS N 1s spectrum of the CFMNs. The three deconvoluted XPS peaks originated from the N atoms of the pyrrole ring. The three peaks at 397.2, 399.5, and 401.2 eV correspond to imine-like nitrogen, neutral nitrogen, and positively charged pyrrolium nitrogen, respectively [181].

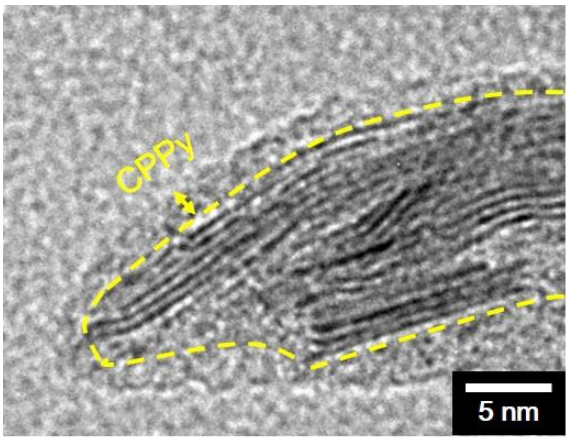

Figure 45. HR-TEM image of carboxylated polypyrrole-coated FMNS.

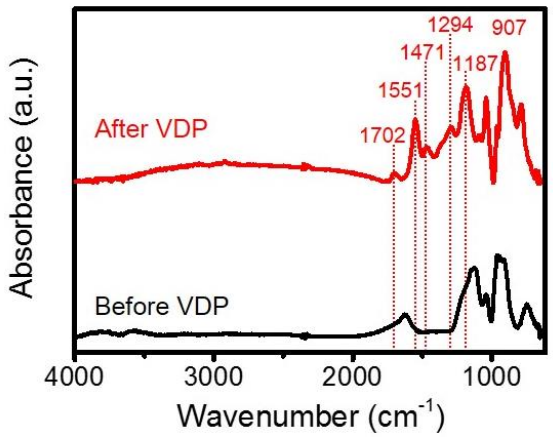

Figure 46. FT-IR spectra of FMNSs (black line) and CFMNSs (red line).

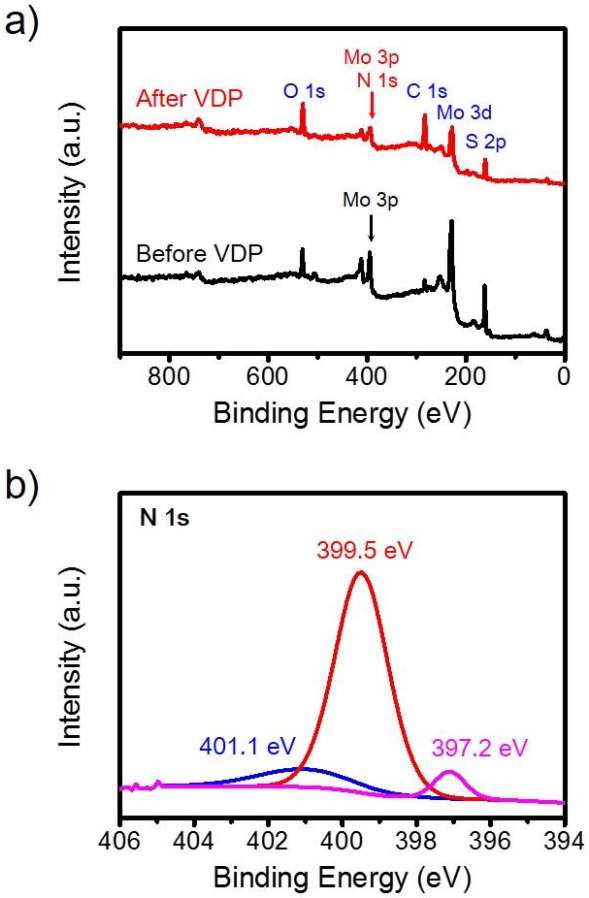

Figure 47. (a) XPS spectra of FMNSs (black line) and CFMNSs (red line). (b) Deconvoluated XPS N 1 s spectrum of CFMNSs.

3.3.4 Immobilization of aptamers on CFMNS surfaces

Figure 48 illustrates the synthetic procedures used to prepare the aptamer-immobilized CFMNSs on the electrode substrate. First, an interdigitated array (IDA) that contained pairs of gold electrodes was used as the substrate for the FET-type sensor platform. To functionalize the IDA surfaces, the IDA substrate was treated with 3-aminopropyltrimethoxysilane (APS) containing the amino group. Subsequently, the CFMNSs were introduced to the APS-functionalized IDA substrate. Then, the CFMNSs were successfully immobilized on the functionalized surface through a condensation reaction between the amino group ($–NH_2$) placed on the substrate surface and the carboxyl group (–COOH) of the CFMNSs. Reaction with the condensing agent 4-(4,6-dimethoxy-1,3,5-triazin-2-yl)-4-methylmorpholinium (DMT-MM) resulted in the formation of chemically stable amide bonds (–CONH–) [182]. Similarly, Ars-3 aptamers were bound to the CFMNSs through covalent bonding. The interaction between the carboxyl group (–COOH) of the CFMNS and the amino group ($–NH_2$) at the 3′ terminus of the binding aptamer formed covalent bonds, resulting in the Ars-3 aptamer-conjugated CFMNS (Apt-CFMNS). Spectrophotometric measurements were carried out to quantify the immobilized aptamer on the FMNSs and

CFMNSs (**Figure 49**). The results showed that *ca*. 90% of the aptamers remained on the CFMNSs after washing process. Although the delocalized electrons of MoS_2 outer layers could lead to π–π stacking interactions with the nucleotide base of the aptamer [183], only *ca*. 50% of the aptamers were immobilized on the washed FMNSs. Compared with the FMNSs, excellent immobilization on the CFMNSs was achieved due to strong, stable covalent bonding. Consequently, an FET-type aptasensor system based on the Apt-CFMNS was successfully fabricated on the IDA electrode.

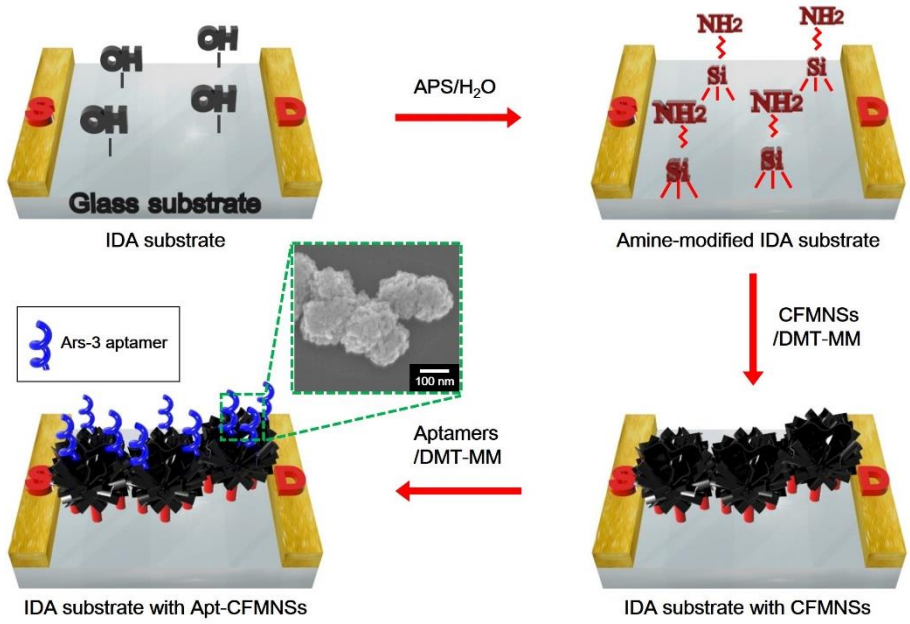

Figure 48. Schematic illustrations for the immobilization procedure of aptamer-conjugated CFMNSs (Apt-CFMNSs) on the electrode. SEM image (inset) of Apt-CFMNSs.

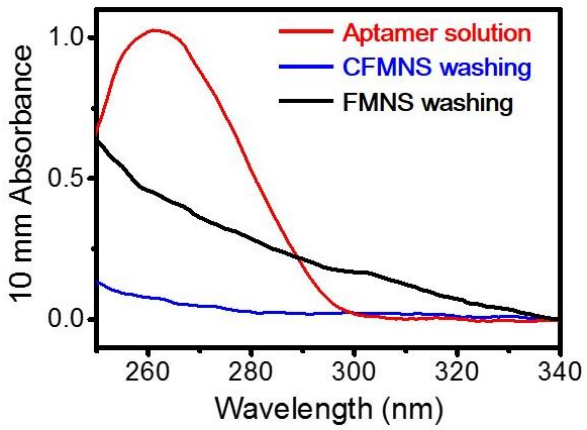

Figure 49. The absorbance of immobilized aptamer on FMNS and CFMNS surfaces before and after washing.

3.3.5 Electrical characteristics of CFMNSs

To investigate the electrical characteristics of the FET-type sensor platform, current–voltage (*I*–*V*) curves were observed. The d*I*/d*V* value of the CFMNS electrode was several orders of magnitude higher than that of the FMNS electrode, which implied that the CPPy coating on the FMNS surfaces provided greatly enhanced conductivity. In addition, the CPPy layer transformed the non-linear curve of the FMNS into the linear curve of the CFMNS (**Figure 50a**). **Figure 50b** depicts the *I*–*V* curves for the sensor electrodes using CFMNSs and Apt-CFMNSs as transducer materials. The curves indicate the electrical changes before and after the attachment of the binding aptamers. The *I*–*V* relationship remained linear over a voltage range from −1 to 1 V, although the d*I*/d*V* value decreased slightly after aptamer immobilization due to a moderately increased resistance. The linear property of the *I*–*V* relationship indicated stable ohmic behavior and that reliable electric contact was preserved. These results suggest that a conductive channel based on Apt-CFMNSs could maintain good electrical contact, and that the channel could provide an effective signal pathway for specific binding interactions. A liquid-ion gated FET system was prepared to examine the possibility of using Apt-CFMNSs as transducers in the liquid-ion gated FET configuration.

Figure 51a portrays the experimental setup of the FET system, which included the Apt-CFMNSs as the conductive channel and gold electrodes as the source (*S*) and drain (*D*). The FET sensor was surrounded by phosphate-buffered saline (PBS; pH 7.4) as an electrolyte; a gate electrode was located in the electrolyte solution. **Figure 51b** shows the output characteristics of the sensor under varying gate voltages (V_g) ranging from 0.2 to −0.8 V. The source-to-drain current (I_{sd}) became more negative with increasing negative gate voltage, which indicated that the FET sensor behaved like a p-type semiconductor (hole-transporting). Moreover, the stable modulation of the I_{sd} value was maintained across the varying V_g, which indicated that the current changes occurred by the electrostatic gating effect, rather than by contact resistance. These electrical characteristics suggest that the liquid-ion gated Apt-FMNSs FET sensor is capable of detecting a signal change when the Ars-3 interacts with target molecules.

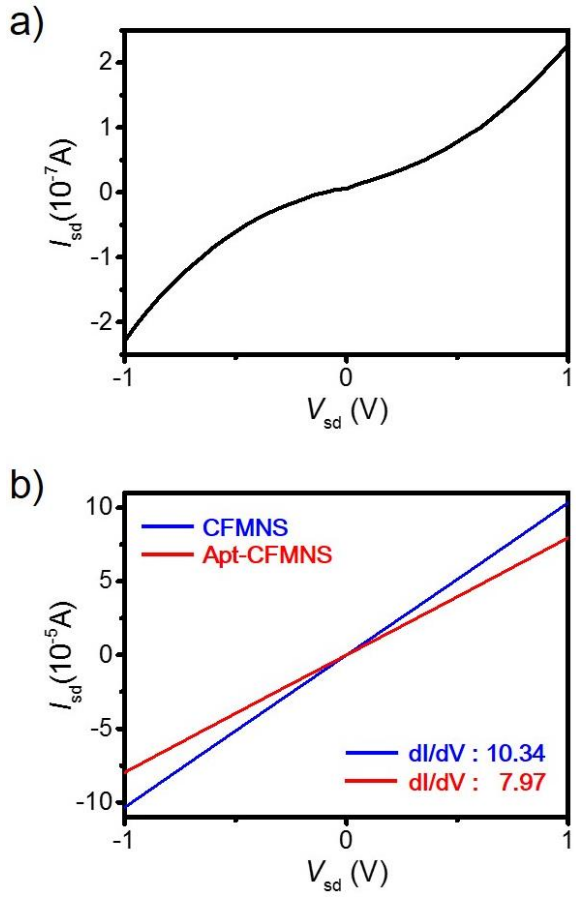

Figure 50. (a) Current–voltage (*I–V*) curve of FMNSs-based electrode. (b) Current–voltage (*I–V*) relations of MoS_2-based sensor before and after the introduction of aptamer.

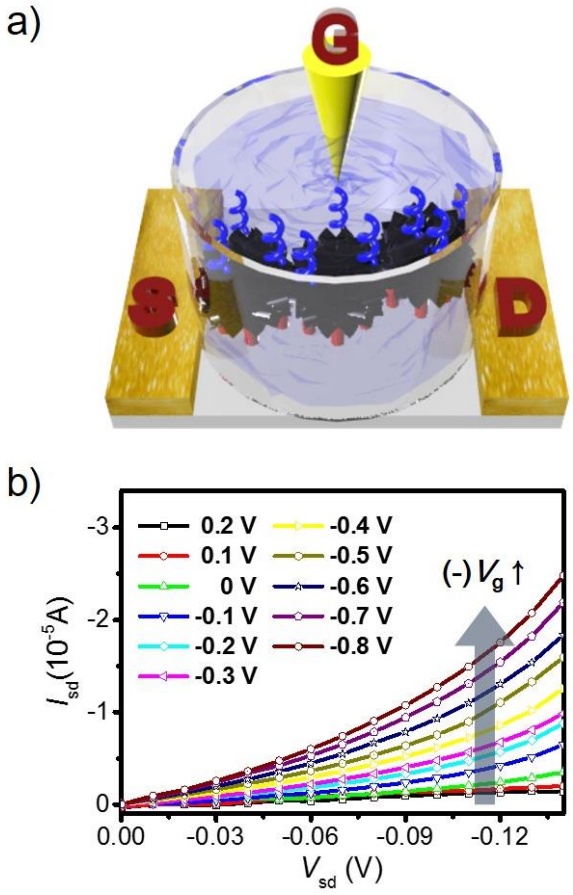

Figure 51. (a) Illustrative diagram of liquid-ion gated FET sensor using Apt-CFMNSs as transducers. (b) Output characteristics of Apt-CFMNSs FET-type sensor under different gate voltage (V_g, 0.2 to –0.8 V in a step of –0.1 V, and V_{sd}, 0 to –0.14 V in a step of –10 mV).

3.3.6 Real-time responses of CFMNS aptasensor toward arsenite

Figure 52a reveals the real-time responses of the aptasensors using FMNSs and CFMNSs. The I_{sd} values immediately increased after adding various As(III) concentrations. This result suggests that the introduction of As(III) in the sensor platform could be detected by observing the current changes that occur *via* a specific interaction between the As(III) as the target analyte and the binding aptamer as the receptor. A plausible sensing mechanism is proposed based on the change in surface charge. An increasing current was induced by the accumulation of hole carriers elicited through the aptamer/arsenite binding interaction. Because the As(III) ion has three hydroxyl groups (–OH) in PBS solution, it can be easily bound to the ssDNA aptamer. The –OH groups of the As(III) were linked to the amine groups ($–NH_2$) of the aptamer bases through strong hydrogen bonds [184]. The single-stranded DNAs transformed into a folded and condensed structure by chemical bonds, which resulted in negative charges in the liquid-ion dielectric near the CFMNS surface [185]. Consequently, positive charge carriers accumulated on the CFMNS transducer. The accumulated holes applied a p-type doping impact indirectly to the gate dielectric. **Figure 52a** shows that both the FMNSs and CFMNSs FET aptasensors had outstanding response speeds

(on a time scale of less than 1 s). However, there were differences in sensing performance between the Apt-FMNSs and Apt-CFMNSs aptasensors. The minimum detectable level (MDL) in the Apt-CFMNSs sensor was 100-times more sensitive than that of the Apt-FMNSs sensor. Moreover, the Apt-CFMNSs sensor displayed a larger current change than the Apt-FMNSs sensor when As(III) was introduced into the FET configuration. The extraordinary performance of the Apt-CFMNSs originated from the aforementioned advantages of the CPPy layer. The CPPy layer provided high conductivity, stable contact, and immobilized more aptamers to the FET sensors, leading to improved sensing performance. The MDL of the Apt-CFMNSs sensor was 1 pM (with a signal-to-noise ratio of 4.57) and was two- to four orders of magnitude more sensitive than that of previous arsenite sensors using electrochemical methods (**Table 2**) [186-188]. Interestingly, the CFMNSs sensor without aptamers used as a control sample displayed only negligible variation. It was apparent that the ars-3 aptamers interacted with target As(III). **Figure 52b** delineates the sensitive change (S) as a function of the As(III) concentration. The Apt-CFMNSs sensor was more sensitive than the Apt-FMNSs sensor. The sensitivity of the Apt-CFMNSs steadily increased as the As(III) concentration increased

in the wide range from 1 pM to 10 nM. Moreover, the sensitive change of the Apt-CFMNSs to As(III) was linear and followed the relationship

S(%) = 9.505 + 6.775logC where C is the As(III) concentration in units of pM.

Figure 53 exhibits the selective responses of the Apt-CFMNSs FET sensors toward As(III). The selective test was conducted using the following non-target metal ions: Fe^{2+}, Zn^{2+}, Mg^{2+}, Cu^{2+}, Mn^{2+}, Li^{+}, Cd^{2+}, Co^{2+}, and Ni^{2+}. Although the non-target metal ions were present at significantly higher concentrations (1 μM) than the As(III) concentration (1 pM), no significant variations occurred when non-target ions were introduced to the FET sensors. However, the I_{sd} values changed remarkably upon the addition of 1 pM concentration of As(III) as the target analyte. Considering these results, the arsenite sensor was able to differentiate the target As(III) from non-target metals with exceptional selectivity.

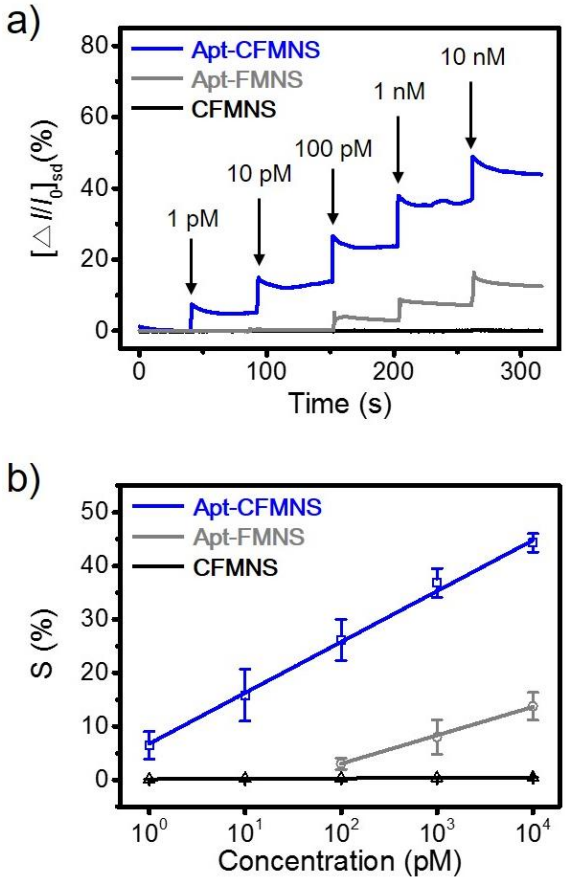

Figure 52. Discrimination of target As(III) with different sensors using CFMNS (black line), Apt-FMNS (gray line), and Apt-CFMNS (blue line). (a) Real-time responses and (b) calibration curves toward various As(III) concentrations (1 pM to 10 nM).

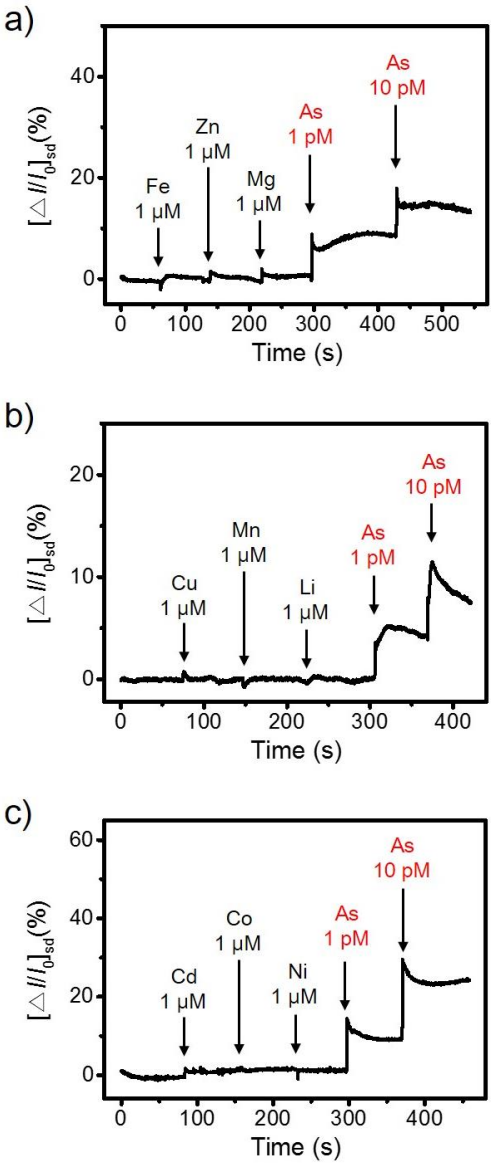

Figure 53. (a-c) Selective responses of Apt-CFMNSs FET sensor toward target analyte (As(III), 1pM) and nontarget metal ions (Fe^{2+}, Zn^{2+}, Mg^{2+}, Cu^{2+}, Mn^{2+}, Li^{+}, Cd^{2+}, Co^{2+}, and Ni^{2+}, 1 μM).

Table 2. Sensing performance compared with previous researches using electrochemical method.

Detection methods	Sensing materials	Detection limit	Reference
Electrochemistry	Au NPs[a)]	200 pM	123
Electrochemistry	Ag/Go[b)] nanocompsites	240 pM	186
Electrochemistry	FePt NPs	10 nM	187
Electrochemistry	SnO^2 NSs[c)]	50 nM	188
Electrochemistry(FET)	CFMNSs[d)]	1 pM	This work

a) NP, nanoparticle; b) GO, graphene oxide; c) NS, nanosheet; d) CFMNS, carboxylated polypyrrole coated-flower like MoS_2 nanosphere.

3.3.7 Real-time response of MoS_2 based-aptasensor toward a real sample

To further exploit the selectivity of the FET aptasensor, additional experiments were conducted using the mixture of 1 μM concentrations of the non-target metal ions (**Figure 54a**). No notable changes were observed following the injection of the mixture sample, whereas significant current changes were observed upon the introduction of mixture samples containing 1 pM and 10 pM concentrations of As(III). This result indicated that the FET aptasensor could selectively detect As(III) in a complex mixture. Response experiments were conducted using real water samples to explore the possibility of using the FET aptasensor for practical applications. A water sample taken from the Han River in Seoul was used as the real water sample. Inductively coupled plasma-atomic emission spectrometry (ICPS) was used to measure the concentrations of arsenic and non-target metals in the real sample. The river water sample contained arsenic at a concentration of *ca*. 5 μM (**Table 3**). The addition of the pristine river sample changed the current signal (**Figure 54b**). Subsequently, the Isd of the liquid-ion gated FET sensor further increased when the river water sample was spiked with As(III) at a concentration of 5 μM. These crucial results demonstrate that

the FET sensor is capable of discriminating As(III) in real water samples and suggest its potential for practical applications.

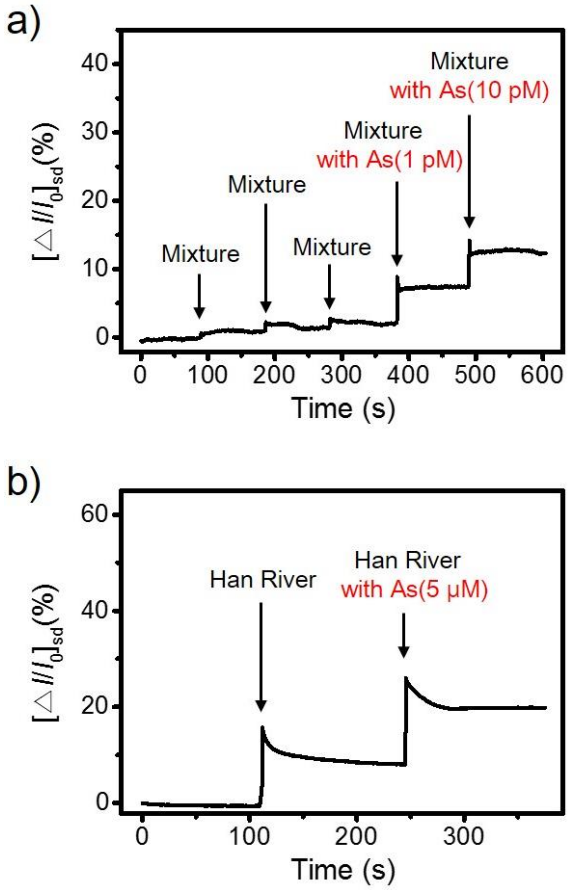

Figure 54. (a) Selective response of Apt-CFMNSs FET sensor toward 1 pM, and 10 pM concentrations of As(III) in mixture containing 1 μM of the nontarget metal ions. (b) Real-time response from river water as real water sample.

Table 3. Inductively Coupled Plasma-Atomic Emission Spectrometer (ICPS) analysis for Han River.

Metal	Weight concentration (mg/L)	Molar concentration (mM)
As	0.381	0.0052
Mg	8.488	0.3486
Fe	0	0
Zn	0	0
Cu	0	0
Mn	0	0
Li	0	0
Cd	0	0
Co	0	0
Ni	0	0

3.4 Fabrication of H_2O_2 sensor based on MoS_2 nanosheets grown on CVD graphene

3.4.1 Fabrication of MoS_2 nanosheets grown on graphene substrate

Figure 55 describes the overall procedure for the preparation of MoS_2 nanosheets-decorated CVD graphene (MNSCG). Graphene was utilized as a transducer because of its outstanding properties such as superior conductivity and high carrier mobility. The graphene was grown on a Cu substrate *via* CVD method with gas precursors containing methane (CH_4) and Hydrogen (H_2). The Cu substrate was removed by the etching process with a Cu-etchant, and the graphene was transferred onto a SiO_2 wafer substrate using wet-transfer method. Subsequently, a thermo-electrostatic bonding (TEB) method was conducted to enhance adhesion between the graphene and SiO_2 wafer substrate [189]. This method was proceeded by annealing and electrostatic force, and it improved the contact area of graphene to the SiO_2 substrate. Before the hydrothermal process, the graphene surface was exposed to 1,5-diaminonaphthalene (DAN), enabling the surface to be functionalized with amino groups. The DAN was placed on the graphene surface through π–π bonding between aromatic structure of the graphene and phenyl groups of the DAN. Then, MoS_2 nanosheets were grown on the

graphene substrate by a simple hydrothermal method. Sodium molybdate (Na_2MoO_4) and thiourea ($CS(NH_2)_2$) were used as precursors. The hydrothermal reaction could be expressed as follows [190,191]:

(1) $CS(NH_2)_2 + 2H_2O \rightarrow CO_2 + H_2S + 2NH_3$

(2) $4Na_2MoO_4 + 9H_2S + 3CO_2 \rightarrow 4MoS_2 + Na_2SO_4 + 3CO_3^{2-} + H_2O$

Thiourea acted as a sulfur source and a reducing reagent in the reactions [192]. Thereafter, annealing process was conducted at 600°C for 1 h. The source (*S*) and drain (*D*) electrodes were deposited on the sensor substrate by the thermal evaporation. To confirm the difference between DAN-treated and -untreated MNSCGs, FE-SEM analysis was performed. As shown in **Figure 56a**, the DAN-untreated MNSCG had unordered structure. This result suggested that Mo precursor interacted with various functional group on the graphene surface originated from oxygen, moisture, and synthesis process [193]. In case of DAN-treated MNSCG, the synthesized structure showed ordered nanosheets with zigzag pattern on the graphene surface (**Figure 56b**). The result indicated that Mo^{4+} ions preferentially reated with the nitrogen atoms of DAN than the other functional groups. In addition, the structure of nanosheets featured a highly open structure, which provided high active surface area.

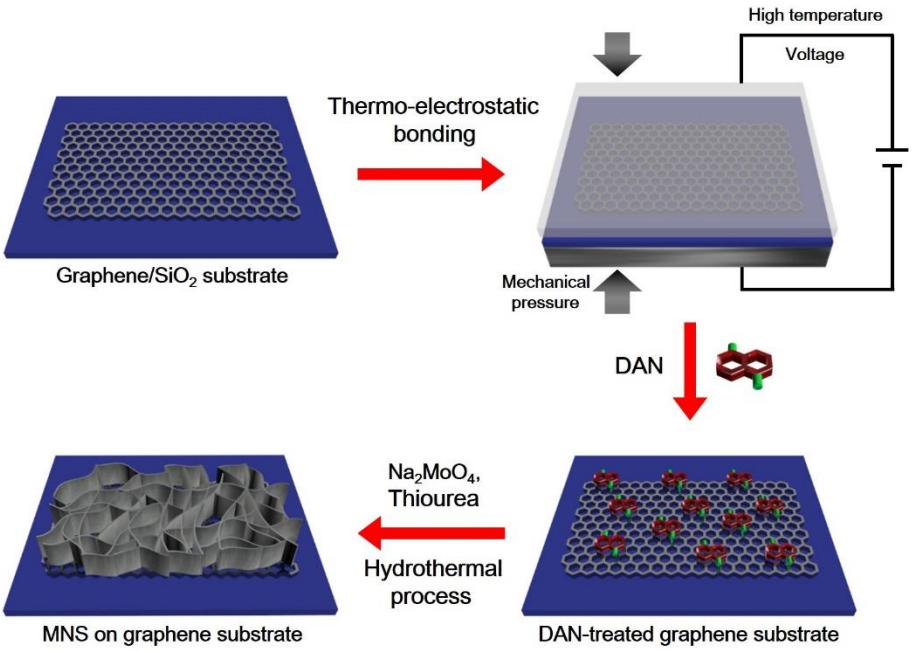

Figure 55. Schematic illustrations for the preparation steps of MNSCG.

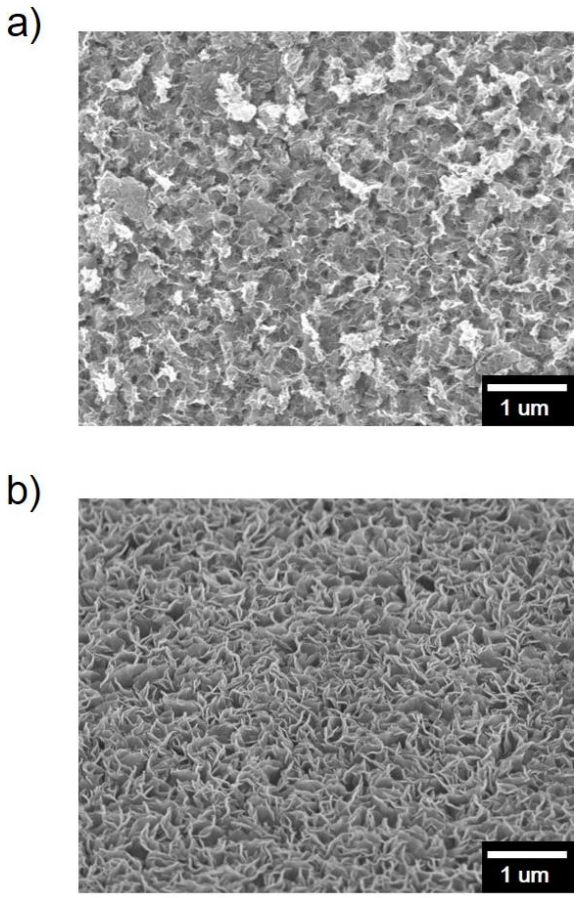

Figure 56. FE-SEM images of MNSCG (a) untreated with DAN and (b) treated with DAN.

3.4.2 Characterization of MNSCG

Figure 57a and b show FE-SEM images of different population of MNSs. The MNSs-decorated CVD graphene using 0.001 and 0.05 M DAN are denoted MNSCG_L and MNSCG_H, respectively. The population increased with higher DAN concentration, which revealed that the number of Mo nuclei was influenced by the DAN concentration. **Figure 58a-d** demonstrate that the MNS structure is also affected by precursor quantity and reaction time. Compared to the optimum quantity of precursor (**Figure 58a**), the excess amount of precursor gave rise to the unwanted small aggregations (**Figure 58b**). The growth of MNSs was not enough when reaction time decreased for the hydrothermal process (**Figure 58c**). Conversely, the microsphere structure of MNSs was observed with increasing reaction time, leading to the increased resistance on the MNSCG (**Figure 58d**). Raman analysis provides meaningful information about the DAN treatment on the graphene surface. As shown in **Figure 59**, absorption bands at 3413^{-1} and $3319–3233^{-1}$ corresponded to the asymmetric and symmetric N–H stretches of aromatic primary amino groups, respectively. Furthermore, two peaks at 1364 and 1294 cm^{-1} were assigned to the C–N stretching vibration of primary amino groups [194]. To determine the chemical composition of

the MNSs grown on the graphene, X-ray Photoelectron Spectroscopy (XPS) analysis was conducted (**Figure 60**). The survey scan spectrum demonstrated that only C, O, and Si were present in the pristine graphene, although Mo, S, and N peaks were represented in the spectrum of MNSCG. Further insight into the nanostructure of MNSCG was obtained using Raman analysis. The two distinctive peaks of MNSCG_L and MNSCG_H at 378 and 408 cm^{-1} corresponded to the E^1_{2g} and A^1_g modes of the hexagonal MoS_2 structure, respectively (**Figure 61a**) [195]. The E^1_{2g} mode is associated with the in-layer displacement of Mo and S atoms, whereas the A^1_g mode is assigned to the out-of-layer symmetric displacements of S atoms along the c axis [196]. Consistent with the XPS result, there was no dominant peak in the pristine graphene spectrum. **Figure 61b** shows Raman spectra containing the G and 2D peaks as the most characteristic peaks of graphene. The I_{2D}/I_G intensity ratio decreased with increasing MoS_2 growth on the graphene surface. In addition, the 2D peak was slightly upshifted when the MoS_2 nanosheets were grown. These results were caused by charge impurity or rippling on the graphene surface [197,198].

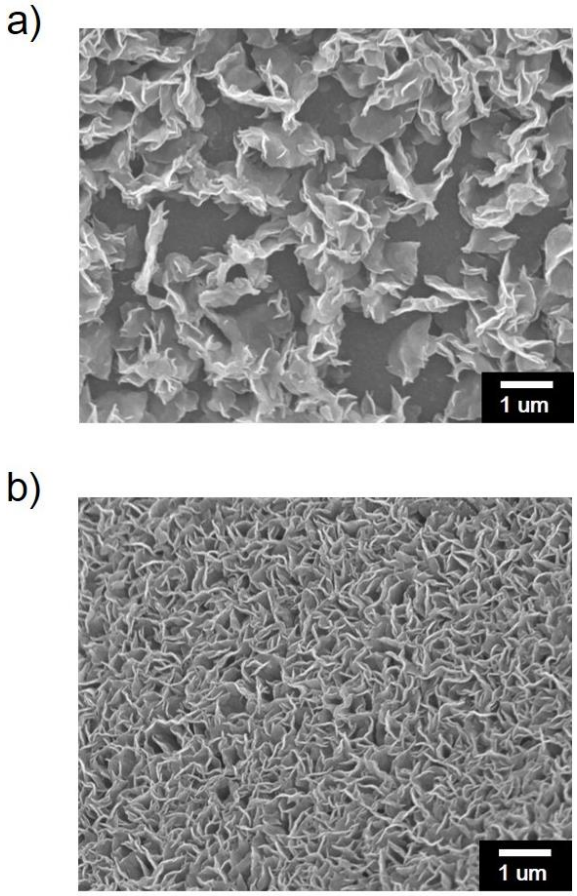

Figure 57. FE-SEM images of (a) MNSCG_L and (b) MNSCG_H.

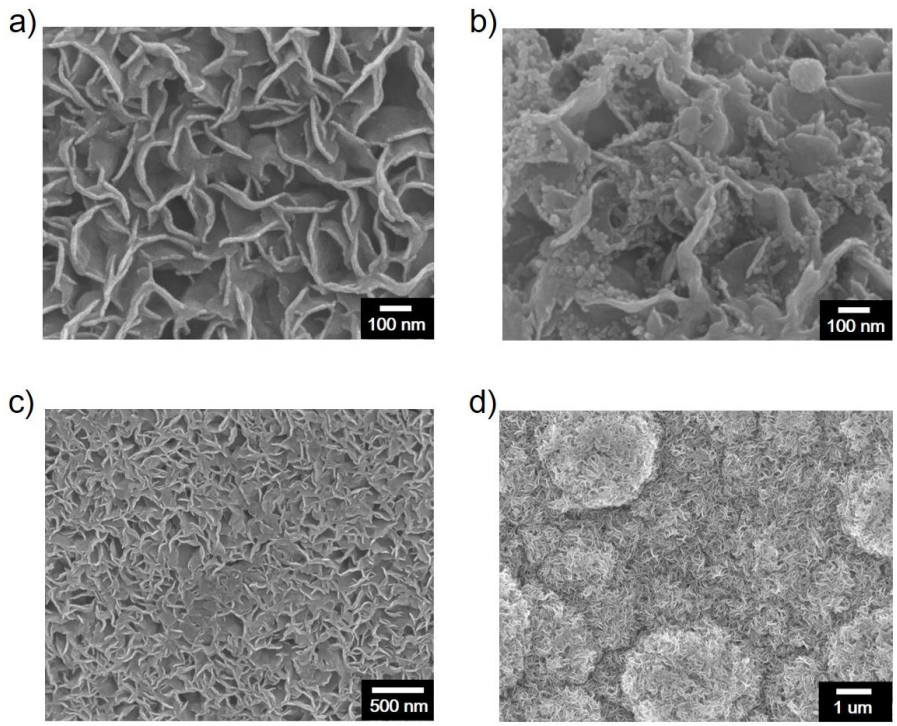

Figure 58. FE-SEM images of MNSCGs with (a) the optimum and (b) the excess amount of precursors. SEM images of MNSCGs reacted for (c) 6 hr and (d) 18 hr, respectively.

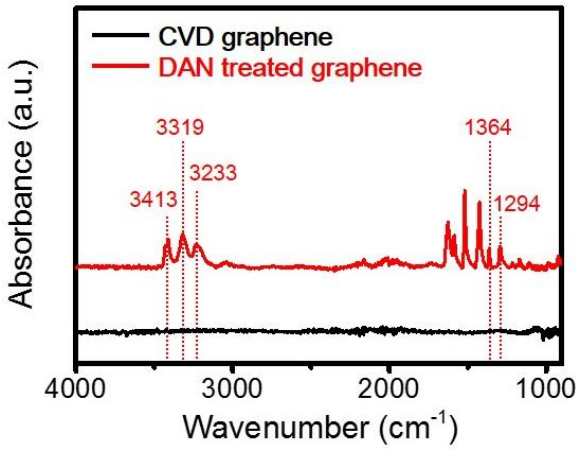

Figure 59. FT-IR spectrum of CVD graphene unmodified (black line) and modified (red line) with DAN.

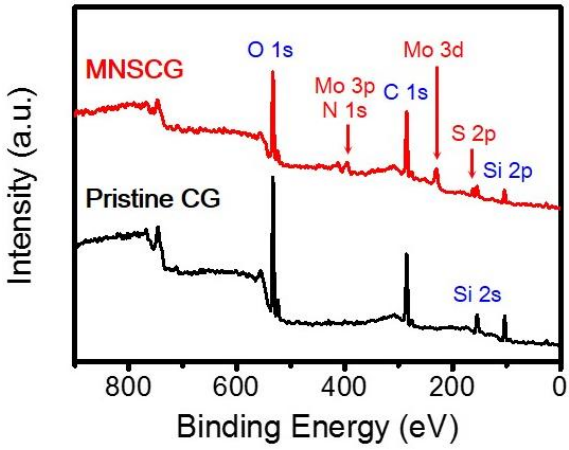

Figure 60. Fully scanned XPS spectra of Pristine CG (black line) and MNSCG (red line).

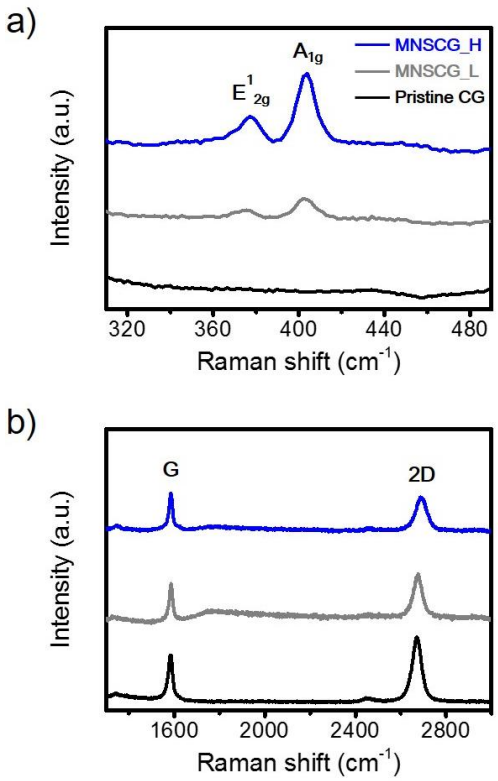

Figure 61. (a), (b) Raman spectra of Pristine CG (black line), MNSCG_L (gray line), and MNSCG_H (blue line).

3.4.3 Electrical properties of MNSCG

Current−voltage ($I-V$) measurement was investigated to explore the electrical characteristics of the FET-type H_2O_2 sensor. **Figure 62a** displays the dependence of current *versus* voltage before and after the MoS_2 growth on CVD graphene. The linearity of $I–V$ curves was maintained over a voltage range from −0.5 to 0.5 V, although the dI/dV value slightly decreased with increasing MoS_2 population. The result revealed that the FET sensor maintained stable ohmic behavior and reliable electric contact after the MoS_2 introduction. It can be concluded that the MNSCG as a transducer provide an efficient current pathway for specific binding reactions. To evaluate the possibility to utilize MNSCG channels as transducers in the FET configuration, a liquid-ion gated FET system was prepared. The FET-type H_2O_2 sensor was surrounded by phosphate-buffered saline (PBS; pH 7.4) as an electrolyte. A gate electrode was introduced in the PBS electrolyte to apply different gate potentials to the FET system. **Figure 62b** presents the output behaviors of the H_2O_2 sensor under various gate voltages (V_g) in a step of −0.1 V (0 to −0.6 V). The source-to-drain current (I_{sd}) became more negative with negatively increased V_g, which indicated that positive holes were major carriers in this system (P-type semiconductor). In addition, the

stable contact remained under the varying gate volgates, suggesting that the current variation mainly occurred by the electrostatic gating effect. Judging from these electrical results, the liquid-ion gated FET sensor can observe a signal change created by the interaction between the sensor and target H_2O_2.

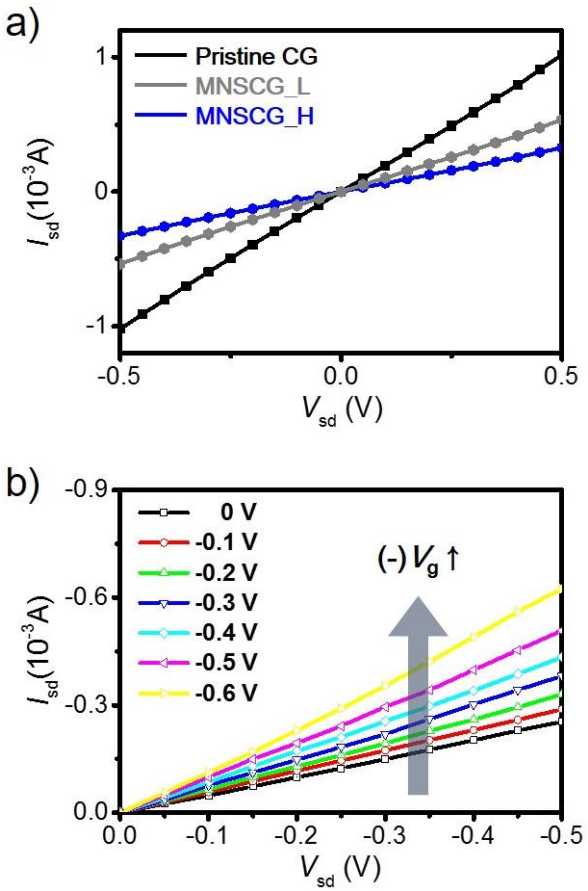

Figure 62. (a) Current–voltage (*I*–*V*) curves of Pristine CG, MNSCG_L, and MNSCG_H. (b) Output properties of MNSCG_H sensor under various gate voltage (V_g, 0 to –0.6 V in a step of –0.1 V, and V_{sd}, 0 to –0.5 V in a step of –50 mV).

3.4.4 Real-time responses of FET-type H_2O_2 biosensor based on MNSCG electrode

Exploring the possibility to detect target H_2O_2, real-time responses of the FET-sensors were observed (**Figure 63a**). The Pristine CG sensor, as a control sample, displayed only slight variation toward H_2O_2. However, the I_{sd} values rapidly decreased after adding various H_2O_2 concentrations in case of FMNS, MNSCG_L, and MNSCG_H sensors. The result reveals that the H_2O_2 addition in the MoS_2-based sensors could be detected by monitoring the I_{sd} changes. In other words, a specific interaction between the H_2O_2 and MoS_2 changes the currents. MoS_2 nanomaterials have been studied as an intrinsic peroxidase-like catalyst that can be used for H_2O_2 monitoring [199]. According to the literature, the possible interaction can be described as follows [200,201]:

(1) $H_2O_2 + MoS_2 \rightarrow HO + MoS_2 + MoS_2OH$

(2) $H_2O_2 + HO \rightarrow HOO + H_2O$

(3) $MoS_2OH + HOO \rightarrow H_2O + O_2 + MoS_2$

In addition, electrochemical sensors combined with MoS_2 exhibited outstanding electro-catalytic activities toward the reduction of H_2O_2 [202,203]. Based on these features of MoS_2, **Figure 64** delineates the sensing mechanism of the FET-type sensor. The reduction of added H_2O_2

occurred by the electro-catalytic effect of the MoS_2 nanosheets, which induced positive charges on the MNS surface. The accumulated charges applied a positive gate impact on the graphene surface. The hole density in the charge transfer pathway decreased by the positive gate effect, which resulted in reduced current. As shown in **Figure 63a**, although the detection limit of FMNS was low enough (100 nM), the sensitivity of MNSCG_L was higher than the FMNS. The enhanced sensitivity originated from the outstanding properties of CVD graphene. When graphene is utilized as a transducer in FET-type sensors, the graphene provides improved signal pathway because of its high conductivity and fast carrier mobility. The minimum detectable level (MDL) of the MNSCG_H was unprecedentedly low value (*ca*. 1 nM) that was two- to three orders of magnitude lower than that of other MoS_2 based sensors (**Table 4**) [204-208]. The MNSCG_H sensor was more sensitive than the MNSCG_L due to the increasing population of MoS_2 nanosheets. **Figure 63b** depicts the calibration curves as a function of H_2O_2 concentration. The sensitive change (S) was defined from the saturation value of the normailized signal changes. The calibration value presented the decreasing tendency upon the addition of higher concentrations of H_2O_2.

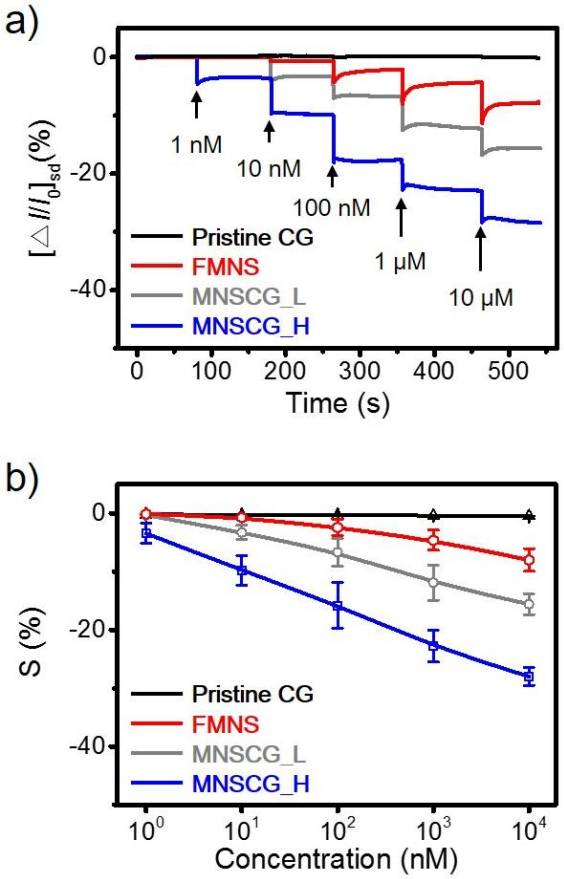

Figure 63. Detection of H_2O_2 with diverse sensors using Pristine CG (black line), FMNS (red line), MNSCG_L (gray line), and MNSCG_H (blue line). (a) Real-time measurements and (b) calibration curves toward various H_2O_2 concentrations (1 nM to 10 μM).

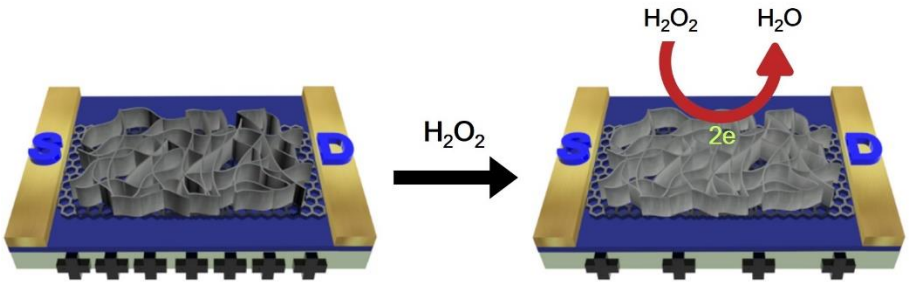

Figure 64. Schematic illustration depicting H_2O_2 sensing mechanism of MNSCG sensor based on non-enzymatic reaction.

Table 4. H_2O_2 sensing performance of this work compared with previous studies.

Detection methods	Sensing materials	Detection limit	Reference
Colorimetirc detection	SDS-MoS_2 NPs[a)]	320 nM	203
Colorimetirc detection	PVP-MoS_2 NPs[b)]	1.3 μM	204
Electrochemistry	Mb-MoS_2 NSs[c)]	1.25 μM	205
Electrochemistry	AuPd-MoS_2 NSs	160 nM	206
Electrochemistry	Au NR-MoS_2 NSs[d)]	100 nM	207
Electrochemistry(FET)	MNSCG[e)]	1 nM	This work

a) SDS, sodium dodecyl sulfate; NP, nanoparticle; b) PVP, polyvinylpyrrolidone; c) Mn, myoglobin; NS, nanosheet; d) NR, nanorod; e) MNSCG, MoS_2 nanosheets grown on CVD graphene.

3.4.5 Selective response and reusability of MNSCG sensor

Figure 65a represents the selective response of the MNSCG sensor toward H_2O_2. The selectivity was evaluated using uric acid (UA) and ascorbic acid (AA) as non-target biomolecules. No meaningful change was monitored when the MNSCG sensor was exposed to the biomolecules, although the concentration of the biomolecules (1 μM) was considerably higher than that of H_2O_2 (1 nM). However, the signal was remarkably altered by the addition of 1 nM H_2O_2, which was apparent change (signal-to-nosie: 3.57). Accordingly, the liquid-ion gated FET sensor demonstrates the ability to detect H_2O_2 with high selectivity and sensitivity. **Figure 65b** shows the reusable property of the MoS_2-based sensor (the sensitivity changes were calculated as S/S_0, where S_0 is the saturation sensitivity of first test and S is the measured sensitivity). The reusable property was proved by inspecting the current changes upon the introduction of 1 μM H_2O_2 for ten times. The reusable process is composed of two steps: (i) introduction of the H_2O_2 into the sensor, (ii) washing with PBS, and then drying under nitrogen stream. The FET-type sensor showed an efficient repeatability with 1 μM H_2O_2 concentration. The sensitivity decreased slightly at tenth test (*ca*. 10%), which indicated that the sensor featured excellent reusability. In addition,

the morphology of the MNSCG remained without structural change and collapse after the tenth addition of 1 μM H_2O_2 as shown in **Figure 66a and b**. Because reusable property is important for practical sensors, the good reusability of the non-enzymatic sensor enables it to be utilized in practical applications.

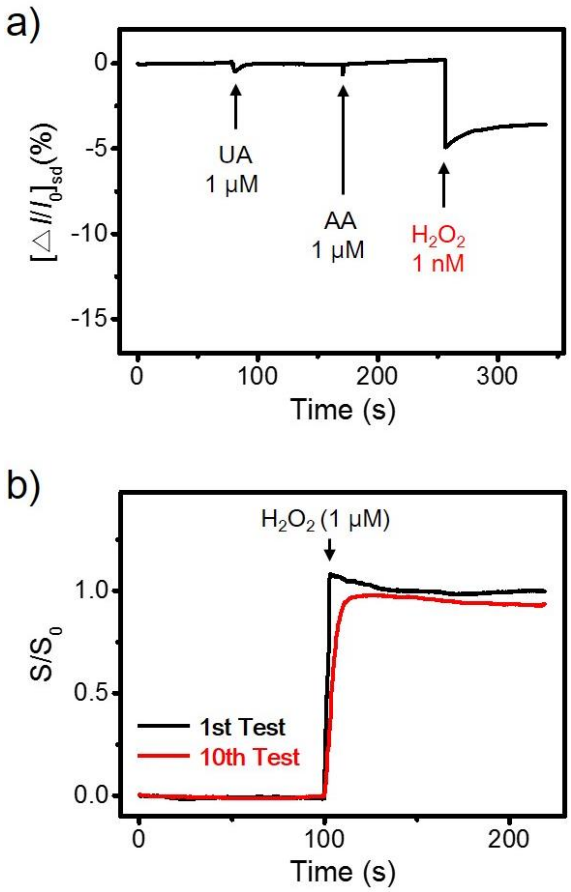

Figure 65. (a) Selective response of MNSCG sensor toward target H_2O_2 (1 nM) and non-target biomolecules (uric acid (UA) and ascorbic aicd (AA), 1 μM). (b) Reusability of non-enzymatic MNSCG sensor upon the first (black) and tenth (red) addition of 1 μM H_2O_2.

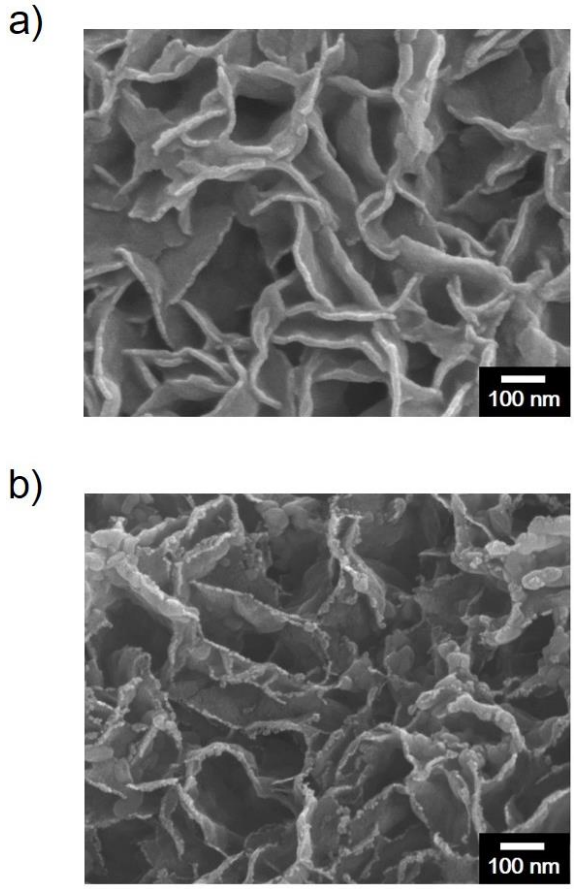

Figure 66. FE-SEM images of MNSCG after (a) the first and (b) the tenth addition of 1 μM H_2O_2.

4. Conclusion

The graphene and molybdenum disulfide nanomaterials were fabricated *via* chemical vapor deposition (CVD) and hydrothermal methods and the prepared materials demonstrated attractive properties for the biosensor applications. The subtopics could be concluded as follows:

1. A liquid-ion gated FET-type graphene-based aptasensor was prepared with highly sensitive and selective responses to various HBsAg concentrations. The aptasensors consisted of a single layer graphene, with the graphene surface functionalized using an aptamer that binds specifically to target HBsAg. The sensing capability of the aptasensor was verified by real-time measurements, which showed unprecedentedly minimum detectable level (10 fM) and rapid response time of < 1 s. Moreover, the aptasensor displayed outstanding selectivity toward HBsAg. Based on the exceptional sensing abilities, the aptasensor was applied to discriminate HBsAg in artificial and real saliva as real samples, resulting in the high selectivity toward HBsAg. In addition, the aptasensor also had excellent flexibility. From these results, the FET-type aptasensor

based on graphene can provide an advanced methodology of HBsAg sensing devices and be broadly applied analytical real-sample applications.

2. The human mimicking duplexed bioelectronic tongue (DBT) was successfully fabricated based on the multiple graphene electrodes functionalized with the heterodimeric human taste receptor nanovesicles. The taste sensor had high sensitivity and selectivity toward target tastants. It featured an ability to mimic the human taste system for the recognition of sweet and umami tastants. The DBT platform delineated outstanding responses for each umami and sweet tastant. On the basis of the high performance, the duplex sensor was utilized to simultaneously detect both umami and sweet tastants. The multiplexed detections were successfully achieved with the human-like responses. In addition, the DBT sensor has the ability to detect target tastants in real food samples (tomato juice and green tea) and can be utilized in practical applications. Accordingly, the DBT system can overcome the disadvantages of previous artificial taste sensors containing poor selectivity, low sensitivity, and impossibility to discriminate unknown molecules. Furthermore, this research is

expected to provide an efficient method to prepare a highly sensitive taste sensor for practical applications such as food and beverage industry.

3. A liquid-ion gated FET sensor for arsenic was successfully manufactured and based on aptamer-conjugated CFMNSs as a transducer. The CFMNSs were readily prepared through simple hydrothermal and vapor deposition processes. The flower-like structure of the CFMNSs provided a large specific surface area, which enabled the loading of a considerable number of aptamers. Coating with a layer of CPPy played a pivotal role in improving the sensing performance due to its functional group and high conductivity. The FET-type aptasensor exhibited a rapid response time of <1 s, enabling real-time detection of As(III). The minimum detectable level (MDL) of the arsenic sensor was 1 pM, which is two- to three orders of magnitude more sensitive than that of previous electrochemical sensors. Moreover, the MoS_2-based aptasensor selectively discriminated As(III) from numerous other metal ions and accurately detected As(III) in a mixed solution. This FET-type sensor detected target As(III) in real samples of river water.

These findings demonstrate the potential of this FET sensor in advanced As(III) analyzers for a wide range of practical applications.

4. The MoS_2 nanosheets grown on CVD graphene (MNSCG)-based nonenzymatic H_2O_2 sensor was successfully fabricated using surface modification and hydrothermal process. MoS_2 nanosheets were grown on the graphene surface during the hydrothermal process. The population of the MNS was modulated by the concentration of DAN solution. A FET-type nonenzymatic sensor using MNSCG electrode could detect H_2O_2 with high sensitivity and rapid response time of< 1s. The more populated morphology (MNSCG_H) had more reaction sites to interact with H_2O_2, leading to enhanced sensitivity (1 nM). Moreover, the FET-type sensor showed outstanding selectivity toward H_2O_2 among other biomolecules due to the intrinsic peroxidase-like property of the MoS_2 nanostructure. Furthermore, the good repeatability was also demonstrated. The morphology of MNSCG remained without structural change and collapse after reusable test. This research offers a promising tool and convenient methology to fabricate a highly sensitive and stable nonenzymatic sensor.

In summary, three different morphologies of nanostructures were used as transducers for biosensor applications. First, graphene, two dimensional structures with hexagonal honeycomb lattice, was fabricated using chemical vapor deposition (CVD) process. CVD graphene was applicated to HBsAg and taste sensors, revealing high sensitivity, selectivity, and rapid response time owing to its extraordinary carrier mobility and high conductivity. Second, molybdenum disulfide (MoS_2), which is a layered TMD, was prepared by a simple hydrothermal method. A hexagonal lattice with the Mo and S_2 atoms is similar to the graphene structure. The morphology of flower-like MoS_2 nanospheres (FMNSs) was controlled by the amount of hydrazine. After vapor deposition polymerization (VDP), carboxylated polypyrrole-coated FMNSs exhibited enhanced performance in As(III) sensing application. Lastly, MoS_2/graphene nanocompsite was prepared by hydrothermal process. MoS_2 nanosheets (MNSs) were grown on graphene surface, and the population of MNSs was modulated by the surface modification with diamino naphthalene (DAN). The nanocomposite was adopted to fabricate a highly sensitive FET-type nonenzymatic sensor for H_2O_2 detection.

The graphene and MoS_2 nanomaterials have been successfully

applied in versatile biosensor application. The high performance of these materials as signal transducers in sensor system was demonstrated. Therefore, these materials may offer a promising potential in further applications related to nano-electronic devices, chemical/pressure sensor, conductive nanocomposites, actuators, catalyst, and biomedical engineering.

References

[1] M. P. Byfield, R.A. Abuknesha, *Biosens. Bioelectron.* **1994**, 9, 373.

[2] K. Besteman, J. O. Lee, F. G. M. Wiertz, H. A. Heering, C. Dekker, *Nano Lett.* **2003**, 3, 727.

[3] J. A. Goode, J. V. H. Rushworth, P. A. Millner, *Langmuir* **2015**, 31, 6267.

[4] A. P. F. Turner, *Chem. Soc. Rev.* **2013**, 42, 3184.

[5] S. Afreen, K. Muthoosamy, S. Manickam, U. Hashim, *Biosens. Bioelectron.* **2015**, 63, 354.

[6] A. Amine, H. Mohammadi, I. Bourais, G. Palleschi, *Biosens. Bioelectron.* **2006**, 21, 1405.

[7] B. G. Trewyn, S. Giri, I. I. Slowing, V. S. Y. Lin, *Chem. Commun.* **2007**, 31, 3236.

[8] B. S. Mao, G. Lu, K. Yu, Z. Bo, J. Chen, *Adv. Mater.* **2010**, 22, 3521.

[9] S. Myung, A. Solanki, C. Kim, J. Park, K. S. Kim, K. B. Lee, *Adv. Mater.* **2011**, 23, 2221.

[10] E. Eltzov, A. Cohen, R. S. Marks, *Anal. Chem.* **1994**, 9, 373.

[11] C. Dhand, M. Das, M. Datta, B. D. Malhotra, *Biosens. Bioelectron.* **2011**, 26, 2811.

[12] O. S. Kwon, S. J. Park. J. Jang, *Biomaterials* **2010**, 31, 4740.

[13] B. Xu, J. C. Pizarro, M. A. Holmes, C. McBeth, V. Groh, T. Spies, R. K. Strong, *Proc. Natl. Acad. Sci. U. S. A.* **2011**, 108, 2414.

[14] X. Duan, Y. Li, N. K. Rajan, D. A. Routenberg, Y. Modis, M. A. Reed, *Nat. Nanotechnol.* **2012**, 7, 401.

[15] X. Guo, C. S. Lin, S. H. Chen, R. Ye, V. C. H. Wu, *Biosens. Bioelectron.* **2012**, 38, 177.

[16] S. R. Ryoo, J. Lee, J. Yeo, H. K. Na, Y. K. Kim, H. Jang, J. H. Lee, S. W. Han, Y. Lee, V. N. Kim, D. H. Min, *ACS Nano* **2013**, 7, 5882.

[17] J. Sun, J. Ge, W. Liu, M. Lan, H. Zhang, P. Wang, Y. Wang, Z. Niu, *Nanoscale* **2014**, 6, 255.

[18] L. Gao, Q. Li, R. Li, L. Yan, Y. Zhou, K. Chen, H. Shi, *Nanoscale* **2015**, 7, 10835.

[19] A. Chen, S. Yang, *Biosens. Bioelectron.* **2015**, 71, 230.

[20] K. Nam, K. Eom, J. Yang, J. Park, G. Lee, K. Jang, H. Lee, S. W. Lee, D. S. Yoon, C. Y. Lee, T. Kwon, *J. Mater. Chem.* **2012**, 22, 23279.

[21] B. Yuna, Y. Zhou, Q. Guo, K. Wang, X. Yang, X. Meng, J. Wan, Y. Tan, Z. Huang, Q. Xie, X. Zhao, *Chem. Commun.* **2015**, 52, 1590.

[22] A. Li, L. Tang, D. Song, S. Song, W. Ma, L. Xu, H. Kuang, X. Wu, L. Liu, X. Chen, C. Xu, *Nanoscale* **2016**, 8, 1873.

[23] X. Li, Y. Peng, Y. Chai, R. Yuan, Y. Xiang, *Chem. Commun.* **2016**, 52, 3673.

[24] O. S. Kwon, S. R. Ahn, S. J. Park, H. S. Song, S. H. Lee, J. S. Lee, J. Hong, J. S. Lee, S. A. You, H. Yoon, T. H. Park, J. Jang, *ACS Nano* **2012**, 6, 5549.

[25] K. J. Kohlhoff, D. Shukla, M. Lawrenz, G. R. Bowman, D. E. Konerding, D. Belov, R. B. Altman, V. S. Pande, *Nat. Chem.* **2013**, 6, 15.

[26] H. S. Song, O. S. Kwon, S. H. Lee, S. J. Park, U. K. Kim, J. Jang, T. H. Park, *Nano Lett.* **2013**, 13, 172.

[27] S. H. Lee, O. S. Kwon, H. S. Song, S. J. Park, J. H. Sung, J. Jang, T. H. Park, *Biomaterials* **2012**, 33, 1722.

[28] H. S. Song, H. J. Jin, S. R. Ahn, D. Kim, S. H. Lee, U. K. Kim, C. T. Simons, S. Hong, T. H. Park, *ACS Nano* **2014**, 10, 9781.

[29] N. J. Ronkainen, H. B. Halsall, W. R. Heineman, *Chem. Soc. Rev.* **2010**, 39, 1747.

[30] L Lu, L. Zhang, F. Qu, H. Lu, X. Zhang, Z. Wu, S. Huan, Q. Wang, G. Shen, R. Yu, *Biosens. Bioelectron.* **2009**, 25, 218.

[31] F. Wang, J. Yang, K. Wu, *Analytica. Chimica. Acta.* **2009**, 638, 23.

[32] T. Shaymurat, Q. Tang, Y. Tong, L. Dong, Y. Liu, *Adv. Mater.* **2013**, 25, 2269.

[33] A. Gao, N. Lu, P. Dai, C. Fan, Y. Wang, T. Li, *Nanoscale* **2014**, 6, 13036.

[34] M. Larisika, C. Kotlowski, C. Steininger, R. Mastrogiacomo, P. Pelosi, S. Schutz, C. F. Peteu, C. Kleber, C. R. Rozman, C. Nowak, W. Knoll, *Angew. Chem. Int. Ed.* **2015**, 54, 13245.

[35] Z. Cheng, Q. Li, Z. Li, Q. Zhou, Y. Fang, *Nano Lett.* **2010**, 10, 1864.

[36] B. Zhan, C. Li, J. Yang, G. Jenkins, W. Huang, X. Dong, *Small* **2014**, 10, 4042.

[37] O. S. Kwon, S. J. Park, J. Hong, A. Han, J. S. Lee, J. S. Lee, J. H. Oh, J. Jang, *ACS Nano* **2012**, 6, 1486.

[38] J. Li, S. Pud, M. Petrychuk, A. Offenhausser, S. Vitusevich, *Nano Lett*, **2014**, 14, 3504.

[39] S. J. Park, H. S. Song, O. S. Kwon, J. H. Chung, S. H. Lee, J. H. An, S. R. Ahn, J. E. Lee, H. Yoon, T. H. Park, J. Jang, *Sci. Rep.* **2014**, 4, 4342.

[40] J. Lee, J. Jang, B. Choi, J. Yoon, J. Kim, Y. Choi, D. M. Kim, D. H. Kim, S. Choi, *Sci. Rep.* **2015**, 5, 12286.

[41] S. G. Kim, J. S. Lee, J. Jun, D. H. Shin, J. Jang, *ACS Appl. Mater. Interfaces* **2016**, 8, 6602.

[42] J. W. Park, S. J. Park, O. S. Kwon, C. Lee, J. Jang, *Anal. Chem.* **2014**, 86, 1822.

[43] J. W. Park, S. J. Park, O. S. Kwon, C. Lee, J. Jang, *Analyst* **2014**, 139, 3852.

[44] J. S. Lee, J. Oh, S. G. Kim, J. Jang, *Small* **2015**, 11, 2399

[45] W. Na, J. W. Park, J. H, An, J. Jang, *J. Mater. Chem. B* **2016**, 4, 5025

[46] H. Yoon, J. Jang, *Adv. Funct. Mater.* **2009**, 19, 1567.

[47] D. Chen, L. Tang, J. Li, *Chem. Soc. Rev*. **2010**, 39, 3157.

[48] A. K. Geim, K. S. Novoselov, *Nat. Mater*. **2007**, 6, 183.

[49] K. S. Kim, Y. Zhao, H. Jang, S. Y. Lee, J. M. Kim, K. S. Kim, J. Ahn, P.

Kim, J. Choi, B. H. Hong, *Nature* **2009**, 457, 706.

[50] Z. Wu, S. Pei, W. Ren, D. Tang, L. Gao, B. Liu, F. Li, C. Liu, H. Cheng, *Adv. Mater*. **2009**, 21, 1756.

[51] F. Bonaccorso, Z. Sun, T. Hasan, A. C. Ferrari, *Nat. Photonics* **2010**, 4, 611.

[52] Y. Lee, K. H. Tu, C. Yu, S. Li, J. Hwang, C. Lin, K. Chen, L. Chen, H. Chen, C. Chen, *ACS Nano* **2011**, 8, 6564.

[53] K. Shin, J. Hong, J. Jang, *Chem. Commun.* **2011**, 47, 8527.

[54] E. O. Polat, C. Kocabas, *Nano Lett*. **2013**, 13, 5851.

[55] W. Chen, C. Xia, H. N. Alshareef, *Nano Energy* **2015**, 15, 1

[56] P. You, Z. Liu, Q. Tai, S. Liu, F. Yan, *Adv. Mater*. **2015**, 27, 3632.

[57] K. S. Novoselov, V. I. Falko, L. Colombo, P. R. Gellert, M. G. Schwab, K. Kim, *Nature* **2012**, 490, 192.

[58] J. H. An, S. J. Park, O. S. Kwon, J. Bae, J. Jang, *ACS Nano* **2013**, 7, 10533

[59] O. S. Kwon, S. H. Lee, S. J. Park, J, H. An, H. S. Song, T. Kim, J. H. Oh, J. Bae, H. Yoon, T. H. Park, J. Jang, *Adv. Mater*. **2013**, 25, 4177.

[60] X. Li, J. Shan, W. Zhang, S. Su, L. Yuwen, L. Wang, *Small* **2017**, 13, 1602660.

[61] Q. H. Wang, K. Zadeh, A. Kis, J. N. Coleman, M. S. Strano, *Nat. Nanotechnol*. **2012**, 7, 699.

[62] H. Pan, Y. Zhang, *J. Mater. Chem*. **2012**, 22, 7280.

[63] M. Chhowalla, H. S. Shin, G. Eda, L. Li, K. P. Loh, H. Zhang, *Nat. Chem*. **2013**, 5, 263.

[64] X. Chia, A. Ambrosi, Z. Sofer, J. Luxa, M. Pumera, *ACS Nano* **2015**, 5, 5164.

[65]D. Sarkar, X. Xie, J. Kang, H. Zhang, W. Liu, J. Navarrete, M. Moskovits, K. Banerjee, *Nano Lett.* **2015**, 15, 2852

[66] M. Xu, T. Liang, M. Shi, H. Chen, *Chem. Rev*. **2013**, 113, 3766.

[67] H. Nam, S. Wi, H. Rokni, M. Chen, G. Priessnitz, W. Lu, X. Liang, *ACS Nano* **2013**, 7, 5870.

[68] Q. Qian, B. Li, M. Hua, Z. Zhang, F. Lan, Y. Xu, R. Yan, K. J. Chen, *Sci. Rep*. **2016**, 6, 27676.

[69] Y. Yao, Z. Lin, Z. Li, X. Song, K. Moon, C. Wong, *J. Mater. Chem*. **2012**, 22, 13494.

[70] K. Lee, R. Gatensby, N. McEvoy, T. Hallam, G. S. Duesberg, *Adv. Mater*. **2013**, 25, 6699.

[71] S. Cho, S. J. Kim, Y. Lee, J. Kim, W. Jung, H. Yoo, J. Kim, H. Jung, *ACS Nano* **2015**, 9, 9314.

[72] A. L. Friedman, F. K. Perkins, A. T. Hanbicki, J. C. Culbertson, P. M. Campbell, *Nanoscale* **2016**, 8, 11445.

[73] D. Sarkar, W. Liu, X. Xie, A. C. Anselmo, S. Mitragotri, K. Banerjee, *ACS Nano* **2014**, 4, 3992.

[74] D. Lee, J. Lee, I. Y. Sohn, B. Kim, Y. M. Son, H. Bark, J. Jung, M. Choi, T. H. Kim, C. Lee, N. Lee, *Nano Res*. **2015**, 8, 2340.

[75] G. A. Snook, P. Kao, A. S. Best, *J. Power Sources* **2011**, 196, 1.

[76] H. Shirakawa, *Angew. Chem. Int. Ed.* **2001**, 40, 2574.

[77] D. T. Mcquade, A. E. Pullen, T. M. Swager, *Chem. Rev*. **2000**, 100, 2537.

[78] J. Janata, M. Josowicz, *Nat. Mater*. **2003**, 2, 19.

[79] O. S. Kwon, S. J. Park, H. Park, T. Kim, M. Kang, J. Jang, H. Yoon, *Chem. Mater*. **2012**, 24, 4088.

[80] D. H. Shin, J. S. Lee, J. Jun, J. Jang, *J. Mater. Chem. A* **2014**, 2, 3364.

[81] A. Ramanavicius, A. Ramanaviciene, A. Malinauskas, *Electrochim. Acta* **2006**, 51, 6025.

[82] P. Camurlu, *RSC Adv*. **2014**, 4, 55832.

[83] O. S. Kwon, S. J. Park, H. Yoon, J. Jang, *Chem. Commun*. **2012**, 48, 10526.

[84] S. J. Park, O. S. Kwon, J. Jang, *Chem. Commun.* **2013**, 49, 4673.

[85] J. Jun, J. S. Lee, D. H. Shin, J. Jang, *ACS Appl. Mater. Interfaces* **2014**, 6, 13859.

[86] J. S. Lee, W. Kim, S. Cho, J. Jun, K. H. Cho, J. Jang, *J. Mater. Chem. B* **2016**, 4, 4447.

[87] F. Li, Y. Xu, X. Yu, Z. Yu, X. He, H. Ji, J. Dong, Y. Song, H. Yan, G. Zhang, *Biosens. Bioelectron.* **2016**, 82, 212.

[88] T. Riedel, F. Surman, S. Hageneder, O. P. Georgievski, C. Noehammer, M. Hofner, E. Brynda, C. R. Emmenegger, J. Dostalek, *Biosens. Bioelectron.* **2016**, 85, 272.

[89] R. Lozano, M. Naghavi, K. Foreman, S. Lim, K. Shibuya, V. Aboyans, J. Abraham, T. Adair, R. Aggarwal, S. Y. Ahn, M. A. Almazroa, M. Alvarado, and C. J. L. Murray, *Lancet* **2012**, 380, 2096.

[90] S. Lee, C. Lee, H. Mark, D. R. Meldrum, C. Lin, *Sens. Actuators, B* **2007**, 127, 598.

[91] J. Ren, J. Wang, J. Wang, N. W. Luedtke, E. Wang, *Biosens. Bioelectron.* **2012**, 31, 316.

[92]M. Li, S. K. Cushing, H. Liang, S. Suri, D. Ma, N. Wu, *Anal. Chem*. **2013**, 85, 2072.

[93] Q. Cao, Y. Teng, X. Yang, J. Wang, E. Wang, *Biosens. Bioelectron.* **2015**, 74, 318.

[94] J. Shen, Y. Zhou, F. Fu, H. Xu, J. Lv, Y. Xiong, A. Wang, *Talanta*, **2015**, 142, 145.

[95] Z. Ge, Y. Song, Z. Chen, W. Guo, H. Xie, L. Xie, *Anal, Chim. Acta* **2015**, 862, 24.

[96] T. Xu, J. Miao, Z. Wang, L. Yu, C. M. Li, *Sens. Actuators, B* **2011**, 151, 370.

[97] I. Lee, M. Jeun, H. Jang, W. Cho, K. H. Lee, *Nanoscale*, **2015**, 7, 16789.

[98] Z. Xi, R. Huang, Z. Li, N. He, T. Wang, E. Su, Y. Deng, *ACS Appl. Mater. Interfaces* **2015**, 21, 11215.

[99] M. Habara, H. Ikezaki, K. Toko, *Biosens. Bioelectron.* **2004**, 19, 1559.

[100] P. H. B. Aoki, P. Alessio, A. Riul, J. A. De. S. Saez, C. J. L. Constantino, *Anal. Chem*. **2010**, 82, 3537/

[101] J. Y. Heras, S. D. Rodriguez, R. M. Negri, F. Battaglini, *Sens. Actuators, B* **2010**, 145, 726.

[102] G.A. Evtugyna, S.V. Belyakovaa, R.V. Shamagsumovaa, A.A. Savelievb, A.N. Ivanova, E.E. Stoikovaa, N.N. Dolgovaa, I.I. Stoikova, I.S. Antipina, H.C. Budnikova, *Talanta* **2010**, 82, 613.

[103] D. Volpati, P. H. B. Aoki, C. A. R. Dantas, F. V. Paulovich, M. C. F. Oliveira, O. N. Pliveira, A. Riul, R. F. Aroca, C. J. L. Constantino, *Langmuir* **2011**, 28, 1029.

[104] K. Chang, R. L. C. Chen, B. Hsieh, P. Chen, H. Hsiao, C. Nieh, T. Cheng, *Biosens. Bioelectron.* **2010**, 26, 1507.

[105] C. Hui, P. Ji, S. Mi, S. Deng, *Biosens. Bioelectron.* **2013**, 47, 164.

[106] T. Leem H. L. Lee, M. H. Tsai, S. Cheng, S. Lee, J. Hu, L. Chen, *Biosens. Bioelectron.* **2013**, 43, 56.

[107] E. Voitechovic, D. Kirsanov, A. Legin, *Sens. Actuators, B* **2016**, 225, 209.

[108] X. Li, L. Staszewski, H. Xu, K. Durick, M. Zoller, E. Adler, *Proc. Natl. Acad. Sci. U. S. A.* **2002**, 99, 4692.

[109] F. Zhang, B. Klebansky, R. M. Fine, H. Xu, A. Pronin, H. Liu, C. Tachdjian, X. Li, *Proc. Natl. Acad. Sci. U. S. A.* **2008**, 105, 20930.

[110] S. Fendorf, H. A. Michael, A. V. Geen, *Science* **2010**, 328, 1123.

[111] M. F. Hughes, B. D. Beck, Y. Chen, A. S. Lewis, D. J. Thomas, *Toxicol. Sci.* **2011**, 123, 305.

[112] S. V. Flanagan, R. B. Johnston, Y. Zheng, *Bull. W. H. O.* **2012**, 90, 839.

[113] E. Doppa, L.M. Hartmannb, A. M. Floreaa, U. von Recklinghausenc, R. Pieperc, B. Shokouhia, A.W. Rettenmeiera, A.V. Hirnerb, G. Obec, *Toxicol. Appl. Pharmacol.* **2004**, 201, 156.

[114] V. C. Ezeh, T. C. Harrop, *Inorg. Chem.* **2012**, 51, 1213.

[115] B. K. Jena, C. R. Raj, *Anal. Chem.* **2008**, 80, 4836.

[116] J. R. Kalluri, T. Arbneshi, S. A. Khan, A. Neely, P. Candice, B. Varisli, M. Washington, S. McAfee, B. Robinson, S. Banerjee, A. K. Singh, D. Senapati, P. C. Ray, *Angew. Chem. Int. Ed.* **2009**, 48, 9668.

[117] K. de Mora, N. Joshi, B. L. Balint, F. B. Ward, A. Elfick, C. E. French, *Anal. Bioanal. Chem.* **2011**, 400, 1031.

[118] F. Salazar, S. Beggah, J. R. Meer, H. H.Girault, *Biosens. Bioelectron.* **2013**, 47, 237.

[119] T. Wang, R. D. Milton, S. Abdellaoui, D. P. Hickey, S. D. Minteer, *Anal. Chem*. **2016**, 88, 3243.

[120] M. Kim, H. Um, S. Bang, S. Lee, S. Oh, J. Han, K. Kim, J. Min, Y. Kim, *Environ. Sci. Technol.* **2009**, 43, 9335.

[121] Y. Wu, S. Zhan, F. Wang, L. He, W. Zhi, P. Zhou, *Chem. Commun*. **2012**, 48, 4459.

[122] Y. Wu, S. Zhan, H. Xing, L. He, L. Xu, P. Zhou, *Nanoscale* **2012**, 4, 6841.

[123] L. Cui, J. Wu, H. Ju, *Biosens. Bioelectron.* **2016**, 79, 861.

[124] A. A. Ensafi, N. Kazemifard, B. Rezaei, *Biosens. Bioelectron.* **2016**, 77, 499.

[125] H. Chang, X. Wang, K. Shiu, Y. Zhu, J. Wang, Q. Li, B. Chen, H. Jiang, *Biosens. Bioelectron.* **2013**, 41, 789.

[126] R. Zhang, W. Chen, *Biosens. Bioelectron.* **2017**, 89, 249.

[127] Y. Liu, X. Liu, Z. Guo, Z. Hu, Z. Xue, X. Lu, *Biosens. Bioelectron.* **2017**, 87, 101.

[128] X. Li, Z. Zhang, L. Tao, *Biosens. Bioelectron.* **2013**, 47, 356.

[129] E. Ortega, S. Marcos, J. Galban, *Biosens. Bioelectron.* **2013**, 41, 150.

[130] J. Liu, X. Wang, L. Jiao, M. Cui, L. Lin, L. Zhang, S. Jiang, *Talanta* **2013**, 116, 199.

[131] W. Wu, J. Li, L. Chen, Z. Ma, W. Zhang, Z. Liu, Y. Cheng, L. Du, M. Li, *Anal. Chem.* **2014**, 86, 9800.

[132] Y. Lin, M. Zhao, Y. Guo, X. Ma, F. Luo, L. Guo, B. Qiu, G. Chen, Z. Lin, *Sci. Rep.* **2016**, 6, 37879.

[133] C. Hou, Q. Xu, L. Yin, X. Hu, *Analyst* **2012**, 137, 5803.

[134] Y. Zhang, X. Bai, X. Wang, K. Shiu, Y. Zhu, H. Jiang, *Anal. Chem.* **2014**, 86, 9459.

[135] X. Zhang, Q. Liao, M. Chu, S. Liu, Y. Zhang, *Biosens. Bioelectron.* **2014**, 52, 281.

[136] X. Liu, Z. Han, F. Li, L. Gao, G. Liang, H. Cui, *ACS Appl. Mater. Interfaces* **2015**, 7, 18283.

[137] P. Pannopard, C. Boonyuen, C. Warakulwit, Y. Hoshikawa, T. Kyotanim, J. Limtrakul, *Carbon* **2015**, 94, 836.

[138] T. Wang, H. Zhu, J. Zhuo, Z. Zhu, P. Papakonstanitnou, G. Lubarsky, J. Lin, M. Li, *Anal. Chem.* **2013**, 85, 10289.

[139] Y. Lin, X. Chen, Y. Lin, Q. Zhou, D. Tang, *Microchim. Acta* **2015**, 182, 1803.

[140] X. Lin, Y. Ni, S. Kokot, *Biosens. Bioelectron.* **2016**, 79, 685.

[141] H. Shafiee, M. K. Kanakasabapathy, F. Juillard, M. Keser, M. Sadasivam, M. Yuksekkaya, E. Hanhauser, T. J. Henrich, D. R. Kuritzkes, K. M. Kaye, U. Demirci, *Sci. Rep.* **2014**, 4, 9919.

[142] S. R. Ahn, J. H. An, H. S. Song, J. W. Park, S. H. Lee, J. H. Kim, J. Jang, T. H. Park, *ACS Nano* **2016**, 10, 7287.

[143] W. Feng, L. Chen, M. Qin, X. Zhou, Q. Zhang, Y. Miao, K. Qiu, Y. Zhang, C. He, *Sci. Rep*. **2015**, 5, 17422.

[144] S. J. Park, O. S. Kwon, S. H. Lee, H. S. Song, T. H. Park, J. Jang, *Nano Lett.* **2012**, 12, 5082.

[145] J. Zhao, Y. Xie, D. Guan, H. Hua, R. Zhong, Y. Qin, J. Fang, H. Liu, J. Chen, *Sci. Rep.* **2015**, 5, 12544.

[146] S. Bae, H. Kim, Y. Lee, X. Xu, J. Park, Y. Zheng, J. Balakrishnan, T. Lei, H. R. Kim, Y. Song, Y. Kim, K. S. Kim, B. Ozyilmaz, J. Ahn, B. H. Hong, S. Iijima, *Nat. Nanotechnol*. **2010**, 5, 574.

[147] D. Graf, F. Molitor, K. Ensslin, C. Stampfer, A. Jungen, C. Hierold, L. Wirtz, *Nano Lett.* **2007**, 7, 238.

[148] A. Srivastava, C. Galande, L. Ci, L. Song, C. Rai, D. Jariwala, K. F. Kelly, P. M. Ajayan, *Chem. Mater.* **2010**, 22, 3457.

[149] R. R. Nair, P. Blake, A. N. Grigorenko, K. S. Novoselov, T. J. Booth, T. Stauber, N. M. R. Peres, A. K. Geim, *Science* **2008**, 320, 1308.

N. M. R. Peres,2 A. K. Geim

[150] T. Chen, P. T. K. Loan, C. Hsu, Y. Lee, J. T. Wang, K. Wei, C. Lin, L. Li, *Biosens. Bioelectron.* **2013**, 41, 103.

[151] X. Yang, G. Liu, A. A. Balandin, K. Mohanram, *ACS Nano* **2010**, 10, 5532.

[152] Y. Ohno, K. Maehashi, K. Matsumoto, *J. Am. Chem. Soc.* **2010**, 132, 18012.

[153] H. Li, L. Rothberg, *Proc. Natl. Acad. Sci. U. S. A.* **2004**, 101, 14036.

[154] D. Tang, R. Yuan, Y. Chai, L. Zhang, J. Dai, Y. Liu, X. Zhong, *Electroanalysis* **2005**, 17, 155.

[155] X. Wang, Y. Li, H. Wang, Q. Fu, J. Peng, Y. Wang, J. Du, Y. Zhou, L. Zhan, *Biosens. Bioelectron.* **2010**, 26, 404.

[156] Z. Zou, J. Wang, H. Wang, Y. Li, Y. Lin, *Talanta* **2012**, 94, 58.

[157] H. Cruz, E. da Silva, C. A. Villela-Nogueira, L. C. Nabuco, K. M. Rodrigues, L. L. Lewis-Ximenez, C. Yoshida, E. Lampe, L. M. Villar, *J. Clin. Lab. Anal.* **2011**, 25, 134.

[158] B. S. Ravi, G. S. Vidya, *IJSRP*. **2014**, 4, 1.

[159] F. Schedin, A. K. Geim, S. V. Morozov, E. W. Hill, P. Blake, M. I. Katsnelson, K. S. Novoselov, *Nat. Mater.* **2007**, 6, 652.

[160] X. Li, Y. Zhu, W. Cai, M. Borysiak, B. Han, D. Chen, R. D. Piner, L.

Colombo, R. S. Ruoff, *Nano Lett.* **2009**, 9, 4359.

[161] X. Dong, Y. Shi, W. Huang, P. Chen, L. Li, *Adv. Mater.* **2010**, 22, 1649.

[162] Y. Huang, X. Dong, Y. Shi, C. Li, L. Li, P. Chen, *Nanoscale* **2010**, 2, 1485.

[163] S. C. Feifel, K. R. Stieger, H. Lokstein, H. Luxc, F. Lisdata, *J. Mater. Chem. A* **2015**, 3, 12188.

[164] N. M. Grubor, R. Shinar, R. Jankowiak, M. D. Porter, G. J. Small, *Biosens. Bioelectron.* **2004**, 19, 547.

[165] K. Hayashi, M. Yamanaka, K. Toko, K. Yamafuji, *Sens. Actuators, B* **1990**, 2, 205.

[166] K. Toko, *Sens. Actuators, B* **2000**, 64, 205.

[167] J. Rhodes, A. Titherley, J. A. Norman, R. Wood, D. W. Load, *Food Addit. Contam.* **1991**, 8, 663.

[168] S. Yamaguchi, K. Ninomiya, *J. Nutr.* **2000**, 130, 921S.

[169] Y. Osawa, *Ecol. Food Nutr.* **2012**, 51, 329.

[170] J. Loliger, *J. Nutr.* **2000**, 130, 915S.

[171] S. Yamaguhi, *Food Rev. Int.* **1998**, 14, 139.

[172] K. Ninomiya, *Food Rev. Int.* **2002**, 18, 23.

[173] S. Kaneko, K. Kumazawa, H. Masuda, A. Henze, T. Hofmann, *J. Agric. Food Chem.* **2006**, 54, 2688.

[174] N. Hayashi, R. Chen, H. Ikezake, T. Ujihara, *J. Agric. Food Chem.* **2008**, 56, 7384.

[175] J. Wu, W. E. Chang, Y. T. Chang, C. Chang, *Adv. Mater*. **2016**, 28, 3718.

[176] L. Tan, K. Xu, T. Liu, P. Liang, M. Niu, H. Shao, J. Yu, T. Ma, H. Li, J. Dou, J. Ren, X. Meng, *Small* **2016**, 12, 2046.

[177] S. Hu, W. Chen, J. Zhou, F. Yin, E. Uchaker, Q. Zhang, G. Cao, *J. Mater. Chem. A* **2014**, 2, 7862.

[178] O. S. Kwon, J. Hong, S. J. Park, Y. Jang, J. Jang, *J. Phys. Chem. C*

2010, 114, 18874.

[179] J. S. Lee, S. G. Kim, J. Jun, D. H. Shin, J. Jang, *Adv. Funct. Mater.* **2014**, 24, 6145.

[180] J. Jun, J. Oh, D. H. Shin, S. G. Kim, J. S. Lee, W. Kim, J. Jang, *ACS Appl. Mater. Interfaces* **2016**, 8, 33139.

[181] J. S. Lee, J. Jun, D. H. Shin, J. Jang, *Nanoscale* **2014**, 6, 4188.

[182] H. Yoon, S. H. Lee, O. S. Kwon, H. S. Song, E. H. Oh, T. H. Park, J. Jang, *Angew. Chem. Int. Ed.* **2009**, 48, 2755.

[183] V. V. Singh, K. Kaufmann, E. Karshalev, J. Wang, *Adv. Funct. Mater.* **2016**, 26, 6270.

[184] Y. Wu, S. Zhan, H. Xing, L. Xu, P. Zhou, *Nanoscale* **2012**, 4, 6841.

[185] R. Liang, Z. Wang, L. Zhang, J. Qiu, *Chem. Eur. J.* **2013**, 19, 5029.

[186] R. A. Dar, N. G. Khare, D. P. Cole, S. P. Karna, A. K. Srivastava, *RSC Adv.* **2014**, 4, 14432.

[187] N. Moghimi, M. Mohapatra, K. T. Leung, *Anal. Chem.* **2015**, 87, 5546.

[188] T. Jiang, Z. Guo, J. Liu, X. Huang, *Electrochim. Acta* **2016**, 191, 142.

[189] W. Jung, J. Park, T. Yoon, T. Kim, S. Kim, C. Han, *Small* **2014**, 10, 1704.

[190] T. Yang, Y. Chen, B. Qu, L. Mei, D. Lei, Q. Li, T. Wang, *Electrochim. Acta* **2014**, 115, 165.

[191] Y. Lu, Q. Zhao, N. Zhang, K. Lei, F. Li, J. Chen, *Adv. Funct. Mater.* **2016**, 26, 911.

[192] P. Sun, W. Zhang, X. Hu, L. Yuan, Y. Huang, *J. Mater. Chem. A* **2014**, 2, 3498.

[193] S. K. Hong, S. M. Song, O. Sul, B. J. Cho, *J. Electrochem. Soc.* **2012**, 159, K107.

[194] D. H. Shin, J. S. Lee, J. Jun, J. H. An, S. G. Kim, K. H. Cho, J. Jang, *Sci. Rep.* **2015**, 5, 12294.

[195] Y. Lu, Q. Zhao, N. Zhang, K. Lei, F. Li, J. Chen, *Adv. Funct. Mater.*

2016, 26, 911.

[196] Y. Zhao, Y. Liu, H. Kang, K. Cao, C. Zhang, Y. Wang, H. Yuan, L. Jiao, *J. Power Sources* **2015**, 300, 358.

[197] X. Dong, D. Fu, W. Fang, Y. Shi, P. Chen, L. Li, *Small* **2009**, 12, 1422.

[198] J. Lee, K. S. Novoselov, H. S. Shin, *ACS Nano* **2010**, 5, 608.

[199] W. Yin, J. Yu, F. Lv, L. Yan, L. Zheng, Z. Gu, Y. Zhao, *ACS Nano* **2016**, 10, 11000.

[200] X. Wang, C. Chu, L. Shen, W. Deng, M. Yan, S. Ge, J. Yu, X. Song, *Sens. Actuators, B* **2015**, 206, 30.

[201] X. Lin, Y. Ni, S. Kokot, *Biosens. Bioelectron.* **2016**, 79, 685.

[202] T. Wang, H. Zhu, J. Zhuo, Z. Zhu, P. Papakonstantinou, G. Lubarsky, J. Lin, M. Li, *Anal. Chem.* **2013**, 85, 10289.

[203] L. Zhu, Y. Zhang, P. Xu, W. Wen, X. Li, J. Xu, *Biosens. Bioelectron.* **2016**, 80, 601.

[204] K. Zhao, W. Gu, S. Zheng, C. Zhang, Y. Xian, *Talanta* **2015**, 141, 47.

[205] J. Yu, X. Ma, W. Yin, Z. Gu, *RSC Adv.* **2016**, 6, 81174.

[206] K. Zhang, H. Sun, S. Hou, *Anal. Methods* **2016**, 8, 3780.

[207] X. Li, X. Du, *Sens. Actuators, B* **2017**, 239, 536.

[208] Y. Shu, J. Chen, Q. Xu, Z. Wei, F. Liu, R. Lu, S. Xu, X. Hu, *J. Mater. Chem. B* **2017**, 5, 1446.

국문초록

바이오센서는 의학진단, 약물전달, 음식의 품질관리, DNA 검출 및 독성 평가 등 다양한 분야에 활용 될 수 있기 때문에 고성능 센서에 대한 개발이 국제적으로 요구되고 있다. 특히 고신뢰성, 고감도, 고선택성을 특징으로 하는 바이오센서 개발에 대한 관심이 지속적으로 증가하고 있다. 색 및 형광 변화를 측정하여 타겟 물질을 검출하는 센서에 대한 개발이 활발히 진행되고 있으나 느린 반응시간, 낮은 민감도 및 검출 방법의 복잡성과 같은 한계를 가진다. 이에 반해 전기화학적 검출 방법에 기반하는 전계 효과 트랜지스터 방식의 센서는 고감도, 짧은 분석시간 및 낮은 구동전압과 같은 다양한 장점을 갖고 있다. 이는 타겟 물질과 센서 수용체의 반응 결과를 트랜스듀서를 통해 측정가능한 전기적 신호로 효과적으로 변환 할 수 있기 때문이다. 트랜스듀서는 전계 효과 트랜지스터 센서의 성능 향상에 많은 영향을 미치는 요소이다.

본 학위 논문에서는 그래핀(graphene)과 이황화 몰리브덴을 트랜스듀서로 이용하여 전계 효과 트랜지스터 센서를 제조하였으며, 이들의 물성을 체계적으로 고찰하였다. 그래핀은 육각형의 격자를 이루는 단일원자층 두께의 탄소 박막이며, 뛰어난 전기적/물리적 특성들을 보여준다. 이황화

몰리브덴은 그래핀과 유사한 육각형의 격자 구조를 지니는 전이 금속 이유화 물질이며, 높은 전하 이동도 및 낮은 노이즈 수준 등의 장점을 가진다. 훌륭한 물성을 지니는 그래핀과 이황화 몰리브덴을 사용하여 다양한 바이오센서에 응용하였다.

첫째로, 화학 기상 증착(chemical vapor deposition) 방법을 이용해 그래핀 박막을 제조하고 포토 공정과 열증착 과정을 거쳐 센서 제조를 완료하였으며, 간염 및 맛과 관련된 인자를 검출하는데 적용하였다. 둘째로, 수열 반응으로 꽃 모양의 이황화 몰리브덴 나노 구조체를 합성하고 비소 센서에 응용하였다. 마지막으로, 수열 반응을 통해 이황화 몰리브덴 나노 구조체를 그래핀 표면에 성장시키고 과산화수소 센서에 적용하였다. 본 연구에서 제조된 센서들은 높은 감도, 뛰어난 선택성, 빠른 응답속도 및 안정성을 제공하며 센서의 성능을 향상시킬 수 있었다.

주요어: 그래핀, 이황화 몰리브덴, 전계-효과 트랜지스터, 바이오센서

학번: 2014-31079